Master's thesis

NTNU
Norwegian University of Science and Technology
Faculty of Engineering
Department of Structural Engineering

Anders Hald

Dynamic Response of Steel Plates Subjected to Combined Impact and Blast Loading

An Experimental and Numerical Study

Master's thesis in Engineering and ICT
Supervisor: Vegard Aune
June 2019

NTNU
Kunnskap for en bedre verden

Anders Hald

Dynamic Response of Steel Plates Subjected to Combined Impact and Blast Loading

An Experimental and Numerical Study

Master's thesis in Engineering and ICT
Supervisor: Vegard Aune
June 2019

Norwegian University of Science and Technology
Faculty of Engineering
Department of Structural Engineering

NTNU
Norwegian University of
Science and Technology

Department of Structural Engineering
Faculty of Engineering
NTNU- Norwegian University of Science and Technology

ACCESSIBILITY
Open

MASTER THESIS 2019

SUBJECT AREA:	DATE:	NO. OF PAGES:
Computational Mechanics	June 11th 2019	152

TITLE:

Dynamic response of steel plates subjected to combined impact and blast loading

Dynamisk respons av stålplater utsatt for kombinert støt- og eksplosjonslast

BY:

Anders Hald

SUMMARY:

This thesis investigates the behavior of flexible steel plates exposed to the combination of impact- and blast loading, using experimental- and numerical studies. The numerical work consists of a preliminary study and a final numerical study with full load configurations. All experiments were conducted at the Norwegian University of Science and Technology (NTNU). The tested plates were made from 0.8 mm thick Docol 600DL and Docol 1400M steel. All conducted experiments were documented using high-speed cameras. The blast loading experiments were also documented using other methods.

All numerical models of this thesis used a pure Lagrangian approach, simplified boundaries, and were run using Abaqus Explicit. The applied loading was applied as idealized pressure-time curves.

14 plates were tested in the SIMLab shock tube facility (SSTF), with a total of 38 experiments being conducted in the ballistics rig. In the SSTF, the two materials were tested using equal firing pressures for the shared configurations in order to establish a basis for comparison. In addition, the plates experiencing oblique impact were tested at higher firing pressures to determine the capacity.

In the final numerical studies, simulations were conducted on pure ballistics. In addition, the combination of impact- and blast loading were modelled and compared to the experimental data for validation. A parametric study was conducted on the CL fracture parameter and the strain rate sensitivity parameter.

RESPONSIBLE TEACHER: Vegard Aune

SUPERVISOR(S): Vegard Aune, Tore Børvik and PhDc Benjamin Stavnar Elveli

CARRIED OUT AT: Department of Structural Engineering, NTNU

Institutt for konstruksjonsteknikk
Fakultet for ingeniørvitenskap
NTNU- Norges teknisk- naturvitenskapelige universitet

TILGJENGELIGHET
Åpen

MASTEROPPGAVE 2019

FAGOMRÅDE:	DATO:	ANTALL SIDER:
Beregningsmekanikk	11. juni 2019	152

TITTEL:

Dynamisk respons av stålplater utsatt for kombinert støt- og eksplosjonslast

Dynamic response of steel plates subjected to combined impact and blast loading

UTFØRT AV:

Anders Hald

SAMMENDRAG:

Hovedmålet med denne oppgaven er å studere oppførselen av fleksible stålplater utsatt for kombinert støt- og eksplosjonslast ved bruk av eksperimentelle- og numeriske studier. Det numeriske arbeidet består av et forstudie og et endelig numerisk studie med den fulle lastkonfigurasjonen. Alle eksperimentene ble utført ved Norges Teknisk- Naturvitenskapelig Universitet (NTNU) I Trondheim. Platene var laget av 0.8 mm tykke Docol 600DL og Docol 1400M stål. Alle utførte eksperimenter ble dokumentert med høy-hastighets kameraer. Eksplosjonslasteksperimentene ble også dokumentert med andre metoder.

Alle numeriske modeller I denne tesen bruker en Lagrangian beskrivelse, forkenklede opplagere og ble kjørt med Abaqus Explicit. Den påførte lasten ble tatt idealiserte trykk-tids kurver.

14 plater ble tested I SIMLab shock tube facility (SSTF), med totalt 38 eksperimenter utført I ballistikk riggen. De to materialene ble testet I SSTF med like avfyringstrykk for å etablere en sammenligningsbasis. I tillegg ble platene som opplevde skrå beskytning testet på høyere trykk for å bestemme kapasiteten.

Simuleringer ble utført på ballistikk i det endelige numeriske studiet. I tillegg ble det utført simuleringer på kombinert støt- og eksplosjonslast, som ble sammenlignet med de eksperimentelle resultatene for validering. Et parameterstudie ble utført for CL bruddparameteren og for tøyningsrate sensitivitetsparameteren.

FAGLÆRER: Vegard Aune

VEILEDER(E): Vegard Aune, Tore Børvik og PhDc Benjamin Stavnar Elveli

UTFØRT VED: Institutt for Konstruksjonstekikk, NTNU

Department of Structural Engineering
FACULTY OF ENGINEERING SCIENCE AND TECHNOLOGY
NTNU – Norwegian University of Science and Technology

MASTER'S THESIS 2019

for

Anders Hald

Dynamic response of steel plates subjected to combined blast and impact loading

1. INTRODUCTION

Protection of vital infrastructure against blast or impact loading has received a lot of attention in recent years. However, the literature is rather scarce when it comes to studies on the combined effect of blast and impact loading. This is often the case in real scenarios where hazardous fragments may be accelerated by the blast wave. It is known from experience that the combined effect of blast and fragment impact may be more severe than the effect of the blast or impact alone. Despite these observations, such loading scenarios are not covered by design codes and few studies are available in the open literature. Computational methods are now available to predict both the loading and structural response in these extreme loading situations, and experimental validation of such methods is necessary in the development of safe and cost-effective protective structures. In this study blast experiments will be performed on thin steel plates, and the data will be used for validation of some frequently used computational methods involving blast and impact loading.

2. OBJECTIVES

The main objective of the research project is to develop a better understanding of how thin steel plates behave under combined blast and impact loading, and to validate to which extent this can be predicted using computational tools. Special focus is placed on the influence of fragment penetration on the performance of blast-loaded plates.

3. A SHORT DESCRIPTION OF THE RESEARCH PROJECT

The main topics in the research project will be as follows;

1. A comprehensive literature review should be conducted to understand the blast load phenomenon, the combined effect of blast and impact loading, constitutive and failure modeling of steel plates exposed to extreme loadings, and explicit finite element methods.
2. The steel plates are manufactured from cold-rolled sheets of type Docol 600DL and Docol 1400M. Material data and input for the numerical simulations will be based on previous studies in the literature.
3. Both ballistic tests and shock tube tests will be used to obtain combined blast and impact loading. The ballistic tests will be used to impact the plates with small-arms projectiles, before the same plates are exposed to blast loading in the shock tube. The shock tube tests will be used to investigate typical dynamic responses and failure modes of plates exposed to blast and impact loading.
4. Digital Image Correlation (DIC) and laser scanning will be used to measure the 3D transverse displacement fields of the plates in the experiments.
5. Non-linear FE numerical simulations of the ballistic and shock tube experiments will be performed, and the numerical results shall be compared and discussed based on the experimental findings.

Supervisors: Vegard Aune (NTNU), Tore Børvik (NTNU), Benjamin Stavnar Elveli (NTNU)

The thesis must be written according to current requirements and submitted to the Department of Structural Engineering, NTNU, no later than June 11th, 2019.

NTNU, January 15th, 2019

Vegard Aune

Vegard Aune
Associate Professor

Preface

This thesis was written in the spring of 2019 and submitted in partial requirement for the degree of Master of Science in Engineering and ICT. The work has been funded by and carried out at, the Structural Impact Laboratory (SIMLab), housed at the Department of Structural Engineering at the Norwegian University of Science and Technology (NTNU).

Trondheim, June 11th, 2019

Anders Hald

Anders Hald

Abstract

This thesis investigated the behavior of flexible steel plates exposed to the combination of ballistic impact- and blast loading, using both experimental- and numerical studies. The numerical work consists of a preliminary study examining plates with simplified perforations exposed to blast loading, whereas the final numerical study examines the full loading configurations. All experiments were conducted at SIMLab facilities, housed at the Department of Structural Engineering, at the Norwegian University of Science and Technology (NTNU) in Trondheim. The ballistics experiments were conducted in a ballistics rig, and the blast loading experiments were conducted in the SIMLab Shock Tube Facility (SSTF). The tested plates were made from 0.8 mm thick Docol 600DL and Docol 1400M steel with a blast-exposed area of 300 mm x 300 mm. A total of three configurations were tested in the SSTF, with two of these configurations experiencing both normal- and oblique ballistic impact prior to blast loading. One configuration had a ballistic perforation through the center of the plate, and two configurations were impacted by four projectiles. All conducted experiments were documented using high-speed cameras. The blast loading experiments were also documented using three-dimensional digital image correlation, laser scanning of the deformed plates, and pressure sensors.

The preliminary study was executed using simplified perforations and aimed to establish a test matrix to execute experimentally in the SSTF. All numerical models of this thesis neglected the fluid-structure interaction effects, used simplified boundaries, and were run using an uncoupled Lagrangian approach in Abaqus Explicit. The applied loading was applied as idealized pressure-time curves. The effects of element size were explored in the preliminary study.

In total, 14 plates were tested in the SSTF, with a total of 38 experiments being conducted in the ballistics rig. In the SSTF, the two materials were tested using equal firing pressures for the shared configurations in order to establish a basis for comparison. In addition, the plates experiencing oblique impact were tested at higher firing pressures to determine the capacity.

In the final numerical studies, simulations were conducted on pure ballistics in order to determine a suitable number of elements over the thickness. The combination of impact- and blast loading were modelled and compared to the experimental data for validation. A parametric study was conducted on the fracture parameter and the strain rate sensitivity parameter.

Acknowledgements

This thesis is written for the Structural Impact Laboratory (SIMLab), at the Department of Structural Engineering, at the Norwegian University of Science and Technology (NTNU) in Trondheim. SIMLab is currently hosting the Centre for Advanced Structural Analysis (CASA). The research at SFI CASA is about understanding the structural- and material response when subjected to impact- and extreme loading. Their vision is to "establish a world-leading center for multi-scale testing, modelling, and simulation of materials and structures for industrial applications."

This research project is the first conducted at SIMLab for the combined effects of ballistic impact- and blast loading on steel plates, and I am thankful for the opportunity to work with this particular topic. It has been a demanding thesis yet fascinating and educational.

I want to thank my supervisors Associate Professor Vegard Aune, Professor Tore Børvik and Ph.D. candidate Benjamin Elveli, for the guidance they have provided during the spring, and also for the weekly meetings.

I would also like to thank Mr. Trond Auestad for the help during the ballistic impact- and shock tube experiments, and Professor Torodd Berstad for being helpful with the cluster "Snurre".

Lastly, I would like to thank Håvard Houmb Kristiansen and Gunnar Sigstad for providing me with some necessary data from their master thesis.

Contents

Chapter 1

Introduction

The following chapter presents the background and motivation for this thesis, a brief overview of relevant research that has been conducted in the fields of impact- and blast loading, as well as the objectives of this thesis.

1.1 Background and Motivation

An explosion is a rapid release of energy in an extreme manner [1], and may be caused either by accident or by intent, and may occur in a variety of circumstances. The gas-, oil- and other chemical industries are naturally more prone to accidental explosions, as they deal with pressurized equipment and highly flammable substances. An example of such an accident in recent time was the explosion of the Deepwater Horizon drilling rig in 2010, which cost 11 people their life [2].

Unfortunately, the world has seen a significant increase in terrorism [3], which in turn has the potential of harming or killing civilians and destroying infrastructure. With the steady increase of terrorism, there has also been an increase in the use of explosive devices, which, unfortunately, has become the weapon of choice for many terrorist attacks. The information on how to construct and manufacture an improvised explosive device (IED) is easily accessible to the public. This fact, as well as the mobility and portability of these IEDs, combined with the tremendous potential for damage, has led to a momentous increase in bomb attacks experienced all over the world.

In a realistic setting, the blast loading cannot only be considered - the consideration that structures could be struck, and potentially damaged, by objects has to be taken into account. These objects could be anything in the range from debris and fragments created by an explosion, to bullets and artillery shells. Fragments originating from a ruptured pressure vessel can weigh up to 6000 kg (dependent on type of vessel and the material within) [1], and the initial velocity of fragments caused by bursting of a cased TNT charge can have an initial velocity up to about 8000 ft/s ($\approx$ 2438 m/s), dependent on the charge- to casing weight ratio [1], [4]. This could, in turn, severely weaken the structure, resulting in a lower structural capacity compared to the effects of blast loading alone. By augmenting this, the problem at hand becomes more complex and troublesome.

To be able to protect the lives of civilians, as well as the infrastructure, the need for effective and reliable protective structures has seen a significant increase in attention in the last years [5]. These structures must be able to withstand the threat at hand and must be able to protect the civilians in the vicinity. A low-cost, high-strength and ductile material often used for this purpose is steel, which is often used in armored cars/trucks and vehicles transporting VIPs.

Due to the complexity of the two separate fields alone, it is evident that a combination of the two leads to a significant increase in complexity, both when it comes to loading as well as the structural response. As a consequence of this, numerical simulations could be utilized as a means to acquire more insight, since full-scale experiments can be very troublesome, or impossible, to conduct. It is worth noticing that experiments should be conducted and used as a tool of comparison and validation for the established numerical models.

1.2 Previous Work

The response of impact- and blast loaded structures are both active fields of research, and a considerable amount of work already exists in each respective field. Work conducted by combining these two fields are somewhat scarce, but there exist a few research papers on steel and aluminum plates with pre-formed holes and slits and other geometrical holes that have been subjected to blast loading. On the contrary, the published work on combined impact- and blast loading are somewhat more limited, with the majority being conducted on reinforced concrete slabs.

A brief overview of previous work somewhat related to this thesis is therefore presented. The review is limited to the combination of blast loading and either impact loading or pre-formed/drilled slits and holes.

Pre-Formed Holes or Slits

Pre-formed holes and slits are added to a plate before the plate is exposed to blast loading in order to simulate, e.g., fragment and projectile impact to the structure prior to blast loading. Rakvåg *et al.* [6] studied the effects of pre-formed holes and slits with respects to structural response for Docol 600DL plates with a thickness of 0.7 mm subjected to pulse loading. The primary trend observed was that the plates with circular holes experienced less localized plastic strains and no significant reduction in capacity. Neither of the configurations exhibited failure. Further, it was observed that an increase in the perforation area led to a decrease of the final deflection and that the shape of the perforation played a role as well.

Granum and Løken (2016) [7] examined the dynamic response of 0.8 mm thick Docol 600DL steel plates subjected to blast loading at the SIMLab shock tube facility (SSTF) at NTNU. They examined plates with, and without, square holes which reduced the blast-exposed area by 16%. The full flexible plates showed no sign of failure, whereas the perforated plates were observed to fail at the corners, where cracks propagated outwards from these points. The experiments were then simulated numerically using both a purely uncoupled Lagrangian description, and a coupled and uncoupled Eulerian-Lagrangian approach.

Aune *et al.* (2017) [8] studied the dynamic response of 0.8 mm thick Docol 600DL plates subjected to blast loading both with and without, square holes. The blast loading experiments were conducted at the SSTF. This work is a continuation of previously conducted work [7]. In addition, pressure-time curves were obtained for solid steel plates which could be utilized for numerical studies at later occasions, and the solid plates were used as a basis to investigate the effect of fluid-structure interaction (FSI) for the deformable Docol plates. The trend observed was a reduction of reflection pressure when introducing perforated plates, as well as an increase in deflection when compared to the full flexible steel plates.

Stensjøen and Thorgeirsson (2017) [9] examined the blast response of aluminum plates with a thickness of 1.5 mm, with cross-shaped slits when exposed to blast loading in the SSTF. Special attention was devoted to the crack propagation of the experiments, and how well this could be recreated numerically. The experiments were modelled numerically using a purely Lagrangian approach in Abaqus and concluded that the models created in the preliminary study proved to be satisfactory when compared to the experimental results. They further concluded that solid element models need several elements over the thickness to accurately depict the crack propagation and failure modes of the plates.

Li *et al.* (2017) [10] studied the effects of pre-formed holes with different geometry subjected to blast loading created by a charge of TNT situated at a fixed distance with a varying amount of explosives for each experiment. All perforations of the experiments had the same area. They observed that plates with square- and circular holes did not experience fracture, whereas diamond-shaped holes did. The displacements were observed to increase linearly as the blast loading increased, and the deviations in displacements for the circular- and the square holes were observed to increase with increasing pressure as well. The conclusion was that the structural response is dependent on the perforation shape, with circular holes giving the highest capacity.

Elveli and Iddberg (2018) [11] examined the response of 0.8 mm thick Docol 600DL plates with square holes and slits exposed to blast loading in the SSTF. This work is a continuation of previous work [7], [8]. The results were modelled numerically and compared to the previous work for validation of the models. The numerical simulations were conducted using a purely uncoupled Lagrangian approach in Abaqus, which was compared to both a coupled and uncoupled Lagrangian approach in EUROPLEXUS [12].

Granum *et al.* (2019) [13] investigated the effects of cross-shaped slits on aluminum plates subjected to blast loading in the SSTF. This work is a continuation of previous work [9]. The test program consisted of four different configurations with different heat tempers. It was observed that the number and the orientations of the slits gave a significant effect on the capacity and the observed failure modes. Further, it was observed that the failure modes did not get affected by heat tempering, but it influenced the blast resistance and the crack propagation, due to a change in work-hardening and ductility of the material.

Combined Impact- and Blast Loading

Del Linz *et al.* (2016) [14] studied the response of reinforced concrete with a varying thickness between 100-200 mm subjected to a total of 346 impacting ball bearings, originating from an explosive device of TNT placed at a stand-off distance of 2.1 m. They observed a maximum penetration depth of 25 mm as well as some connecting cracks between the different craters. From this, they concluded that the capacity of the slabs was sufficient and that the damage sustained was superficial, as no damage occurred at the back of the slabs, not jeopardizing the overall structural integrity.

Grisario *et al.* (2018) [15] studied the combined effects of fragments and blast loading on the overall impulse and pressure-time histories, which were validated numerically with good agreement. In the experiments, a steel-cased cylindrical charge of TNT where detonated. Two cases were examined, were different charge- and casing masses were used. The explosive charge was situated above and at ground level for both cases. It was observed that a low charge mass to casing mass ratio had a negligible fragment impulse. Whereas an increase in this ratio resulted in an impulse that could not be neglected. The damage exerted to structure could not be neglected, as it proved to be significant.

Osnes *et al.* (2019) [16] studied the combined effects of impact- and blast loading on laminated glass. The study considered laminated glass plates without any prior damage, with a pre-drilled hole at the center of the plate, and with projectile perforation using a 7.62 mm AMP2 bullet weighing approximately 10.5 g. The result of this study was that damage to the laminated glass plates prior to blast loading gave a lower blast resistance. This was because the interlayer of the glass was observed to rupture completely for some cases, thus causing the glass to fail as the blast wave hits. This subsequently lead to the detachment of shards of glass, which ultimately might have caused further damage to personnel. From the experiments, it was concluded that ballistic impact prior to blast loading was the most detrimental.

Ma *et al.* (2013) [17] studied the effects of combined ballistics and blast loading on 6 mm thick XAR-450 steel plates, which is a high-strength steel with an approximate yield stress of 1200 MPa and tensile strength of 1400 MPa [18]. The combined effects were studied both experimentally and numerically using Abaqus. The study was executed by firing projectiles with a maximum velocity of approximately 434 m/s at the steel target, then exposing the plates to the blast of 100 kg of TNT detonated at a stand-off distance of 15 m.

The results showed that no detrimental damage was inflicted on the steel plates, and the maximum deflection from blast loading was measured to 8 mm. The simulations yielded excellent results and showed that the results are dependent on the strain rate. From this, it was concluded that the plates had more than sufficient capacity.

Marchand *et al.* (1992) [19] studied the synergism between fragment- and blast loading for close-in bomb loading on reinforced concrete and reinforced slurry infiltrated fiber concrete (SIFCON). The explosive used was a bare charge of C4 and a steel-cased charge of C4, both with the same weight. From the experimental work, it was found that the internal stress of the plates was significantly increased when using steel-cased charges versus bare charges. It was further observed that the combination of blast and fragments were more severe than the bare charge alone, as it caused larger and more significant breaches of the concrete. In addition, it was observed that the use of cased charges resulted in higher velocities of the fragments, where the maximum velocity was measured to approximately 6900 feet/s (≈2100 m/s). The explosions caused a maximum debris velocity (debris from the concrete targets) of 336 feet/s (≈ 100 m/s). From this, it was concluded that the synergistic effects were significant, and thus that fragment loading should not be neglected.

Kong *et al.* (2013) [20] studied the synergistic effect of blast- and fragment loading on a multi-layer protective structure made from steel. This effect was investigated both experimentally and numerically in ANSYS Autodyn [21]. This type of structure has a *liquid cabin* where a liquid is stored in order to diminish the blast loading effects. This cabin was empty in the experiments. A steel-cased cylindrical charge of TNT was placed inside of the structure. A numerical study was conducted on the fragmentation of the explosive device, using a model that had been validated by the authors in a previous study. Here, fragments were formed with a maximum weight of 36.1 g, and with an average speed of 1389.1 m/s. The experimental velocities were observed to be slightly smaller than the numerical results. It was observed that the combination of fragment- and blast loading caused significant damage, which was amplified as the explosive charge was situated in a defined space. The fragments were observed to cause perforations, which coalesced as the blast wave hit the structure, causing it to ultimately fail. The numerical simulations yielded excellent results with good accuracy for the experiments.

Ebrahimi *et al.* (2016) [22] studied the numerical response of honeycomb sandwich panels subject to combined blast- and impact loading. The models had been previously validated and were simulated in Abaqus without considering FSI effects. The models were firstly subjected to pressure and then impacted by a projectile with fixed mass and different impact velocities. The study concluded that vertical impact was the most detrimental factor, although acute angles experienced a higher core crushing strain. For higher impacting velocities, the cores of the models were observed to fail near the boundaries.

1.3 Objectives

The increased demand for protective structures has led to a steady increase in the use of numerical- and computational methods. As a vast majority of blast load cases are impossible to conduct on a full-scale due to limitations, the role of the numerical methods has become ever more prominent, and the need to evaluate and assess the performance of such methods are deemed important. The overall objectives of this thesis are as follows:

- Obtain knowledge and understanding of how thin steel plates behave under combined impact- and blast loading.
- Setup and conduct experiments that are controlled and easily reproducible on each of the individual load cases.
- Use the test setup to obtain experimental data covering a wide range of dynamic responses of thin steel plates.
- Establish and assess the differences between the two steels with respect to the obtained experimental results.
- Validate to which extent the combination of these two load cases can be predicted by the use of non-linear Finite Element numerical simulations.
- Identify parameters influencing the dynamic response and capacity of thin steel plates in the experimental- and numerical studies.

This type of knowledge, comprehension, and considerations are deemed imperative to be able to meet the ever-increasing demand for innovative and optimized solutions in today's society. These solutions need to fulfill all aspects of safety, as well as architectural requirements when considering highly prominent threat of combined impact- and blast loading.

Chapter 2, Theory: Gives a brief introduction on impact and ballistics, where the emphasis is on basic notations and theory. Further gives an introduction to the blast phenomenon and shock tube theory. In addition, topics related to the numerical framework used for the models are presented as well. It should be noted that the presented theory is meant to be an introduction to some of the most essential aspects of this thesis, and not as a throughout and complete description.

Chapter 3, Material: Presents the two Docol steels used in this thesis with respect to material properties. Assumptions made to idealize the material model is presented. The modified Johnson-Cook constitutive relation and the Cockcroft-Latham fracture criterion are presented as well.

Chapter 4, Preliminary study: Aims to study the two materials with respect to structural response, as well as to establish a basis for the experimental section, in the form of a test matrix.

Chapter 5, Experimental work: Presents the experimental work. The impact experiments are presented in terms of calculated initial- and residual velocities, images of a selection of the resulting perforations and time-lapses of the penetration process. The test matrix serves as a basis when selecting firing pressures in the SIMLab shock tube facility (SSTF). All experiments are analyzed with the use of high-speed cameras. For the blast loading experiments, post-test images, pressure-time histories, midpoint displacements, and displacement profiles obtained with 3D-DIC, laser scanning of the deformed plates and cracking of the plates will be presented and discussed.

Chapter 6, Numerical study part I: Numerical study considering the ballistics aspect of the thesis. Mesh-sensitivity- and projectile studies are conducted to determine the most appropriate element size and numerical projectile for this thesis, which is used further in Chapter 7.

Chapter 7, Numerical study part II: Serves as a final numerical study, where the numerical- and experimental results from previous chapters are taken into account. Parametric studies are conducted on the fracture parameter and the strain-rate sensitivity parameter.

Chapter 2

Theory

2.1 Introduction

In this chapter, brief introductions to the fields of impact- and blast loading are given, as well as a basic presentation of explicit finite element methods (FEM) and the Lagrangian approach. This chapter aims to cover some of the most relevant terminology, definitions, and theory needed to describe the experiments and the main theory and considerations behind explicit FEM and numerical modelling.

2.2 Impact Loading

2.2.1 Basic Terminology

Impact and Ballistics

To better get an understatement of the field of ballistics, some fundamental terminology and definitions are presented in this section. Firstly, the definitions of impact and ballistics are taken from [23] and given as the following:

(a) *Impact* is defined as the collision between two or more objects, where the interaction between the colliding objects can be classified as either elastic, plastic or fluid, or any combination of these.

(b) *Ballistics* is defined as accelerating an object by the use of some kind of engine, with examples being either a compressed gas gun or a rifle. Ballistics deals with the forces, impact, and motion of free-flying objects, particularly those that have been discharged from firearms or guns. This field of research is usually divided into three main areas:

   (i) *Interior ballistics*, the study of motion and forces acting on an object when it is still within the launcher.

   (ii) *Exterior ballistics*, the study of the motion and forces acting on an object during free flight, and is in general covered by the theory of aerodynamics.

   (iii) *Terminal ballistics*, describes the interaction between the object and the target during impact.

As aforementioned in Chapter 1, a target structure may be impacted by a variety of objects. According to Zukas (1982) [24], a projectile can be defined as any item that can be launched. To be more refined, one can, in general, describe the impacting object using some generic terms. As this thesis only covers projectiles and fragments, the other terms will not be further presented. The following definitions have further been adapted throughout the thesis:

(a) *Projectile* refers to a device for general ballistic performance that serves specific ballistic functions. Examples of this are bullets, bombs and artillery shells.

(b) *Fragments* are pieces separated from a body by breaking, often generated by the failure of pressurized equipment, mines, etc. Such fragments are termed primary, while secondary fragments may be those generated by, e.g., a blast wave picking up loose objects and launching them towards the target.

Penetration and Perforation

As this thesis mainly focuses on the field of terminal ballistics, penetration is imperative, and it can thus be defined as the entry of a projectile into any region of a target [24]. Backman and Goldsmith (1978) [25] suggested the following definitions:

(a) *Perforation*, if the projectile passes through the target with a residual velocity.

(b) *Embedment*, if the projectile stops within the target.

(c) *Ricochet*, if the projectile is deflected off the target without being stopped.

Ballistic Limit Velocity

The ballistic limit velocity denoted v_{bl}, is defined as the lowest velocity a given projectile can have, for a given target, where the projectile perforates the target [26]. The ballistic limit velocity is considered a measurement of capacity when it comes to ballistics. This limit is dependant on numerous factors, and only a few are presented here for completeness. Some of these are the effect of the *projectile nose-shape*, *target strength* and *target thickness.* Børvik *et. al* (2002) [27] observed that the ballistic limit velocity and failure mode are severely affected by the nose-shape of the projectile, with pointed-nose projectiles giving a higher ballistic velocity. They further observed that the ballistic limit velocity increases monotonically with increasing target thickness. Børvik *et al.* (2009) [28] observed that the ballistic limit velocity increases linearly as the yield strength of the target increases for pointed-nose projectiles.

2.2.2 Energy Balance

To determine the ballistic limit velocity as well as validate the numerical models, energy balance in ballistics is an important measure. The energy balance is given as conservation of energy. Further, the change in kinetic energy is equal to the total work carried out, where the total work can be divided into contributing mechanisms. The energy balance can be expressed as the following [23]

$$\Delta K = K_f - K_i = W_l + W_g + W_{pr} + W_{el} + W_{fr} = W_{total} \tag{2.1}$$

where $\Delta K = K_f - K_i$ is the change in kinetic energy, W_l is the local target work, W_g is the global target work, W_{pr} is the projectile work, W_{el} is the elastic work and W_{fr} is the frictional work. In most models, only a few of these factors are typically considered, and frictional effects are generally of minor importance [23].

2.2.3 Failure Modes

During impact, the target may fail in a number of ways. The cause of failure is dependant on a variety of factors, such as impact velocity, projectile geometry, target support and thickness, and material properties. The most common failure modes are depicted in Figure 2.1. It usually is one of these failure modes that dominate the failure process, but other modes will usually accompany them. The most common failure modes in the velocity regime of this thesis, and for thin steel plates, are shortly presented. The definitions are taken from [23].

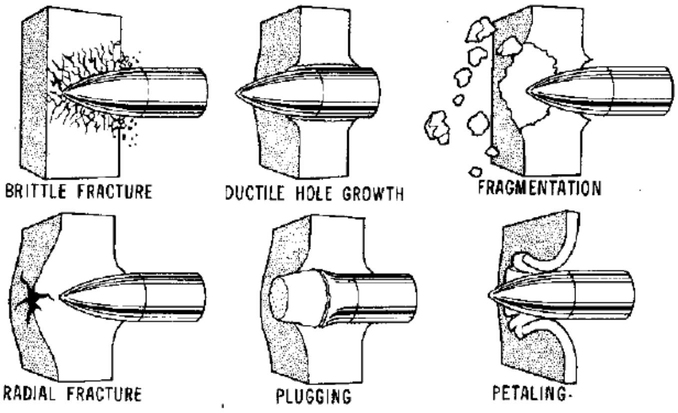

Figure 2.1: Common failure modes in target plates. Image is taken from [23].

Petaling is mostly observed in thin metal plates struck by pointed-nose projectiles. The petals are produced by high radial and circumferential tensile stresses after the passage of the initial stress wave occurring near the tip of the projectile.

Ductile hole growth is likely to occur in ductile materials struck by conical- or ogival projectiles. The projectile opens a microscopic hole, and the hole expands in the circumferential direction as the projectile passes through the target.

Fragmentation occurs at high impact velocities, where large amounts of energy are deposited in a short time resulting in very high local stresses. Fragmentation is mainly observed in brittle material such as concrete, but may also occur in high-strength steel if the impact velocity is sufficiently high.

2.3 Blast Theory

2.3.1 Blast Phenomena

Explosions

Explosions can be categorized as either mechanical, chemical, or nuclear [1], [29]. The latter will not be presented, as a nuclear explosion is a highly unlikely scenario in most cases.

- **Mechanical explosions** are caused by a gradual buildup of pressure. When the pressure reaches a critical point, the solid containing the expanding gas will rupture, and an explosion occurs. This type of explosion is mainly accidental and can occur as an industrial accident.
- **Chemical explosions** are caused by the rapid conversion from an explosive compound, either in solid- or liquid form, into gases of a much higher volume, compared to that of the substance from which it originated. Examples of this are the detonation of "traditional" explosives, such as TNT, C4, and gunpowder. All manufactured explosives, except for nuclear explosives, are chemical.

Explosive devices can be classified as either primary- or secondary explosives, which is based on their sensitivity to ignition [29]:

- **Primary explosives** are easily detonated by impact, a spark or a flame. An example of this are materials typically found in ammunition. When the trigger of a firearm is pulled, the firing pin will impact the percussion cap of the ammunition, and the primary explosive is detonated.
- **Secondary explosives** are not detonated as easily as primary explosives. To be able to detonate a secondary explosive, it is necessary to use a detonator (primary explosive). The high-velocity shock wave produced by the primary explosive will propagate through the secondary explosive at a detonation velocity which causes compression of the material and causes it to undergo adiabatic heating. Examples of such explosives include TNT and C4.

Shock Wave

Shock waves originate from an explosive detonation and can be seen as a discontinuity which causes abrupt changes in pressure, temperature, and density, propagating outwards from the origin. A shock wave occurs when the velocity of the wave itself is higher than the speed of sound in the surrounding medium [30]. For detonation in free air, the shock wave can be seen to propagate spherically, and consequently, the pressure of the wave will decrease in a cubic manner with the distance from the origin. The shock wave is able to propagate due to the disequilibrium present between the undisturbed medium in front of the shock wave and the highly-pressurized air in the shock front itself [31].

Rankine-Hugoniot Relations

As previously mentioned, as the shock wave propagates through an undisturbed medium, the physical properties of that medium will change. It is therefore beneficial to establish a relationship between the physical properties in the two possible states on each side of the shock wave. By utilizing the ideal gas law [32], the speed of sound in the non-shocked material can be expressed as

$$c = \sqrt{\gamma R T} \tag{2.2}$$

where γ is the heat capacity ratio, R is the universal gas constant, and T is the temperature of the gas. For air, it can be shown that γ=1.4. The relations mentioned above are given by the Rankine-Hugoniot relations which describe the conservation of mass, momentum, and energy across the discontinuity of the shock front. These equations were established by Rankine [33], [34] and Hugoniot [35], [36], and are given as

$$\rho_2 u_2 = \rho_1 u_1, \tag{2.3}$$

$$p_2 + \rho_2 u_2 = p_1 + \rho_1 u_1, and \tag{2.4}$$

$$\frac{p_2}{\rho_2} + e_2 + \frac{1}{2}u_2^2 = \frac{p_1}{\rho_1} + e_1 + \frac{1}{2}u_1^2 \tag{2.5}$$

where ρ_1, u_1 and p_1 denotes the density, particle velocity and hydrostatic pressure, respectively, for the shocked material, and ρ_2, u_2 and p_2 denotes the same quantities in the non-shocked material. In addition, e is the internal energy per unit volume.

The depiction of a generalized shock wave is depicted in 2.2. Here, the shock wave moves with a velocity u_s into the non-shocked fluid at rest, thus altering its properties. The shock Mach number M_s, which is given the ratio of the speed of an object moving through a fluid, can be expressed as

$$M_s^2 = \frac{6}{7}\frac{OP_{SO}}{P_a} + 1, \; where \; M_s = \frac{u_s}{c_a} \tag{2.6}$$

where OP_{SO} is the peak reflected overpressure and P_a is the ambient pressure.

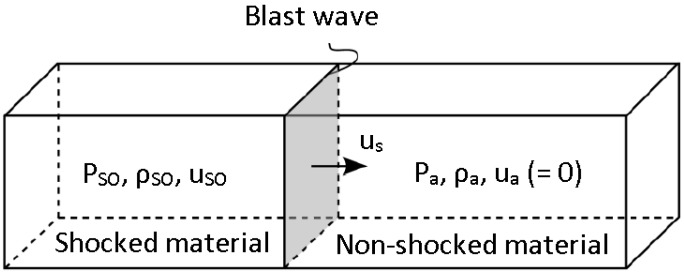

Figure 2.2: State variables defining the conditions ahead and behind a shock wave. Figure is taken from [29].

For further reading on the Rankine-Hugoniot relations as well as the derivation of Equation 2.6, the reader are referred to the journals of Rankine [33], [34], and Hugoniot [35], [36].

2.3.2 Shock Tube

Blast loading is a complex problem, usually with unknown loading and large deformations, and propagation of 3D blast waves which adds to its complexity. It is thus desirable with a controlled environment. With the use of a shock tube, it is possible to simulate blast loading using known boundary conditions and a well-defined shock wave. This section aims to present the basic shock tube theory and give the reader a better understanding of how a shock tube can be utilized in blast loading experiments.

Basic Design

The basic design of a shock tube is depicted in Figure 2.3. The tube can be divided into two parts, the *driver* and the *driven*. The driver is defined as the high-pressure chamber where the pressure is built-up using a compressor. The driven is defined as the section where a shock wave can propagate, and is separated from the driver by a set of membranes. The blast-exposed plate is mounted inside a tank at the end of the tube.

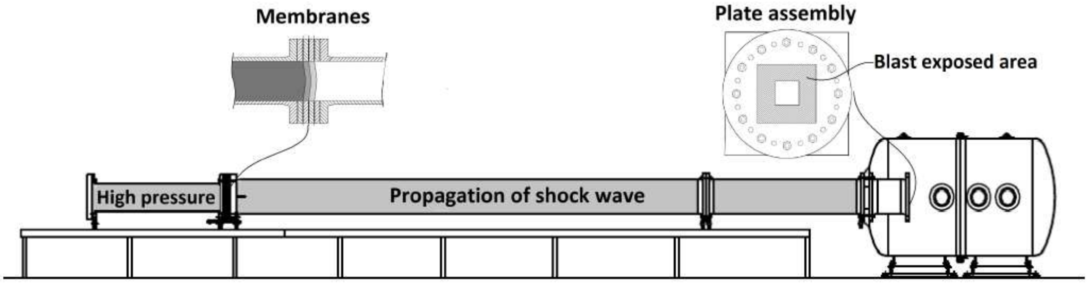

Figure 2.3: Illustration of basic shock tube design. Figure is taken from [11].

Basic Operation

The basic operation process is depicted in Figure 2.4. The pressure is built up in the high-pressure chamber (4) to the desired pressure level p_4. The driven-section (1) holds ambient pressure p_1. This is depicted in (a).

As the membranes rupture, the shock wave will propagate through the undisturbed air in (1) with a velocity of u_s. The previously undisturbed air now moves with a velocity u_2 and with a pressure of p_2 immediately behind the shock wave. Rarefaction waves (E) propagate in the opposite direction through the highly compressed air (3). This situation is depicted in (b).

When the rarefaction waves reach the end of the chamber, they are reflected, and now propagate in the same direction as the shock wave. The velocity of the rarefaction waves is higher than the velocity of the shock front because they propagate through air with a higher density. This can be seen in (c).

As the rarefaction waves catch up with the shock wave; the shock decays in strength, increases in duration, decreases in velocity, which results in a pressure profile that is similar to that of a far-field detonation, which can be seen in (d).

If the rarefaction waves catch up with the shock front wave is dependent on the design of the shock tube. As the shock front hits the boundary at the end of the tube, the wave is reflected, and the pressure is reinforced (5). This is depicted in (e). The rigid walls of the tank will further on reflect the shock wave.

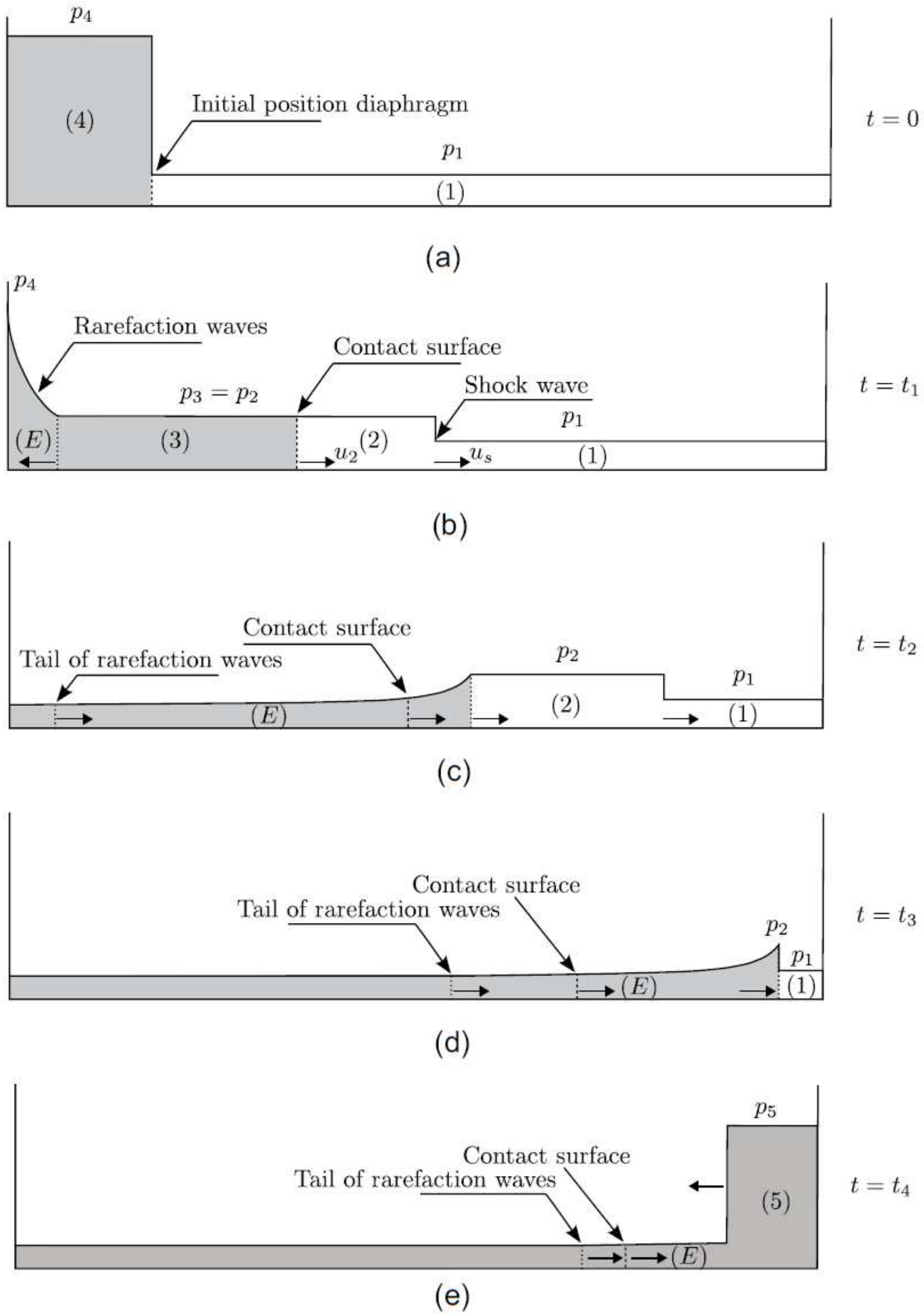

Figure 2.4: Schematic representation of the events occurring in a shock tube. Figure is taken from [37].

2.4 Important Differences Between Impact and Blast Loading

As impact- and blast loading are two widely different research fields, it consequently follows that there exist some significant differences between the two. These differences could, in turn, cause some problems when considering numerical analyses and may need to be considered thoroughly. The most important differences are presented in Table 2.1.

Table 2.1: Important differences between blast- and impact loading [23], [29].

Blast Loading	**Impact Loading**
Global problem	Local problem
Structural problem	Material problem
Large deformation/stability	Local failure
Moderate strains and strain rates	Large strains and strain rates
Isothermal conditions	Adiabatic conditions
Complex, unknown loading	Simple, well-defined loading
Shell element formulation	2D-axisymmetric or 3D element formulation
Fluid-structure interaction (FSI)	No fluid-structure interaction
Coupled Eulerian-Lagrangian FEA	Lagrangian FEA
Complex tests	Simple tests
Fluid mechanics	Solid mechanics

2.5 Explicit Finite Element Methods

When considering transient dynamics problems such as impact- and blast loading, where very small time increments are required, Explicit Finite Element Methods (FEM) are particularly suited. As iterations are done explicitly in time, there is no need for equation solving or equilibrium iterations, which makes each time step computationally inexpensive and ensures convergence [38]. Explicit FEM is usually reliable for problems with discontinuous nonlinearities such as contact problems, which makes it ideal for solving impact problems [39], [40]. It is worth noticing that even though the result converges, the method is conditionally stable [38], and small time increments are needed such that results do not blow out of proportion, as these results are prone to energy imbalance [41].

The following derivation is based on the work presented in [42], [43] and [38]. Explicit FEM is based on the principle of virtual power (PVP), using a Lagrangian description [44]. The PVP states that the sum of the virtual power of the internal forces and the inertia forces equals the virtual power of the external forces. The PVP can be formulated as the following on component form:

$$\int_V \delta \dot{\epsilon_{ij}} \sigma_{ij} dV + \int_V \delta v_i \rho a_i dV = \int_V \delta v_i b_i dV + \int_S \delta v_i \bar{t}_i dS \tag{2.7}$$

where *ij* denotes matrix element number ij, and *i* denotes vector element number i. Here, ϵ_{ij} is the strain rate and σ_{ij} is the stress. Further, ρ denotes the density of the material, and u_i, v_i and a_i denotes the displacement, velocity, and acceleration, respectively. V is the volume of the body, S is the surface of the body, and $\bar{t_i}$ is the traction force prescribed on the surface. In addition, the δ symbol denotes a quantity which is virtual, meaning that it is considered infinitesimal and arbitrary. These quantities still satisfy the compatibility conditions. By now interpolating the kinetic fields over the entire body, the following is obtained on matrix form:

$$\begin{gathered} \boldsymbol{u} = \boldsymbol{N}\boldsymbol{r},\ \boldsymbol{v} = \boldsymbol{N}\dot{\boldsymbol{r}},\ \boldsymbol{a} = \boldsymbol{N}\ddot{\boldsymbol{r}}, \\ \dot{\boldsymbol{\epsilon}} = \boldsymbol{\Delta}\boldsymbol{v} = \boldsymbol{\Delta}\boldsymbol{N}\dot{\boldsymbol{r}} = \boldsymbol{B}\dot{\boldsymbol{r}} \end{gathered} \tag{2.8}$$

where $\mathbf{N}$ is the global shape function matrix, $\mathbf{B}$ is the strain-displacement matrix, $\boldsymbol{\Delta}$ is a differential operator, and $\mathbf{r}$, $\dot{\boldsymbol{r}}$ and $\ddot{\boldsymbol{r}}$ are the global nodal displacement, velocity and acceleration, respectively. Inserting this it into the PVP, cancelling out the virtual quantities, and writing the result on matrix form, the semi-discrete equations of motions are obtained as the following

$$\boldsymbol{M}\ddot{\boldsymbol{r}} = \boldsymbol{R}^{ext} - \boldsymbol{R}^{int} \tag{2.9}$$

where $\boldsymbol{R^{int}}$ are the internal forces, $\boldsymbol{R^{ext}}$ are the external forces and $\mathbf{M}$ is the consistent mass matrix, which can be written as

$$\begin{aligned} \boldsymbol{R}^{int} &= \int_V \boldsymbol{B}^T \boldsymbol{\sigma} dV \\ \boldsymbol{R}^{ext} &= \int_V \boldsymbol{N}^T \boldsymbol{b} dV + \int_S \boldsymbol{N}^T \bar{\boldsymbol{t}} dS \\ \boldsymbol{M} &= \int_V \rho \boldsymbol{N^T} \boldsymbol{N} dV \end{aligned} \tag{2.10}$$

It is worth noticing that a lumped mass matrix is preferable in explicit FEM as it is trivial to find its inverse, and thus to compute the next step in Equation 2.9.

Time Increment

As previously stated, explicit FEM is conditionally stable, and there exists a critical time step Δt (also known as the Courant time step) which must not be exceeded as this could result in an unstable solution. If the solution becomes unstable, this could result in extreme exaggerations and oscillations of the results, as well as a significant change in the total energy balance [41]. The physical explanation for this is that the critical time step must be sufficiently small such that no information propagates further than the distance between two nodes for each time step. Thus, Δt can be defined as the minimum time it takes for a dilatational wave to move across an element in the numerical model. The critical time step can be expressed as

$$\Delta t = \frac{h_e}{c},\ where\ c = \sqrt{\frac{E}{\rho}} \tag{2.11}$$

where h_e is the characteristic length of the smallest element in the model, c is the speed of sound in the medium, E is Young's modulus, and ρ is the density. Here, the one-dimensional stress-wave theory has been assumed as well as an undamped system.

Contact

For contact problems in numerical simulations, it is necessary to prescribe both a contact approach algorithm, which handles the interacting geometries and constraint equations, which ensures non-physical penetrations. In an explicit analysis, the two most common approaches for contact problems are the Lagrangian multiplier method (LMM) and the penalty method (PM). The main differences between the two are that LMM increases the total number of unknowns and imposes the contact constraints in an exact manner, whereas for PM the number of unknowns is unchanged (which may cause ill-conditioning), and the constraints are only satisfied approximately [45]. In this thesis, only the penalty method is considered, as this is the applied method in Abaqus Explicit.

In contact problems, a master- and slave surface are prescribed to the model. The definitions of master- and slave surfaces according to [46] are that a slave node cannot penetrate a master surface, master nodes can penetrate a slave surface, and the slave surface is selected as the most finely meshed instance. This is illustrated in Figure 2.5.

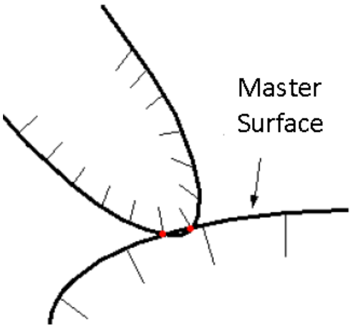

Figure 2.5: Definition of contact surfaces in Abaqus. The master surface is selected as the instant with the coarsest mesh, and no penetration of the slave surface is allowed. Figure is taken from [46].

In contact problems friction needs to be prescribed. In this thesis, the penalty friction formulation was prescribed, and a friction coefficient of zero was selected. As stated in Section 2.2.2, the frictional work is often omitted in numerical modelling and analytical models, consequently yielding a more conservative answer [23].

Energy

The critical time step presented in Equation 2.11 only ensures stability for a linear problem. For nonlinearity, the criterion is not sufficient, but it is necessary. For a highly non-linear analysis, the results may seem reasonable but may be blown out of proportion due to energy-dissipation. This occurs when using reduced integration and zero energy modes, such as hourglass modes are introduced. These modes are caused by spurious deformations or oscillations that do not induce any strain at the integration points [47], which causes the need for artificial stiffness in the elements. This subsequently leads to artificial strain energy being introduced. The artificial strain energy should, therefore, be checked, and the recommendation is that the ratio of the artificial strain energy divided by the internal energy does not exceed 2% [40], or be negligible compared to energies such as the kinetic- and internal energy [41].

Consequently, the total energy balance should differ negligibly from constant [41] such that no energy is added to the system, which is stated by the first law of thermodynamics [48].

Element Erosion

When considering the numerical modelling of experiments exhibiting material fracture, it is necessary to prescribe a fracture criterion for the model. In this thesis, the Cockcroft-Latham criterion was prescribed, which is described in Section 3.3.7.

Numerically, when the damage accumulated in an integration point is equal to a previously defined critical value, the stress in that particular point is set equal to zero, and the element is removed from the model when a user-specified number of the points fail. Element erosion can be viewed as an extremely rapid softening process, and crack propagation is observed to be highly mesh sensitive [42]. For quadratic elements using reduced integration, there exists only one integration point.

2.6 Uncoupled Eulerian and Lagrangian Approach

In the field of continuum mechanics, there exist two common approaches to describe a deforming body, namely the Lagrangian- and Eulerian approach. As these approaches, in this case, are linked to numerical methods such as FEM and computational fluid dynamics (CFD), the bodies are meshed and thus discretized by elements or computational cells. As this thesis only utilizes the Lagrangian approach, the Eulerian approach will only be presented briefly. It is also worth noticing that these two descriptions can be combined into a description known as arbitrary Lagrangian-Euler (ALE), but this is outside of the scope of this thesis. The description of the two approaches is based on [44], [49], and the reader is referred to these sources for a more comprehensive and complete presentation.

Eulerian approach: Also known as a *spatial description.* The properties of the continuum are evaluated with respects to time and spatial coordinates of a fixed reference frame. The mesh is stationary, and the continuum moves through the mesh as it deforms. This description is depicted in the lower part of Figure 2.6.

Lagrangian approach: Also known as a *material description*. The properties of the continuum are evaluated with respects to time and material coordinates. The mesh moves and deforms with the continuum. This approach is depicted in the upper part of Figure 2.6.

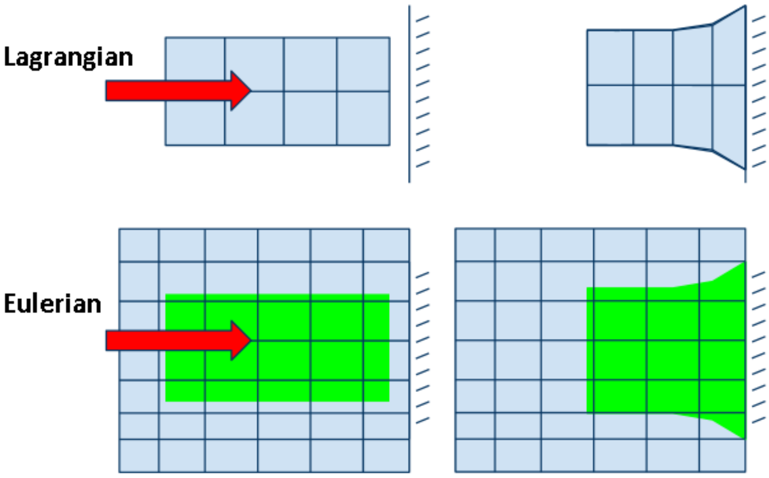

Figure 2.6: Image depicts the difference between the Eulerian- (lower) and Lagrangian description (upper). Figure is taken from [50].

In this thesis, the focus is on an *uncoupled* Lagrangian approach, i.e., a Lagrangian approach where the effects of fluid-structure interaction (FSI) are neglected. FSI has been neglected as it is not available in Abaqus, only through co-simulations through third-party programs [51]. To get a basic understatement of the theory behind FSI, CFD is briefly presented in the following.

For numerical simulations of blast loading, it may be very beneficial to consider **CFD** as this yields a proper modelling of the problem at hand. CFD is a method to numerically model problems related to fluid flows, which are present in such an analysis. The foundations of CFD are the conservation laws of fluid dynamics: conservation of mass, momentum, and energy. As these conservation laws contain a large number of unknowns, an equation of state (EOS) serves as a constitutive relation between a set of given physical quantities.

For a **uncoupled Lagrangian approach** there is no consideration of FSI, and consequently, simulations can be run as a purely structural analysis using FEM. In such analyses, the structural loading history has been predefined before the initiation of the analysis. The most common method to approximate the loading is to do a curve fit of the experimentally obtained pressure histories taken from pressure sensors. This can be done by the use of the Friedlander equation [52] which is given as

$$P(t) = P_a + P_r \left(1 - \frac{t}{t_+} \right) exp \left(\frac{-bt}{t_+} \right) \tag{2.12}$$

where P_a denotes the ambient pressure, P_r is the reflected pressure, t is the time, t_+ is positive time duration and b is the exponential decay coefficient. Such an approach assumes that the blast properties are unaltered by the structural motions and vice versa. Due to the highly non-linear response of the blast-exposed plates, such assumptions could lead to conservative results as well as a non-physical response [31].

Chapter 3

Material Model

3.1 Introduction

In the following chapter, the two materials used for the experiments will be presented. Firstly, a brief introduction of the microstructure of steel will be made, as well as a presentation of different alloying elements. The materials will then be presented and compared based on this preliminary introduction. This chapter aims to establish a constitutive model with a failure criterion, which in turn will be used for the numerical analyses.

3.2 Materials

Both of the Docol steels were produced by the same manufacturer, namely Swedish Steel AB (SSAB), and are both widely used in the automotive industry. The material constants of the two materials are given in Table 3.1.

Table 3.1: Material constants taken from the litterature [53], [31].

E [MPa]	ν [-]	ρ [kg/m^3]	c$_p$ [J/kgK]	χ [-]	T$_r$ [K]	T$_m$ [K]
210*10^3	0.33	7850	450	0.9	293	1800

In the table above, E denotes Young's modulus, ν is Poisson's ratio, c_p is the specific heat, χ is the Taylor-Quinney coefficient, T_r is the reference temperature and T_m is the melting temperature.

3.2.1 Microstructure

The majority of all metals are made up entirely of small crystals in which atoms are packed in repeating three-dimensional patterns [54]. These metals are made up of several crystalline structures, which again is made up of the combination of lattice crystal and atoms. To get a better understanding of the different crystalline structures in steel, a brief introduction of allotropy is firstly made.

Allotropy

Allotropy is defined as the existence of two or more different physical forms of a chemical element in the same physical state [55]. At atmospheric pressure there exists three allotropes of iron: alpha-phase iron (α-Fe), gamma-phase iron (γ-Fe) and delta-phase iron (δ-Fe). Steel is an alloy of iron (Fe) and carbon (C), and the different allotropes of iron have different solubility of carbon. Thus it follows that different allotropes can be used to make different kinds of steel. The aforementioned allotropes are further presented for a basic comprehension as well for completeness. The definitions are taken from [56].

- **Delta-phase iron**: As molten iron cools, it solidifies at 1538°C. In this form it is called δ-Fe and has a body-centered cubic (BCC) crystal structure (see Figure 3.1a). δ-Fe can dissolve up to 0.08% of carbon by mass.
- **Gamma-phase iron**: When the molten iron cools further to 1394°C its lattice structure changes to a face centered cubic (FCC) lattice structure (see Figure 3.1b). This form is called γ-Fe or *austenite*, and can dissolve as much as 2.04% of carbon by mass.
- **Alpha-phase iron**: By further cooling the molten mass to below 912°C, the iron again adopts the BCC structure, and in this form, it is called α-Fe or *ferrite*. Carbon dissolves rather poorly in this allotrope, with only 0.021% of carbon by mass.

Crystal Structures

As previously mentioned, by the inclusion of carbon to the iron allotropes, different steels are produced, which has different crystalline structures. These crystalline structures are built of a series of lattice crystals which can be viewed as points existing in space. There exists a total of seven lattice systems, with a total of four possible symmetry groups [57]. The general symmetry groups are primitive, base-centered, body-centered, and face-centered. It is worth noticing that not all lattice systems contain all symmetry groups.

There exist several different steel crystalline structures, but in this thesis, only two have been considered, namely *ferrite* and *martensite*, which will be briefly covered. These crystalline structures form the basis for the two materials examined in this thesis. The reader is referred to [57] and [54] for further reading on crystalline- and lattice structures, as well as the general topic of microstructure.

- **Ferrite**: Also known as α-phase iron, and is the principal constituent of carbon steels. It has a relatively low content of carbon, less than 0.005% at room temperature, and is a soft and ductile material that can easily be deformed [58].
- **Martensite**: In essence, martensite is ferrite supersaturated with carbon [58]. Martensite is formed by quenching of the austenite (γ-Fe) at such a high rate that carbon atoms do not have time to diffuse out of the crystal structure in large enough quantities to form cementite, which transforms to a body-centered tetragonal (BCT) form (depicted in Figure 3.1c), called martensite. Martensite has very high strength and hardness, but rather a low fracture resistance and ductility. The hardness and strength of martensitic steels are observed to vary linearly with the carbon content up to approximately 0.5% [59]. After this point, the hardness and strength of the material will decrease.

3.2.2 Basic Terminology

With a basic introduction to the microstructure and some of the micro-mechanics of steel, some basic terminology for the two Docol steels can briefly be introduced for completeness.

Alloy and Alloying Elements

Alloy is defined as a combination of metal and other metals or elements [60]. There exist a large amount of different alloying elements, each giving the alloy different properties. The alloying elements in Docol 600DL and 1400M are given in Table 3.2 and 3.3, respectively. The different alloying elements found in the materials, and their effects on the steel, will be shortly presented. The summary of alloying elements are taken from [61], [62] and [63].

- **Carbon (C)**: The most important alloying element in steel. Raises tensile strength, resistance to wear, and hardness. Decreases formability as well as the ductility and toughness.
- **Silicon (Si)**: Increases tensile- and yield strength, forgeability, and hardness. Used as a deoxidizer, which is important as oxygen is detrimental to steel-quality. Acts as a degasifier, removing dissolved gases from the molten steel.
- **Manganese (Mn)**: A deoxidizer and degasifier. Increases tensile strength, hardness, and hardenability. Reacts with sulfur to improve forgeability.
- **Phosphorus (P)**: Increases strength, machinability, and hardness, but without sufficient manganese, it produces brittleness. Decreases ductility and toughness.
- **Sulfur (S)**: Improves machinability. Without sufficient amounts of manganese present, it produces brittleness. Decreases ductility.
- **Aluminium (Al)**: Used for deoxidizing, and for refining grains, which increases ductility and impact resistance.
- **Niobium (Nb)**: Used as a stabilizing element. Increases the toughness, strength, and formability.
- **Titanium (Ti)**: Used as a stabilizing element.

Strength Grading of Steel

High-Strength steel (HSS) is defined as steel with a yield strength subceeding approximately 550 MPa [64]. Advanced high-strength steel (AHSS) is defined as steel with a yield strength exceeding 550 MPa and can be classified as ultra-high-strength steel (UHSS) if the tensile strength exceeds 780 MPa [65].

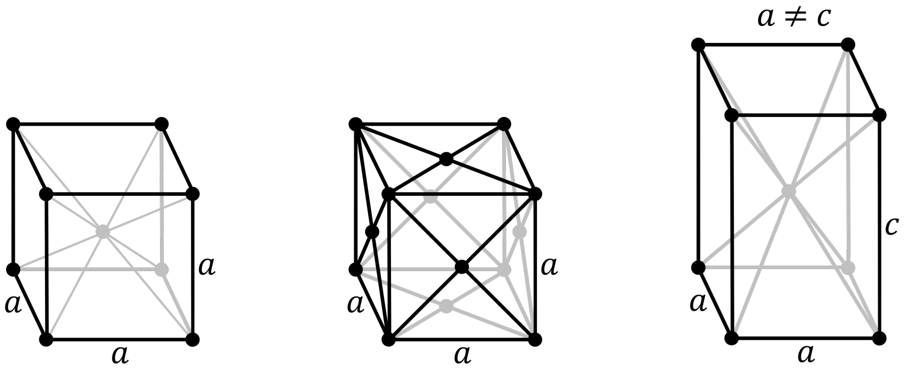

(a) BCC. **(b)** FCC. **(c)** BCT.

Figure 3.1: Different lattice structures. (3.1a) Body Centered Cubic [66], (3.1b) Face Centered Cubic [67], and (3.1c) Body Centered Tetragonal lattice structures [68].

Cold Rolling/Reduced

Takes place after the steel has been hot rolled. When the steel is being hot rolled, it is warmed up, and rolled back and forth through a mill until acquiring the desired shapes and dimensions. Cold rolling does not alter the shape of the steel but reduces the thickness and work hardens the steel. The result is a hard sheet of steel with less ductility than hot rolled steel.

Annealing

Increases the ductility and reduce the hardness of the steel, making it more workable. Done by increasing the temperature, which may alter the physical- and chemical properties of the material itself, reverting it to pre-cold-worked states [69]. This process includes: **recovery** - relief of some internal strain energy. **Recrystallization** - formation of new sets of strain-free grain. And **grain growth** - increase in average grain size.

Dual-phase Steel

Dual-phase steel has a ferrentistic-martensitic microstructure, where islands of hard martensite are embedded in a tougher continuous ferrite [70]. This composition gives the steel the characteristics of both crystalline structures.

Namely the toughness, ductility and fracture resistance from the ferrite, and the hardness and high strength from the martensite.

3.2.3 Docol 600DL and Docol 1400M

Table 3.2: Chemical composition of Docol 600DL (in wt. %). Taken from [71].

C	Si	Mn	P	S	Al_{tot}
0.10	0.40	1.50	0.010	0.002	0.040

Docol 600DL is cold reduced dual-phase steel, available in thicknesses from 0.5 mm to 2.1 mm and widths from 800 mm to 1500 mm. It has a reported yield strength between 280 MPa and 360 MPa, and tensile strength between 600 MPa and 700 MPa [71], which classifies it as an HSS. The chemical composition is given in Table 3.2. Docol 600DL gets its hardenability and toughness from the ferrite, with the martensite providing the material with strength and hardness.

Table 3.3: Chemical composition of Docol 1400M (in wt. %). Taken from [72].

C	Si	Mn	P	S	Al_{tot}	Nb	Ti
0.17	0.20	1.40	0.010	0.002	0.040	0.15	0.25

Docol 1400M is a cold rolled martensitic steel, available in the same thicknesses as for Docol 600DL. It has a minimum yield strength of 1150 MPa, and tensile strength in the range 1400 MPa to 1600 MPa [72], which classifies it as an AHSS. The chemical composition is given in Table 3.3. As it is purely martensitic, it has low ductility and toughness, but rather high strength.

The minimum yield- and tensile strength of Docol 1400M is observed to be approximately 75.6% and 57.1 higher than that of Docol 600DL, respectively. Docol 600DL will therefore obviously exhibit yielding first, but it also possesses a better hardenability and toughness on account of the ferrite. In addition, the Docol 600DL is more ductile than 1400M.

3.3 Constitutive Models

A constitutive model is a relation between two physical quantities, which are material specific. Such a model is essential when conducting a numerical study as it describes the stress-strain relation in response to applied loading. The model takes in the material constants in Table 3.1 as well as some model parameters, which will be presented in further detail in Section 3.4.

3.3.1 Model Assumptions

The model assumptions made in this thesis were isotropic material behavior, no kinematic hardening, small elastic strains, and finite strains and rotation. The material was further assumed to undergo large plastic deformations as a result of blast loading, as this is a widely global problem. The materials were expected to experience strain hardening and temperature softening. For blast loading, isothermal conditions were assumed, whereas adiabatic conditions were assumed for impact loading. The transition from elastic- to plastic behavior was assumed to be governed by the Hosford yield function.

3.3.2 Yield Criterion

When establishing a numerical model, the plastic response will be the most detrimental. It is therefore desirable to establish a criterion that can accurately depict plasticity for the model. This is done by using a yield criterion. The material is said to behave elastically until the yield surface is reached. In the plastic domain, a new set of governing equations are needed, which will be established in this chapter. The yield criterion takes on a value less than zero when the behavior is elastic, and a value of zero when yielding is initiated. This criterion can be expressed as

$$f(\sigma_{ij}) = \phi(\sigma_{ij}) - \sigma_Y \tag{3.1}$$

where ϕ is the yield function, and σ_Y is the current yield stress. The yield function can be introduced in order to characterize the magnitude of the stress state. In the following, the Hosford yield function is presented, which is a high-exponent yield function.

This function is given as [73]

$$\phi(\sigma_{ij}) = \sqrt[n]{\frac{1}{2}((\sigma_I - \sigma_{II})^n + (\sigma_{II} - \sigma_{III})^n + (\sigma_{III} - \sigma_I)^n)} \tag{3.2}$$

where $\sigma_I \geq \sigma_{II} \geq \sigma_{III}$ are the ordered principal stresses and n is a coefficient controlling the shape of the yield surface. It is observed that the von Mises yield surface is a generalization of the expression above when n=2. Further, for n→ 0 and n→ ∞ the Tresca yield surface is obtained.

3.3.3 Work Hardening

When metals are subjected to plastic deformation, the strength of the material will increase. For isotropic hardening, this can be visualized as the size of the yield surface increases. The expansion of the yield surface is depicted in Figure 3.2.

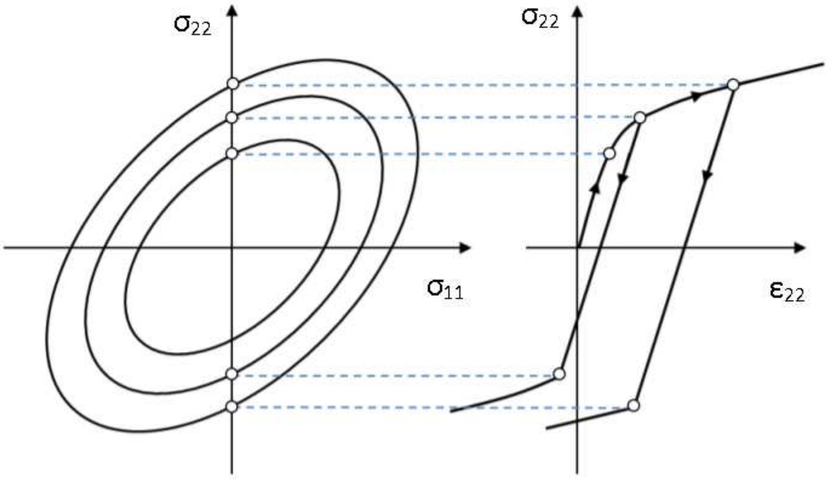

Figure 3.2: Depiction of how the yield surface expands when assuming isotropic hardening. The image is taken from [43].

To be able to include work-hardening of the material, the yield criterion in Equation 3.1 need to be modified. An isotropic work-hardening function has to be prescribed.

Including a work-hardening function, the yield function takes the following form

$$\phi(\sigma_{ij}) = (\sigma_0 + R(p)), \ where \ \sigma_Y = \sigma_0 + R(p) \tag{3.3}$$

where σ_0 denotes the initial yield stress, and R=R(p) is the work-hardening function, which is a function of the equivalent plastic strain p. To establish the work-hardening function, a hardening law must be applied. The most common laws are the Power law and the Voce rule, which are given as

$$R(p) = Bp^n \quad and \quad R(p) = \Sigma_{i=1}^{n} Q_i(1 - exp(-C_i p)) \tag{3.4}$$

respectively. Where B, C_i and Q_i are calibrated model parameters. In this thesis, the extended Voce rule with two terms was selected.

3.3.4 Thermal Softening

When a material is subjected to rapid plastic deformation, heat is generated due to plastic dissipation, which has no time to diffuse. Consequently, the temperature will increase locally where the plastic deformations are large. This is classified as adiabatic heating and is observed in impact loading. An increment in the temperature can be written as

$$dT = \frac{\chi}{\rho c_p} dW_p \tag{3.5}$$

where dW_p is the plastic work increment per unit volume, χ is the Taylor-Quinney coefficient, c_p is the specific heat capacity, and ρ is the density of the material. The Taylor-Quinney coefficient determines the fraction of the plastic work that is dissipated as heat and is typically selected as 0.9 for metals [42], as some strain energy is stored in the lattices during plastic deformation, which is recovered upon unloading. To account for thermal softening it is beneficial to introduce the homologous temperature, which is given as

$$T^* = \frac{T - T_0}{T_m - T_0} \tag{3.6}$$

where T is the current temperature, T_m is the melting temperature of the material and T_0 is a reference temperature which is typically set to 293 K.

The yield function can now be rewritten as a function of the homologous temperature, which gives

$$\phi(\sigma_{ij}) = (\sigma_0 + R(p))(1 - (T^*)^m) \tag{3.7}$$

where m is a constant that reflects the temperature sensitivity of the material. The constant may be determined by material testing at different temperatures.

3.3.5 Rate Dependency

Up until this point, the yield function has not taken rate dependency into account. This is obtained by allowing the stress to move outside the yield surface, thus obtaining viscoplasticity. As a consequence of this, the following needs to be employed:

$$\begin{aligned} \text{f} \leq 0 \implies & \text{ elastic domain} \\ \text{f} > 0 \implies & \text{ plastic domain} \end{aligned}$$

To account for the rate dependency, the Norton creep law can be applied, and the yield function can be written on the following form

$$\phi(\sigma_{ij}) = (\sigma_0 + R(p))(1 + \dot{p}^*)^c \quad for \quad f > 0 \tag{3.8}$$

where $\dot{p}^* = \frac{\dot{p}}{\dot{p}_0}$ is the dimensionless plastic strain rate, $\dot{p}_0$ is a reference strain rate and c is a constant that governs the strain rate sensitivity of the material, which can be found by conducting material tests at several strain rates. The rate dependency should vanish for quasi-static strain rates.

3.3.6 Modified Johnson-Cook

Having established the different relations in the previous sections, the yield criterion, work hardening, thermal softening, and rate dependency can be combined into a single expression for the equivalent stress. The result of this is the Modified Johnson-Cook constitutive relation (MJC).

The expression for the yield function expressed with the MJC read

$$\phi(\sigma_{ij}) = (\sigma_0 + R(p))(1 + \dot{p}^*)^c(1 - (T^*)^m) \quad for \quad f \geq 0 \tag{3.9}$$

It is worth noticing that the MJC constitutive relation is not a complete material model as it cannot predict fracture or failure of the material. Consequently, a failure criterion needs to be prescribed.

3.3.7 Ductile Fracture

For steel, fracture can be divided into two: namely brittle- and ductile fracture. Brittle fracture occurs at small or no plastic deformation prior to fracture and mainly occurs in high-strength materials with poor toughness and ductility [74]. In this thesis, the two materials are assumed to fail in a ductile manner.

Microscopic voids are present in the material as a result of the manufacturing process. When the particles reach a sufficiently high local stress, voids are nucleated [42]. As the material is damaged further, the voids will grow and coalescence with each other, which in turn could lead to ductile fracture. This is depicted in Figure 3.3.

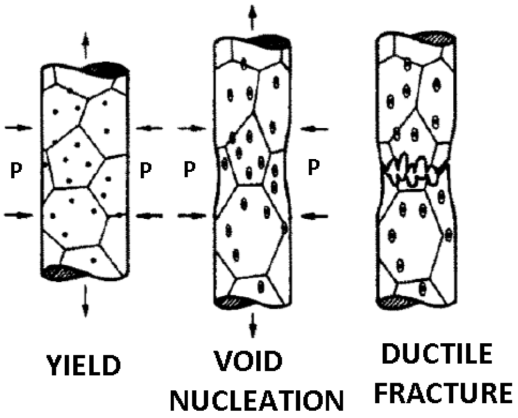

Figure 3.3: Ductile damage and fracture by nucleation, growth and coalescence of voids. Image is take from [42].

Cockcroft-Latham Failure Criterion

It is assumed that the damage evolution is driven by plastic straining, but amplified with a factor that accounts for the stress state. The CL criterion can be expressed as

$$D = \frac{1}{W_c} \int_0^p max(\sigma_I, 0)dp \tag{3.10}$$

where D is the damage variable (failure assumed to occur when D=1), and W_c is the fracture parameter, which is the amount of plastic work experienced by the material when loaded to fracture.

3.4 Material Testing

Material testing is important in order to determine model parameters for a given constitutive relation, as well as material properties. Therefore, numerous studies have employed material testing. The material behaviour of Docol 600DL and 1400M were studied by Gruben *et al.* (2016) [53] on 1.8 and 1 mm thick plates, respectively. The behaviour of Docol 600DL was studied by Råkvag *et al.* (2013) [6] on 0.7 mm thick plates, and by Holmen *et al.* (2014) [75] on 0.8 mm thick plates. The material tests were performed using uniaxial tension tests, and Rakvåg [6] also used Split-Hopkins tests. The model parameters for Docol 600DL and 1400M are given in Table 3.4. The reader is further referred to [6],[76], [53], [75], [74] for more comprehensive and complete presentations of material testing.

These studies concluded that isotropy could be assumed, all though some anisotropy was observed using different material orientations. It was also observed that the thinner the steel plates, the more anisotropy they exhibited. This was also observed by Björklund (2012) [74], who found that 1.46 mm thick Docol 600DP and 1.48 mm thick 1200M steel plates exhibited anisotropy. He proposed that an anisotropic fracture model should be applied to accurately predict fracture for different material directions.

Table 3.4: Model parameters for the modified Johnson-Cook constitutive relation taken from the litterature. Docol 600DL taken from [31] and Docol 1400M from [53].

Material	A [MPa]	Q_1 [MPa]	C_1 [-]	Q_2 [MPa]	C_2 [-]	c [-]	m [-]	$\dot{p}_0$ [s^{-1}]	W_c [MPa]
600DL	325.7	234.8	56.2	445.7	4.7	0.01	1	$5*10^{-4}$	555
1400M	1200	253.6	773.5	97	135	0.004	6	$1*10^{-3}$	741

It is worth noting that the model parameters for Docol 1400M are calculated for a dog-bone specimen with a thickness of 1 mm, and thus not entirely accurate. Further, m in the table above for Docol 1400M is the coefficient controlling the shape of the yield surface (denoted as n in this thesis), and is not associated with the thermoplastic term of the MJC. It has further been assumed that m is equal to unity for Docol 1400M as well.

The difference in response of the two materials when undergoing quasi-static loading is presented in Figure 3.4. Here, the loading rate was constant and equal to 4 mm/min. From the figure, it observed that the strain hardenability of Docol 600DL is significantly better than for Docol 1400M, which as previously stated is due to the ferrite in the dual-phase steel. In addition, it is seen that Docol 1400M experiences fracture at a lower strain, which is linked to Docol 1400M being a less ductile material than Docol 600DL.

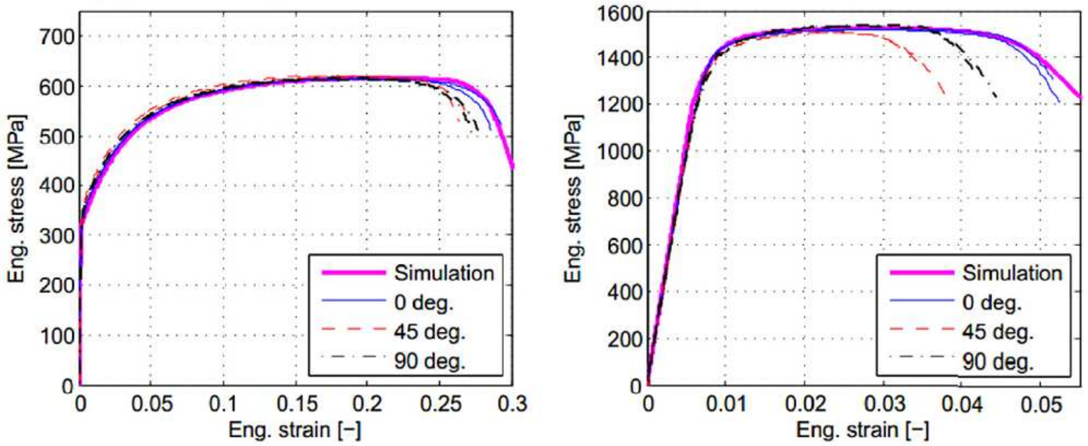

Figure 3.4: Uniaxial tension test at a quasi-static strain rates. Docol 600DL (left) and Docol 1400M (right). Figure is taken from [53].

Chapter 4

Preliminary Study

4.1 Introduction

In this chapter, a preliminary numerical study has been conducted using shell elements and perfectly circular holes with a diameter of 8 mm for the ballistic perforations. This study aims to get an approximate capacity of the perforated plates, which will serve as a basis when selecting the firing pressure in the experimental work. A further aim is to establish the differences between Docol 600DL and 1400M when exposed to blast loading, in terms of total global deformation and capacity.

The blast loading applied in this study was in the range of 25 to 75 bar, and have been idealized through pressure-time curves obtained by Aune *et al.* (2016) [37]. The loading curves were determined by exposing a 5 mm thick steel plate to nominal pressures of a given magnitude, and the pressure was sampled by a series of sensors. A Friedlander curve, see Section 2.6, was then fitted to the data. Nominal pressures of 35 were selected as the initial starting point for all configurations in this study.

4.2 Models

The models were modelled after the blast-exposed area in the shock tube (SSTF), i.e., a square of 300 mm x 300 mm. As the clamping frame which holds the plates in place in the SSTF were excluded from this thesis and the plates are geometrically simple, the outer boundaries were modelled as fixed. All configurations in this study were symmetric about the two in-plane axes. Therefore, only a quarter of the plates was modelled, which significantly reduced computational time. This was a valid assumption as there exists little to no difference in modelling a full plate with such simple geometry [7].

The labeling convention used in this study is shown in Table 4.1. It specifies the material, the configuration of the plate, element type used (restricted to S4R for this study), element size, and blast-loading applied. The general label name is given on the form ***DMMM_CC_XX_YY_phh_tt***.

Table 4.1: Naming convention used to label different models in the preliminary numerical study. General label name: ***DMMM_CC_XX_YY_phh_tt***.

Part of Name	Possible Configurations	Explanation
MMM	600	Docol 600DL
	1400	Docol 1400M
CC	FP	Full Plate
	CHX	Circular Holes, geometry X
XX	S4R	Shell element, reduced integration
YY	0xx	Mesh size of 0.xx mm
	xx	Mesh size of x.x mm
phh_tt	p77_tt	hh = driver length [cm]
		tt = nominal firing pressure [bar]

The model parameters used in this study are presented in Table 4.2. The only difference between these parameters and the ones presented in Table 3.4, is that m=1 for Docol 1400M. With m=6, the model would exhibit extreme strain softening. It is worth noticing that Abaqus runs using the von Mises yield surface, whereas the model parameters for Docol 1400M were fitted to the experimental data using the Hosford yield function with a coefficient of n=6. This is a yield surface somewhere in between the von Mises and Tresca yield surface.

Table 4.2: Model parameters used in the preliminary study.

Material	A [MPa]	Q_1 [MPa]	C_1 [-]	Q_2 [MPa]	C_2 [-]	c [-]	m [-]	$\dot{p}_0$ [s^{-1}]	W_c [MPa]
600DL	325.7	234.8	56.2	445.7	4.7	0.01	1	$5*10^{-4}$	555
1400M	1200	253.6	773.5	97	135	0.004	1	$1*10^{-3}$	741

For this study, there was a total of four different configurations, namely the FP-, CH1-, CH2- and CH3 configuration. The FP configuration is defined as a full plate. A short presentation is given for each of the CHX configurations:

- **CH1**: Has one perfectly circular hole of diameter 8 mm placed in the center of the plate.
- **CH2**: Has a total of four circular holes placed at a distance of 60 mm between each adjacent hole, forming a square of 60 mm x 60 mm between the holes, with the midpoint of the plate in the center.
- **CH3**: Has a total of four circular holes placed at a distance of 120 mm between each adjacent hole, forming a square of 120 mm x 120 mm between the holes, with the midpoint of the plate in the center.

4.2.1 Shell Element Models

The advantages of using shell element models are that they have considerable lower run-time compared to solid element models. They have one only element over the thickness and are not ideal for describing crack propagation and fracture. They are not able to predict stresses perpendicular to the thickness, but as blast loading is dominated by membrane stress, shell elements are a logical choice, especially for the full plate configuration. The shell elements used in this study was the quadratic S4R element. This element utilizes reduced integration, shear- and membrane locking, drilling stiffness, hourglass control and is a general-purpose element that is suitable for a wide range of applications for both thin- and thick shells [47].

Meshing

The meshing of the models was done using element sizes in the range of 0.8 mm to 4 mm. For meshing of shell element models, it is imperative that the element sizes used not are smaller than the thickness of the modelled plate as this violates the shell element theory, which in turn cause inaccurate results. The meshing of the FP- and CH1 configuration was done using the structured meshing algorithm which applies a structured mesh to an assigned region. The precursor for a structured mesh is that the region is geometrically simple [77]. The structured mesh of the CH1 configuration using an element size 0f 0.8 mm is depicted in Figure 4.1. A red dot indicates the reference point for displacement histories for this configuration.

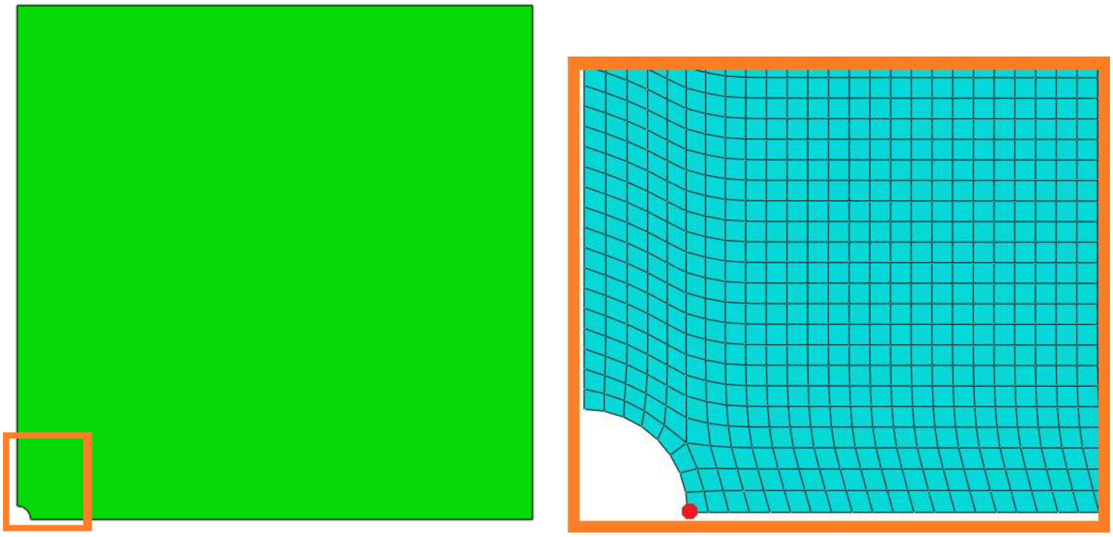
(a)

(b)

Figure 4.1: Partitioning and meshing of the CH2 configuration using an element size of 0.8 mm. (4.1a) Shows the partitioning of the CH1 configuration and (4.1b) shows a close-up of the mesh around the circular hole. The red dot indicates the location of the node used as a reference point for displacement histories for the CH1 configuration.

For the meshing of the CH2- and CH3 configuration, structured meshing was not sufficient as it leads to distorted and small elements, which lead to a smaller critical time step, and incorrect results. Therefore, the model needed to be partitioned in order to get a valid mesh.

The partition of the two configurations are depicted in Figure 4.2a for an element size of 0.8 mm. The green area represents the structured meshing algorithm, whereas the yellow area represents the sweep meshing algorithm [77]. The red dot indicates the location of the node used for midpoint displacements.

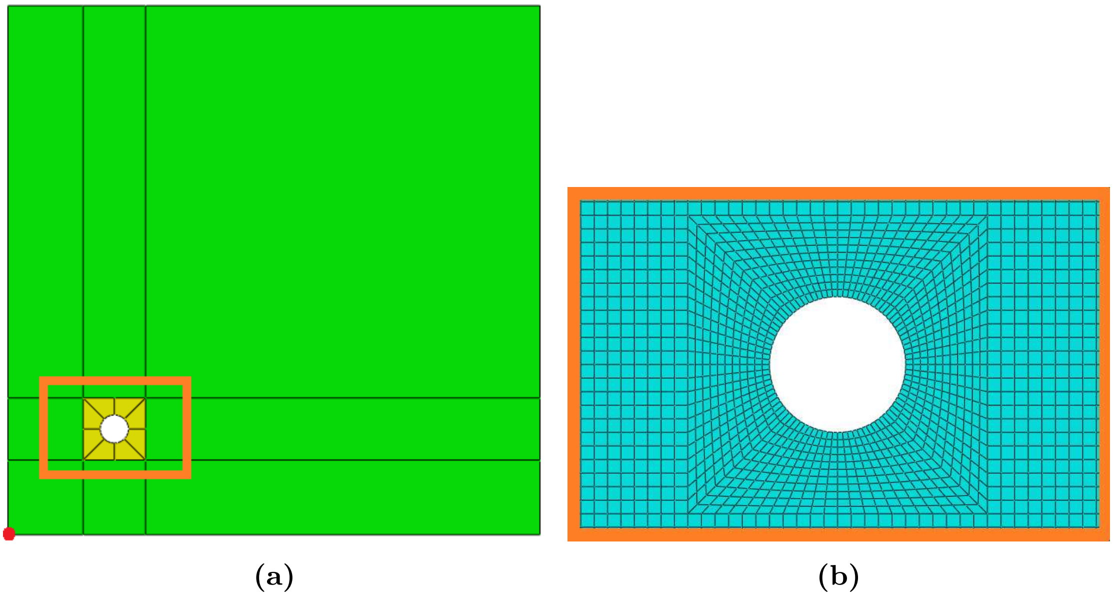
(a) (b)

Figure 4.2: Partitioning and meshing of the CH2 configuration using an element size of 0.8 mm. (4.2a) Shows the partitioning of the CH2 configuration and (4.2b) shows a close-up of the mesh around the circular hole. The red dot indicates the location of the node used as a reference point for midpoint displacements for the CH2- and CH3 configuration.

4.3 Results

The results are presented after configuration and include time-displacement curves of the reference point and energy plots. As the majority of the energy plots showed an artificial strain ratio below the recommended limit of 2% [40] and all total energy plots showed only negligible deviations from constant, only a handful of these plots are presented in this chapter. The remaining plots can be found in Appendix A.1.

4.3.1 Full Plate Configuration

The numerical results were plotted against the experimental data to give an illustration of the accuracy of the simulations. The experimental data are plotted in black and are marked with "*Experimental data*". The data for Docol 600DL was obtained from Granum and Løken (2016) [7], and the data for Docol 1400M was obtained from Sigstad and Kristiansen (2019) [78].

Figure 4.3a shows the displacement histories at 35 bar for Docol 600DL, where it is observed that the numerical response is identical to that of the experimental data. Figure 4.3b shows the time-deflection curves at 60 bar. Here it is observed that the numerical response is stiffer than the experimental data, but it can be concluded to be a good approximation. From these figures, it is also observed that the maximum deflection occurs before 2 ms and that oscillations are negligible. Therefore, the simulation time was cut to 5 ms for all further simulations using Docol 600DL in order to save computational expenses. Further, it is observed that the difference between element sizes is negligible for the FP configuration. Consequently, further simulations conducted for the FP configuration using Docol 600DL were run using an element size of 0.8 mm, as a more refined mesh provides the most accurate results.

Figure 4.3c and 4.3d shows the ratio of the artificial energy (ALLAE) divided by the internal energy (ALLIE) for 35 and 60 bar, respectively, for Docol 600DL. From the figures, it is observed that the ratios stay under 0.082% for 35 bar and under 0.042% for 60 bar, which is well under the recommendation [40]. The total energy in the model have been plotted in Figure 4.3e for 35 bar, and in Figure 4.3f for 60 bar. Here, it is observed that the ratio oscillates, but the requirement of constant energy is fulfilled as the energy deviations are so insignificant.

Figure 4.4a and 4.4b shows the time-deflection for Docol 1400M at 35 and 60 bar, respectively. Here, it is observed that the simulations differ from the experimental data to a larger extent than for Docol 600DL. It is seen that the numerical response is stiffer and exhibit more oscillations than the experimental response. It is further observed that the differences between element sizes are more significant, which diminishes with increasing pressure, along with the exaggerated oscillations. This suggests that the oscillations may be caused by an exaggerated elastic rebound of the material. It is also worth noticing that other factors could contribute to this response, such as the modelling of the boundaries and the applied loading.

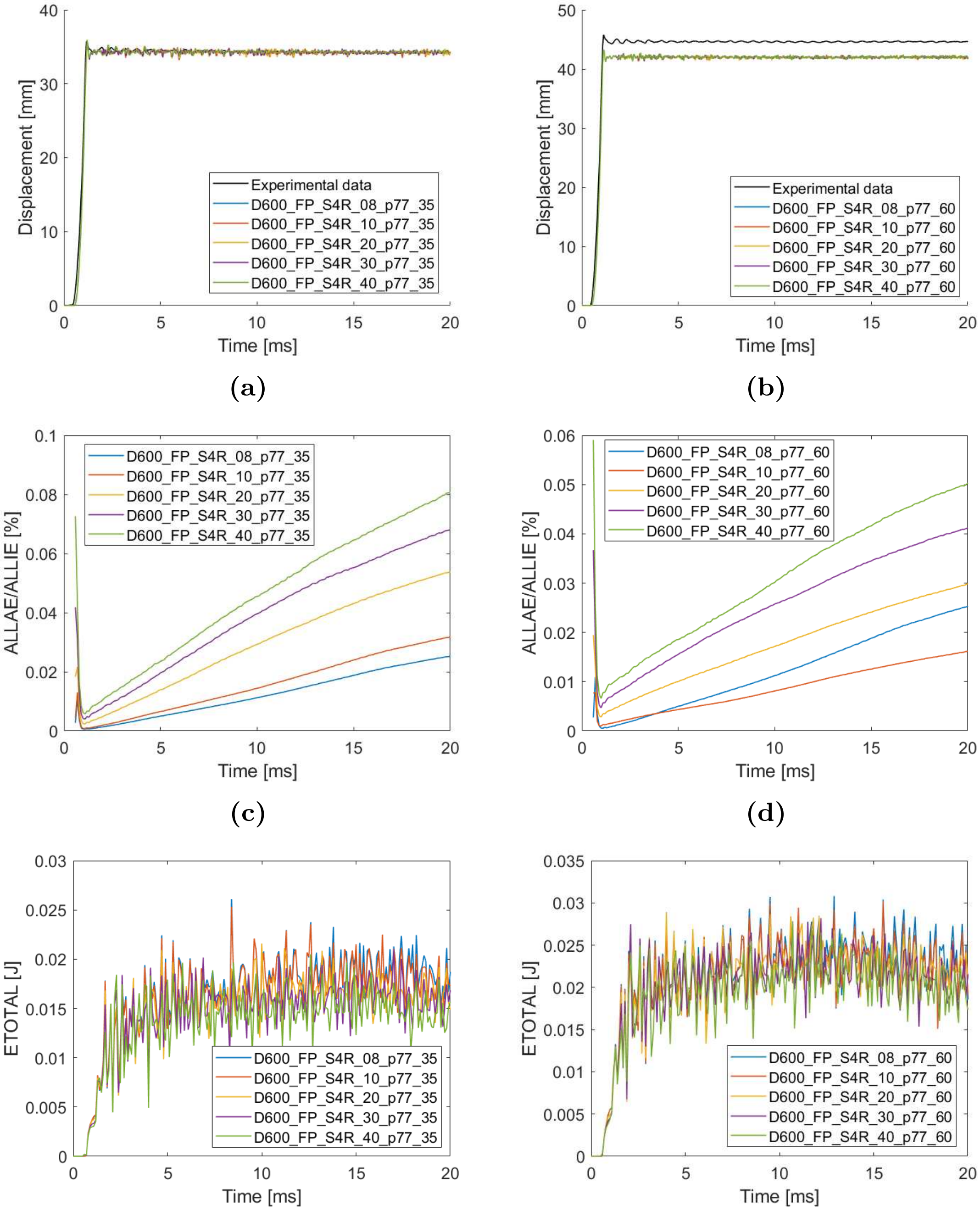

(a) (b)

(c) (d)

(e) (f)

Figure 4.3: Results obtained for the Docol 600DL FP simulations at 35 bar and 60 bar. (4.3a) And (4.3b) shows the displacement history at 35 and 60 bar, (4.3c) and (4.3d) shows the artificial strain energy ratio at 35 and 60 bar, and (4.3e) and (4.3f) shows the energy balance at 35 and 60 bar.

From comparison of Figure 4.4c and 4.4d, which depicts the ratio of artificial energy for Docol 1400M at 35 and 60 bar, it is observed that the ratio decreases as the pressure is increased. This complies with the displacement histories, and an elevated artificial strain ratio may explain the exaggerated oscillations. Comparing the ratios for the two materials, it is seen that the ratios are approximately 15-20 times higher for Docol 1400M, which again can be linked to oscillations.

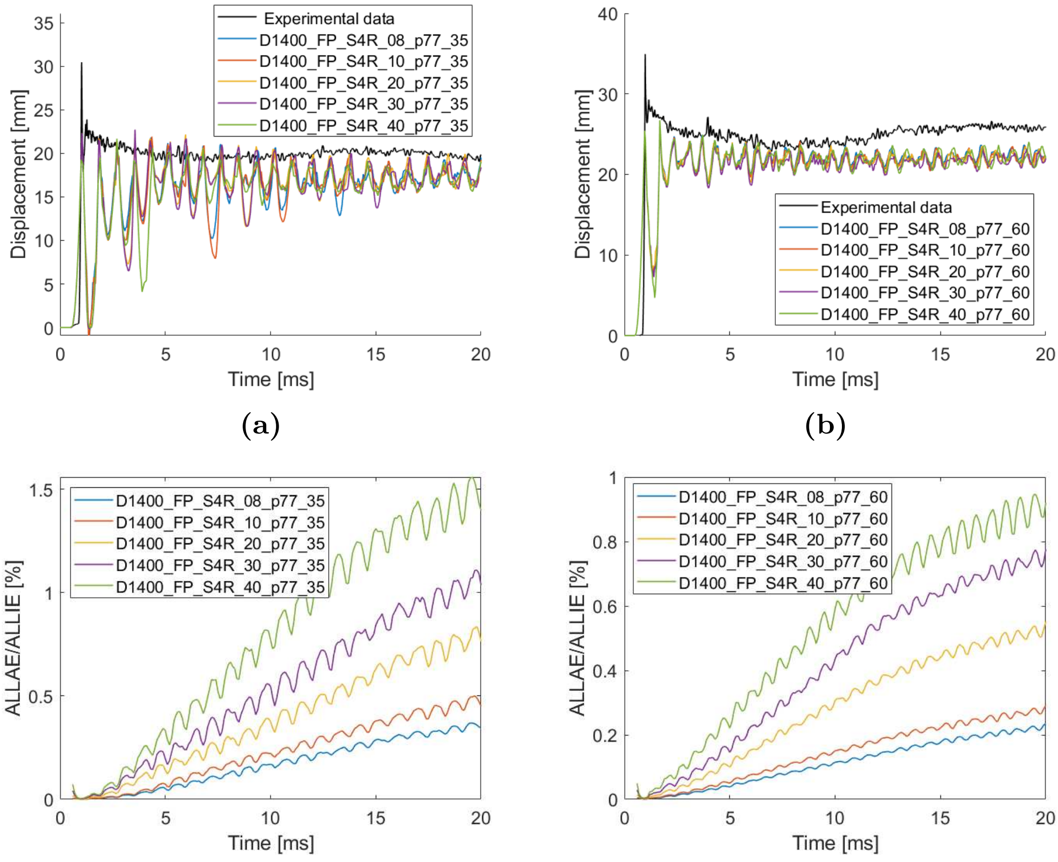

(a) (b)

(c) (d)

Figure 4.4: Results obtained for the Docol 1400DL FP simulations at 35 bar and 60 bar. (4.4a) And (4.4b) shows the displacement histories at 35 and 60 bar, and (4.4c) and (4.4d) shows the artificial strain energy ratio at 35 and 60 bar.

The mean displacement calculated for both materials at 35 and 60 bar is presented in Table 4.3. The mean displacement was taken as the average in a time interval of 5 ms where oscillations were deemed minimal.

From the table, it is observed that the mean displacement for Docol 600DL is on average approximately 50% greater than that of the Docol 1400M at 35 bar and approximately 52% greater at 60 bar.

Table 4.3: Mean midpoint displacement measured for the FP configuration using Docol 600DL and 1400M at 35 and 60 bar. The mean displacements were taken as the average displacement in a time interval of 5 ms where there were minimal oscillations.

Model Name	**Mean Displacement** [mm]	**Crack Length** [mm]
D600_FP_S4R_08_p77_35	33.98	No crack
D600_FP_S4R_10_p77_35	33.98	No crack
D600_FP_S4R_20_p77_35	33.95	No crack
D600_FP_S4R_30_p77_35	33.99	No crack
D600_FP_S4R_40_p77_35	33.65	No crack
D600_FP_S4R_08_p77_60	41.68	No crack
D600_FP_S4R_10_p77_60	41.68	No crack
D600_FP_S4R_20_p77_60	41.63	No crack
D600_FP_S4R_30_p77_60	41.66	No crack
D600_FP_S4R_40_p77_60	41.69	No crack
D1400_FP_S4R_08_p77_35	17.16	No crack
D1400_FP_S4R_10_p77_35	16.96	No crack
D1400_FP_S4R_20_p77_35	17.28	No crack
D1400_FP_S4R_30_p77_35	17.08	No crack
D1400_FP_S4R_40_p77_35	16.68	No crack
D1400_FP_S4R_08_p77_60	22.15	No crack
D1400_FP_S4R_10_p77_60	21.95	No crack
D1400_FP_S4R_20_p77_60	21.91	No crack
D1400_FP_S4R_30_p77_60	21.58	No crack
D1400_FP_S4R_40_p77_60	21.92	No crack

Maximum Capacity of the Plates

This study was conducted to get a rough estimate of the blast load capacity of the plates. Simulations were firstly run at 75 bar, which is the highest calibrated pressure in the SIMLab shock tube facility (SSTF) at NTNU [37]. The oscillations were assumed to decrease further with an increase in pressure for Docol 1400M, and consequently, simulations were run at 5 ms.

The deflection curves are presented in Figure 4.5. Here it is observed that the materials deform in unison up until a given point, which is quite reasonable as both materials share the same elastic modulus E and material density ρ. From comparison with the experimental data for Docol 600DL, it is observed no significant differences besides the fact that the simulated response is a bit stiffer.

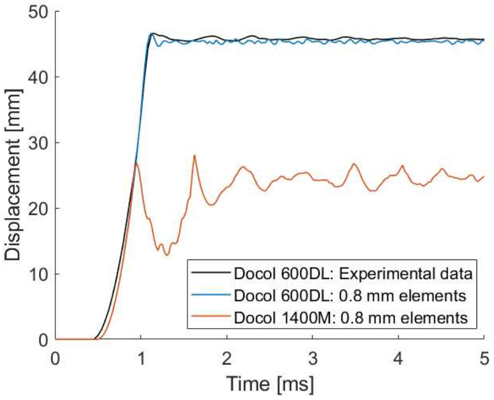

Figure 4.5: Displacement histories for Docol 600DL and 1400M at 75 bar.

The pressure was further increased by selecting a magnitude greater than unity using 75 bar, which resulted in a scaling of the pressure-time curve, and the estimated pressure could thus be taken as the magnitude multiplied with the measured reflected pressure from [37]. The estimated pressure at failure and magnitude is presented in Table 4.4. The capacity of Docol 600DL was approximately 15.4% greater than that of the Docol 1400M. As recalled from Section 3.2.3, Docol 1400M has minimum yield strength which is 75.6% greater than that of Docol 600DL. This highlights that strength does not dictate the blast resistance; other material properties must be considered as well.

Table 4.4: Magnitude of 75 bar and estimated pressure at which each plate fails.

Material	**1.1**	**1.2**	**1.3**	**Estimated Pressure** [kPa]
Docol 600DL	No failure	No failure	Failure	2184
Docol 1400M	Failure	Failure	Failure	1848

Baglo and Dybvik (2015) [79] studied the numerical capacity of full 0.8 mm thick Docol 600DL plates. They found an estimated failure pressure of 4200 kPa, which was 48% greater than the pressure of this thesis. In their study, they used shell elements with a size of 7.5 mm and W_c=815 MPa. They suggested that the response of the plate and the energy plots were inaccurate. They further argued that the mesh of the model was too coarse to fulfill previously established recommendations for element sizes using the CL fracture parameter. This highlights the fact that correct and concise model assumptions must be made, as this may severely affect the results.

Deformation Profiles

To compare the response of the materials, it was convenient to consider the deformation profiles. An element size of 0.8 mm was selected as it gave the most accurate depiction. The deformation profiles are presented in Figure 4.6a, 4.6b, 4.7a and 4.7b at 25, 35, 60 and 75 bar, respectively. The profiles have been plotted at different times. From observation, it is seen that the deformation patterns coincide up until a point. Here, Docol 600DL deformed further, whereas Docol 1400M started to oscillate. Elastic waves were observed to propagate through the width of the Docol 1400M plates, which can be seen as ripples. Further, Docol 1400M is seen to deform less than Docol 600DL, which is linked to it being a stronger material.

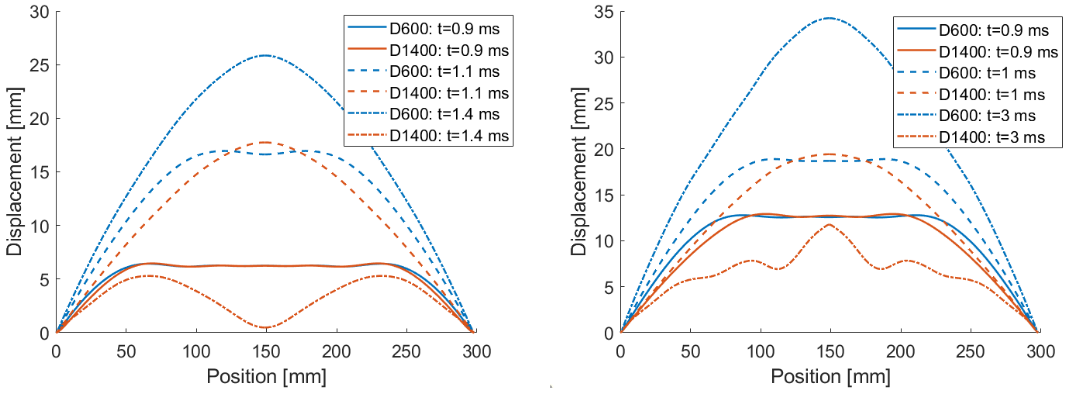

(a) 25 bar **(b)** 35 bar

Figure 4.6: Deformation profiles of the two materials at given times. (4.6a) Shows the deformation profiles at 25 bar and (4.6b) at 35 bar.

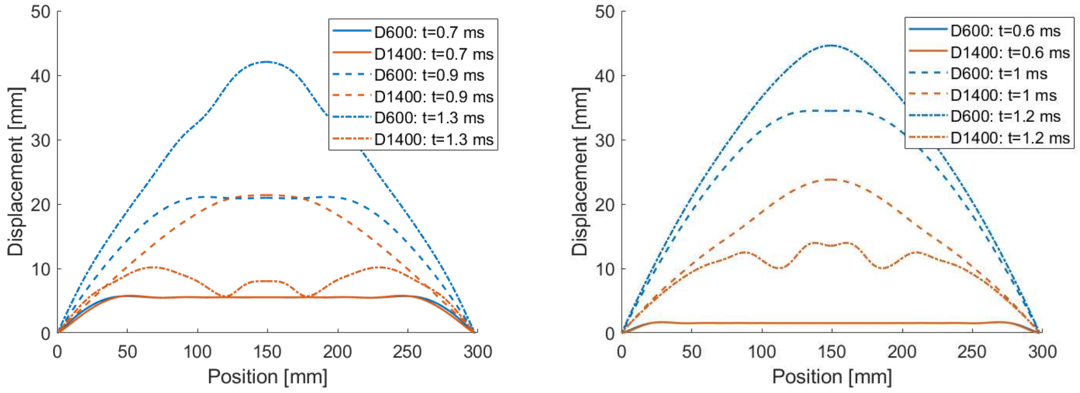

(a) 60 bar **(b)** 75 bar

Figure 4.7: Deformation profiles of the two materials at given times. (4.7a) Shows the deformation profiles at 60 bar and (4.7b) at 75 bar.

4.3.2 Circular Hole Configurations

As concluded in the previous section, the run-time for Docol 600DL was decreased to 5 ms. As there were no deviations between element sizes with respect to deflection for this material, simulations were run with an element size of 0.8 mm, 2 mm and 4 mm for Docol 600DL.

CH1 Configuration

For Docol 600DL, there was not observed any crack initiation or fracture at either 35 bar or 60 bar. At 35 bar the accumulated damage at the integration point (denoted by SDV_W in Abaqus) was equal to 281, which is approximately half of the critical value which has been calibrated to 555. By increasing the pressure to 60 bar, the accumulated damage had increased to 367.7, indicating that the plates were nowhere near the failing limit. The resulting displacement curves at 35 bar and 60 bar are presented in Figure 4.8.

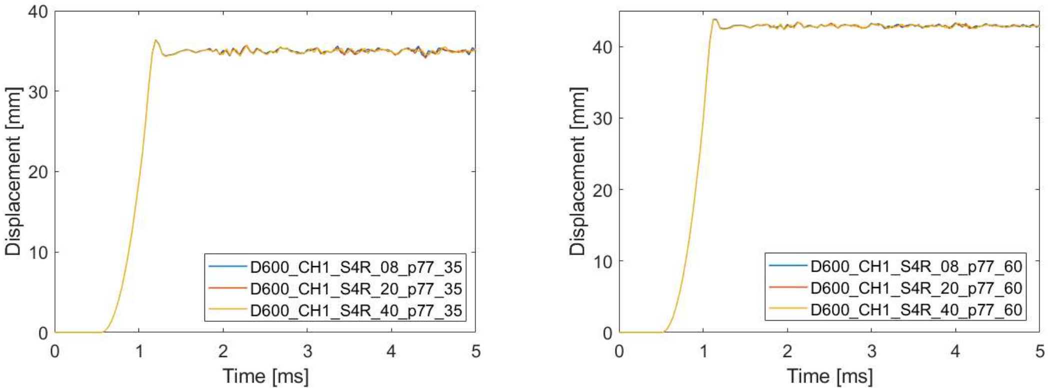

(a) 35 bar **(b)** 60 bar

Figure 4.8: Midpoint displacement histories obtained for the Docol 600DL CH1 simulations at 35 and 60 bar. (4.8a) And (4.8b) shows the displacement histories at 35 and 60 bar, respectively.

The Docol 1400M plates exhibited total failure at 35 bar, and the pressure was therefore decreased to 25 bar. No crack initiation or fracture was observed at this pressure level. The damage parameter was examined for all element sizes, and is presented in Figure 4.3.2 for an element size of 0.8 mm (left), 2 mm (center) and 4 mm (right). From the figure, it is observed that the accumulated damage diminishes as the element dimensions are increased, which is due to the accumulated damage being spread out over the entire element. The critical value has been calibrated to 741, indicating that the element sizes of 0.8 mm were close to fracture. Given a solid element model with a more refined mesh, the plate could have experienced fracture.

The displacement histories for Docol 1400M are presented in Figure 4.10a and the artificial strain ratios are plotted in Figure 4.10b. From the displacement histories, it is observed that the material oscillates heavily, strengthening the observations that a lower pressure induces more exaggerated oscillations. The spurious oscillations are reflected in the artificial energy plot where the coarsest elements are seen to violate the energy recommendation in Abaqus. Consequently, the validity of this model should be checked. The mean displacements for both materials are presented in Table 4.5.

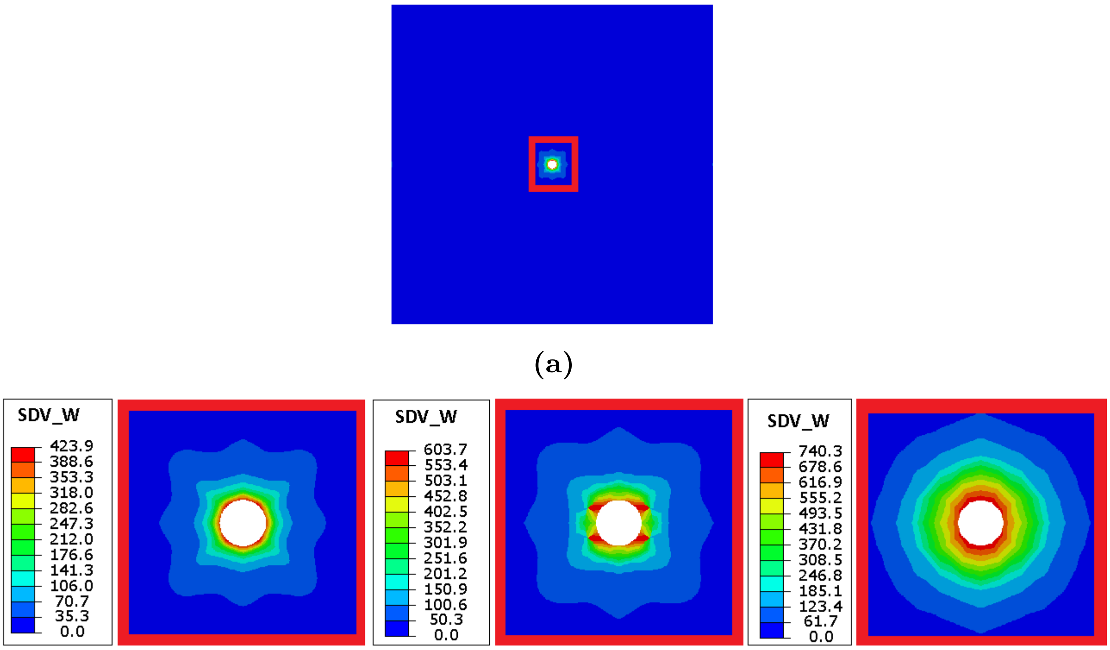

(a)

(b)

Figure 4.9: Damage accumulation for Docol 1400M using the CH1 configuration at 25 bar. (4.9a) Shows the entire evaluated configuration and (4.9b) shows a zoom-in of the previous image, depicting the accumulated damage using an element size of 0.8 mm (left), 2 mm (center) and 4 mm (right).

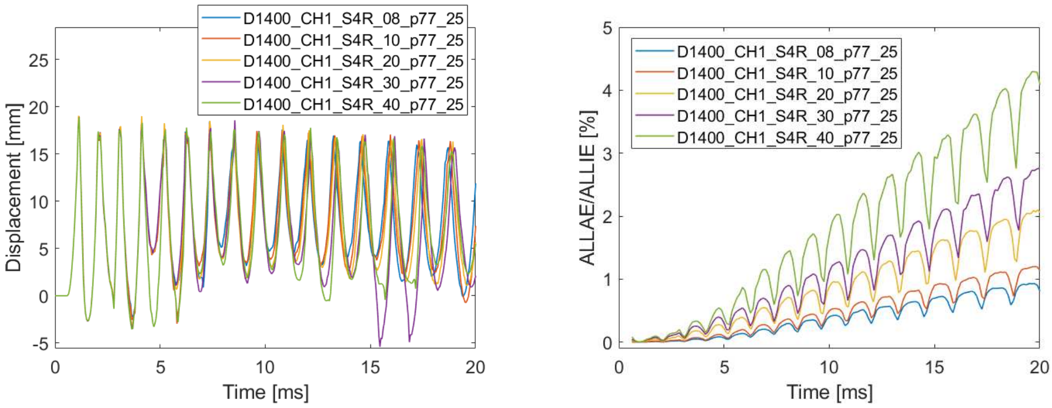

(a) **(b)**

Figure 4.10: Results obtained for the Docol 1400M CH1 configuration at 25 bar. (4.10a) Shows the displacement histories, and (4.10b) shows the artificial strain energy ratio.

Table 4.5: Mean midpoint displacements measured for the CH1 configuration using Docol 600DL and 1400M.

Model Name	**Mean Displacement** [mm]	**Crack Length** [mm]
D600_CH1_S4R_08_p77_35	34.67	No crack
D600_CH1_S4R_20_p77_35	34.64	No crack
D600_CH1_S4R_40_p77_35	34.64	No crack
D600_CH1_S4R_08_p77_60	42.52	No crack
D600_CH1_S4R_20_p77_60	42.49	No crack
D600_CH1_S4R_40_p77_60	42.50	No crack
D1400_CH1_S4R_08_p77_25	7.91	No crack
D1400_CH1_S4R_10_p77_25	7.88	No crack
D1400_CH1_S4R_20_p77_25	6.56	No crack
D1400_CH1_S4R_30_p77_25	4.42	No crack
D1400_CH1_S4R_40_p77_25	6.21	No crack
D1400_CH1_S4R_08_p77_35	Failure	Failure
D1400_CH1_S4R_10_p77_35	Failure	Failure
D1400_CH1_S4R_20_p77_35	Failure	Failure
D1400_CH1_S4R_30_p77_35	Failure	Failure
D1400_CH1_S4R_40_p77_35	Failure	Failure

CH2 Configuration

No crack initiations were observed at either 35 or 60 bar for Docol 600DL. The accumulated damage was 186 at 35 bar, and 312.9 at 60 bar. Comparing these values to that of the CH1 configuration it is observed a decrease of approximately 34% for 35 bar and 15% for 60 bar. For Docol 600DL, the displacement histories are presented in Figure 4.11a for both pressures. For Docol 1400M it was observed crack formation at 35 bar for element sizes of 0.8 mm, 1 mm and 2 mm. The crack formation is depicted in Figure 4.12 for an element size of 0.8 mm. It can be observed from the figure that the cracks propagate along the yield lines, towards the corners of the plate. It is worth noticing that these cracks may not be entirely correct, as the model- and fracture parameters were calculated using a different plate thickness and a different yield surface than von Mises. It is further worth noticing that shell elements do not accurately depict cracking. The displacement histories for Docol 1400M are presented in Figure 4.11b.

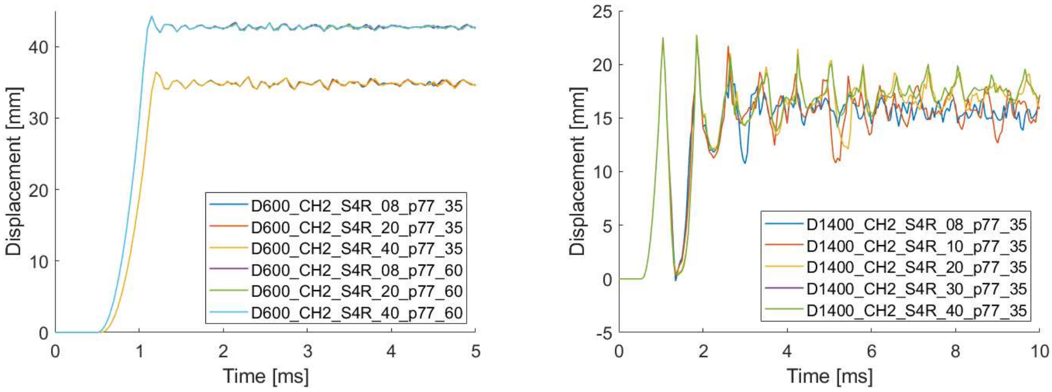

(a) **(b)**

Figure 4.11: Results obtained for CH2 configuration for both Docol 600DL and 1400M. (4.11a) Shows the displacement histories for Docol 600DL at 35 bar and 60 bar, and (4.11b) shows displacement histories for Docol 1400M at 35 bar.

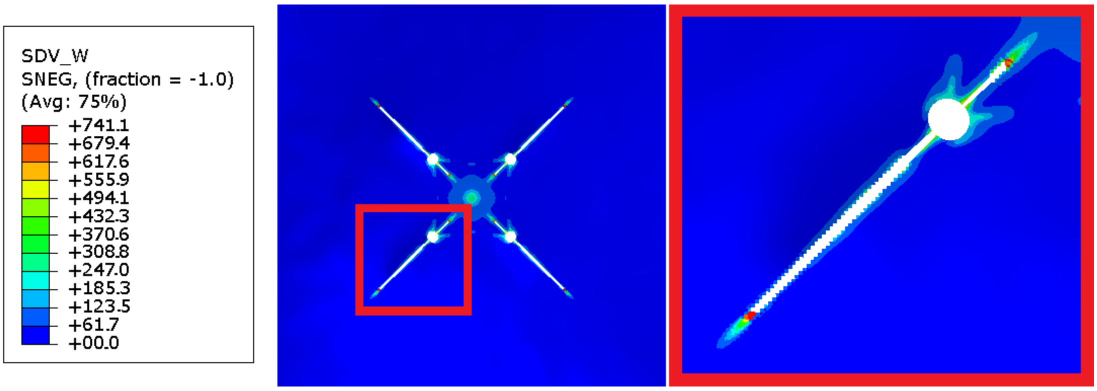

Figure 4.12: Damage accumulation and crack formation in the CH2 configuration using Docol 1400M at 35 bar. The figure depicts the crack formation in the entire plate (left) and a zoomed image of the lower left crack in the previous image (right).

The mean displacements for both materials, as well as the observed crack lengths for Docol 1400M, are presented in Table 4.6. From the table below it is observed that different element sizes give different crack lengths, which is solemnly due to the fact that finer elements accumulate the most damage in the integration points.

Table 4.6: Mean midpoint displacement measured for the CH2 configuration using Docol 600DL and 1400M.

Model Name	**Mean Displacement** [mm]	**Crack Length** [mm]
D600_CH1_S4R_08_p77_35	34.34	No crack
D600_CH1_S4R_20_p77_35	34.32	No crack
D600_CH1_S4R_40_p77_35	33.99	No crack
D600_CH1_S4R_08_p77_60	42.13	No crack
D600_CH1_S4R_20_p77_60	42.09	No crack
D600_CH1_S4R_40_p77_60	42.10	No crack
D1400_CH1_S4R_08_p77_35	15.40	75
D1400_CH1_S4R_10_p77_35	15.61	41.7
D1400_CH1_S4R_20_p77_35	16.97	5.8
D1400_CH1_S4R_30_p77_35	17.31	No crack
D1400_CH1_S4R_40_p77_35	17.31	No crack

CH3 Configuration

For Docol 600DL, there were negligible differences in the displacements using different element sizes for all tested configurations. For Docol 1400M, it was observed that the difference between element sizes increased with decreasing pressure. Based on this, it was decided that this configuration should be run only using an element size of 0.8 mm, as smaller elements better depict damage evolution and that the deflection using this element size was assumed to be the most accurate.

For Docol 600DL there was observed no crack forming at either pressure levels. The accumulated damage was 117.2 for 35 bar and 191 for 60 bar. By comparison with the CH1 configuration, the decrease of this parameter was observed to be 37% for 35 bar and 39% for 60 bar. For Docol 1400M there were no crack initiations at 35 bar, and the accumulated damage was equal to 702. Increasing the pressure to 60 bar the entire plate failed, where cracks were observed to propagate along the yield lines. The displacement histories of both materials are presented in Figure 4.13. The mean midpoint displacements are presented in Table 4.7.

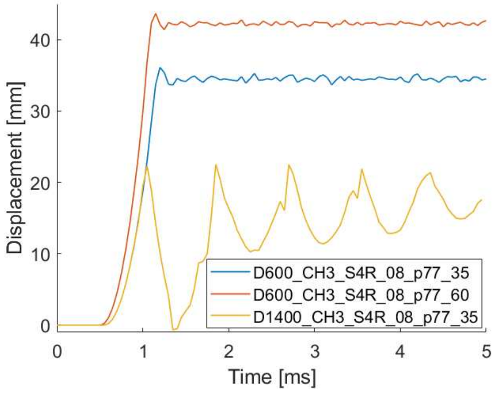

Figure 4.13: Displacement history of the midpoint for Docol 600DL at 35 and 60 bar, and Docol 1400M at 35 bar.

Table 4.7: Mean midpoint displacement measured for the CH3 configuration using Docol 600DL and Docol 1400M.

Model name	**Mean displacement** [mm]	**Crack length** [mm]
D600_CH3_S4R_08_p77_35	33.93	No cracking
D600_CH3_S4R_08_p77_60	41.5	No cracking
D1400_CH3_S4R_08_p77_35	17.19	No cracking
D1400_CH3_S4R_08_p77_60	Failure	Failure

4.3.3 Resulting Test Matrix

A resulting test matrix was established based on the result of the simulations conducted for this preliminary study and is presented in Table 4.8. This test matrix contains a summary of the experienced response of the CHX configurations at different pressure levels for both materials. It is worth noticing that the CH3 configuration not is included for Docol 1400M as this configuration was not tested experimentally. This is due to the scarcity of available plates, and as holes closer to the center was deemed the most detrimental.

Table 4.8: Test matrix based on the simulations in the preliminary study.

Material	**Configuration**	**Firing Pressure** [bar]	**Estimated Response**
Docol 600DL	**CH1**	35	Mainly deformation
		60	Mainly deformation
Docol 600DL	**CH2**	35	Mainly deformation
		60	Mainly deformation
Docol 600DL	**CH3**	35	Mainly deformation
		60	Mainly deformation
Docol 1400M	**CH1**	25	Crack arrest
		35	Total failure
Docol 1400M	**CH2**	25	Mainly deformation
		35	Crack arrest

4.4 Concluding Remarks

There was observed negligible differences in displacements between element sizes for Docol 600DL, as well as non-significant oscillations. Further, the artificial strain ratio was observed to be well under the recommended value in Abaqus. The responses of the simulations were observed to be a good approximation of the experimental results of a full flexible plate, with 35 bar being the most accurate.

For Docol 1400M, the differences in displacements between the finest- and coarsest elements were significant, and it was observed that a decrease in pressure lead to an increase in these differences. It was further observed that the material exhibited significant oscillations, which increased with decreasing pressure as well. The oscillations were believed to be partly due to an elastic rebound of the material. These spurious oscillations consequently lead to the introduction of artificial strain energies about 15-20 times greater than for Docol 600DL. For the coarsest elements, some ratios were observed to be over the recommendation in Abaqus, and the validity of the model should thus be questioned. The numerical responses were observed to be stiffer than the experimental.

For both materials, it was observed that damage accumulated in the integration point decreased as the perfectly circular holes were moved outward from the center along the yield lines. For Docol 600DL it was observed a decrease of 58.3% at 35 bar and 48.1% at 60 bar in accumulated damage from the CH1- to the CH3 configuration. For Docol 1400M, the damage accumulated for the CH1 configuration was 740.3 at 25 bar, and 702 for the CH3 configuration at 35 bar. Consequently, it is safe to conclude that the most detrimental configuration is the CH1 configuration. This is a quite reasonable result as the maximum deflection of the plates occurs at the center, which in turn introduces an area of highly localized strains. When the center is discontinuous due to perforation, the plate loses its ability to transfer membrane forces across the center, which in turn result in loss of capacity and ultimately failure of the plate. It was observed that the blast-load capacity of the full Docol 600DL plate was 15.4% greater than that of Docol 1400M.

Chapter 5

Experimental Work

5.1 Introduction

In this chapter, the experimental work carried out for this thesis is presented. This chapter is divided into two main parts: impact- and blast loading. Both sections are presented in terms of experimental setup and results, and the documentation of these results. At the end of this chapter, the experimental results are discussed with respect to findings made and to the materials. This chapter aims to present the experimental data, as well as to establish the most significant differences between the two materials with respect to both impact- and blast loading. The results obtained in the following will serve as a basis of comparison for the final numerical study in Chapter 7, in order to validate the numerical models.

All experiments were conducted at the SIMLab facilities at the Department of Structural Engineering, at NTNU in Trondheim. The experiments were conducted on Docol 600DL and Docol 1400M steel plates with a nominal thickness of 0.8 mm and a nominal geometry depicted in Figure 5.1. The circular holes in the plates had a nominal diameter of 25 mm and were used to mount the plates to the clamping rig in the shock tube, giving a blast-exposed area of 300 mm x 300 mm. The different experimental configurations are depicted in Figure 5.2, showing the dimensions relative to the blast-exposed area.

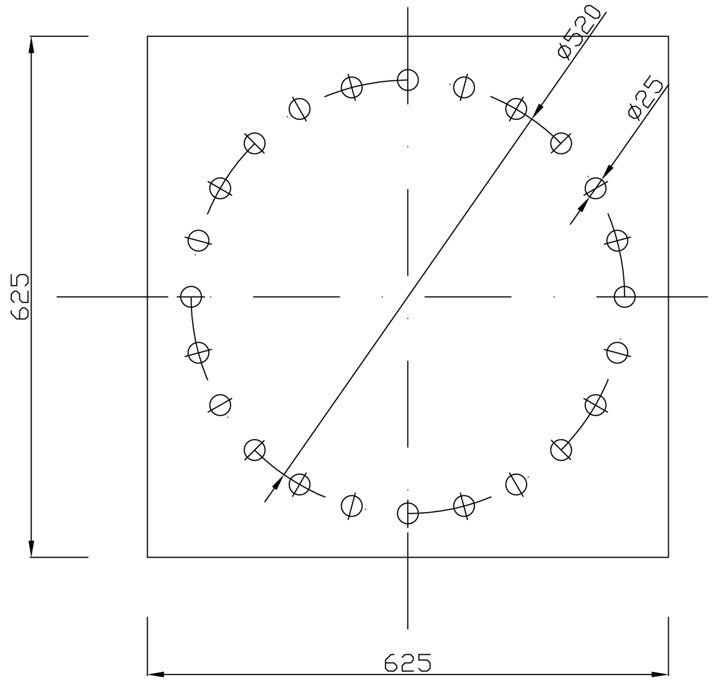

Figure 5.1: The nominal geometry of the undeformed plates used for the experiments in this thesis.

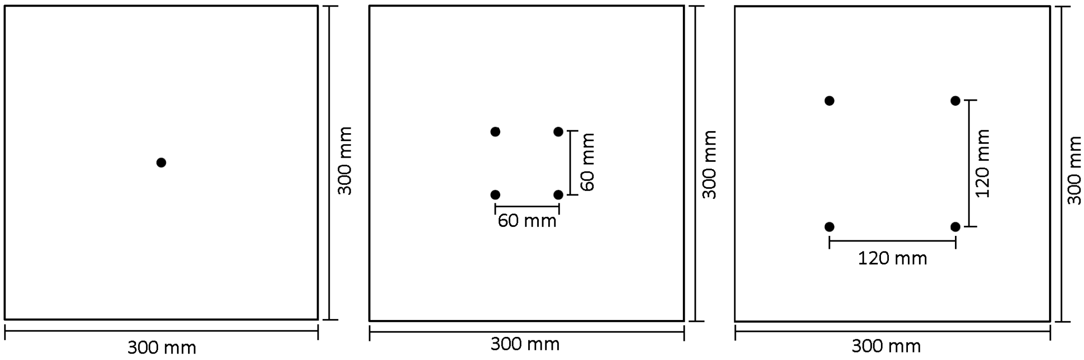

(a) BP1/B1 configuration. **(b)** BP2/B2 configuration. **(c)** BP3/B3 configuration.

Figure 5.2: Configurations used in the experimental work. The black dots denotes ballistic perforations, and are shown relative to the blast-exposed are in the shock tube.

5.2 Impact Loading

5.2.1 Experimental Setup

The ballistic impact experiments were conducted in a ballistics rig where 7.62 mm AMP2 (armor piercing) projectiles were fired at the targets from a smooth-bore Mauser. The projectiles weighed approximately 10.5 g and consisted of three parts: a lead tip, a hardened steel core and an outer casing made out of brass. The nominal geometry and composition of the projectile are depicted to the right in Figure 5.3. The firearm was mounted inside a protective tank and coupled to a remote trigger. The test setup is depicted as a schematic to the left in Figure 5.3. The rifle and the remote trigger are depicted in Figure 5.4a. The experiments were filmed using high-speed cameras of the type Phantom v1610, which was used to calibrate the initial- and residual velocities of the projectiles. The Phantom high-speed cameras used to document the experiments are depicted in Figure 5.4b.

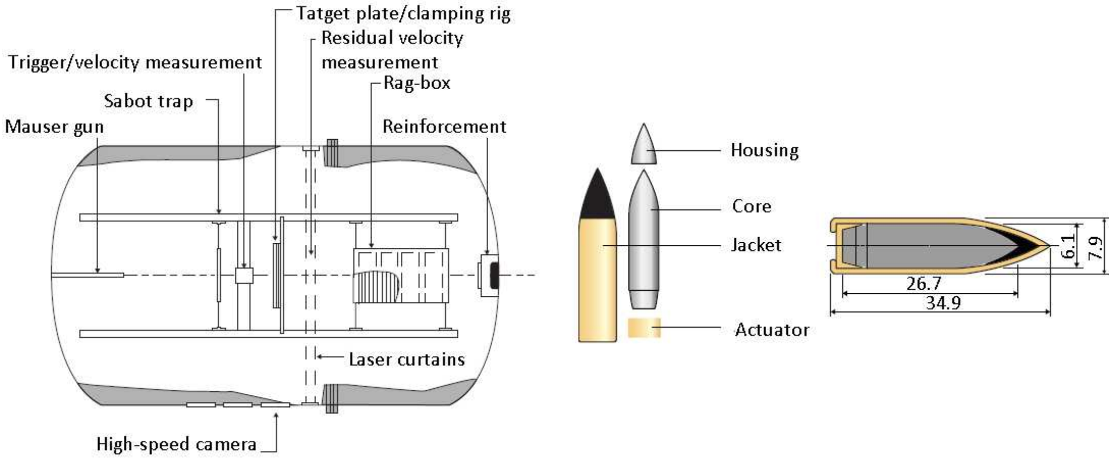

Figure 5.3: Schematic of the setup for ballistic experiments (left), and geometry and composition of 7.62 mm APM2 (right). Measurements are in [mm]. Taken from [80].

The ballistic experiments were conducted on target plates oriented orthogonal to the velocity vector of the projectile (i.e., normal impact) for all Docol 1400M plates, and the majority of the Docol 600DL plates. The orthogonal setup of the target plates is depicted in Figure 5.5a. In addition, some of the Docol 600DL plates were tilted at a 45° angle relative to the velocity vector.

To manage this, a wooden rig was constructed and fixed to the clamping rig. The wooden rig-setup is depicted in Figure 5.5b. By adding the rig, the camera had to be moved in order to track the perforation of the projectiles. Unfortunately, the view of the camera was obscured by a window frame of the ballistics tank. The solution was to use two cameras: one tracking the entry of the projectile, and the other capturing the exit.

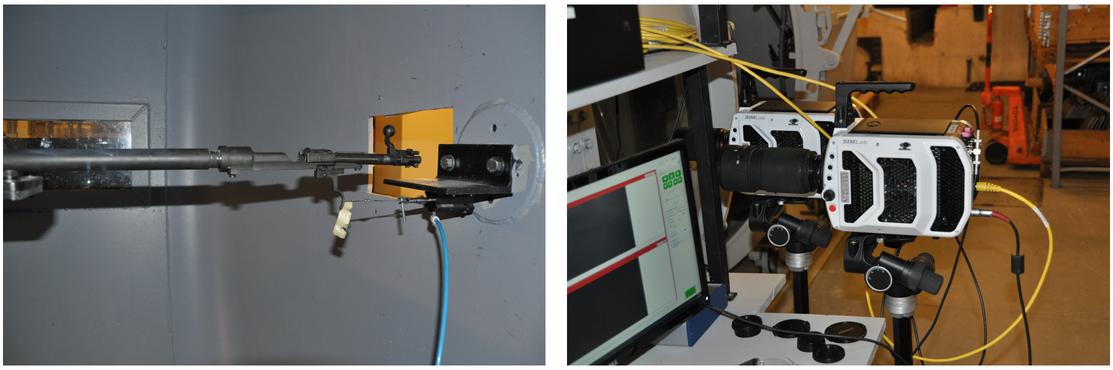
(a) (b)

Figure 5.4: (5.4a) Depicts the remote trigger attached to the smooth bore Mauser, and (5.4b) depicts the two Phantom high-speed cameras used for logging the experiments.


(a) (b)

Figure 5.5: The two plate setups. (5.5a) Shows the orthogonal setup, and (5.5b) shows the setup which is tilted at an 45° angle.

For the ballistic experiments, a total of three configurations were carried out. These are presented in short below. It should be noted that "BP" denotes *ballistic perforation.*

- **BP1 Configuration**: A single projectile was fired at the center (relative to the blast-exposed area in the shock tube) of the target. Projectiles were fired normal at targets for both Docol 600DL and 1400M, as well as plates that were tilted at an angle of 45° for Docol 600DL. This configuration is depicted in Figure 5.2a.
- **BP2 Configuration**: Four projectiles were fired at the target with a distance of 60 mm between each adjacent projectile, forming a square with dimensions 60 mm x 60 mm between the perforations. The projectiles were only fired normal at the plates. This configuration is depicted in Figure 5.2b.
- **BP3 Configuration**: Four projectiles were fired at the target with a distance of 120 mm between each adjacent projectile, forming a square with dimensions 120 mm x 120 mm between the perforations. The projectiles were only fired at Docol 600DL plates. Projectiles were fired normal at targets and plates that were tilted at an angle of 45°. This configuration is depicted in Figure 5.2c.

5.2.2 Experimental Results

The results presented are the initial- and residual velocities of the projectiles for all successfully conducted experiments, and images depicting the perforation event and the resulting perforations for a selection of the experiments.

The initial- and residual velocities of the projectiles denoted v_i and v_r, respectively, were measured by utilizing pictures from the high-speed cameras and the built-in camera software. These results are presented in Table 5.1 and 5.2 for Docol 600DL and Docol 1400M, respectively, and are sorted after configuration and impact angle. Included in the tables are also the calculated difference (in %) between the initial- and residual velocity. It can be observed that the initial velocities of all experiments are close to equal and that the difference in these velocities lies in the approximate range 1%-2%. The maximum difference was observed to be 1.99% for experiment D1400_BP2_7. It is further observed no difference in loss of initial velocity for the tilted- and orthogonal targets.

Table 5.1: Tabulated results from ballistic impact experiments on the Docol 600DL plates. "BP" denotes *ballistic perforation*. The results are sorted after plate configuration, impact angle and test number. *Difference* states the calculated difference (in %) between the initial- and residual velocity.

Configuration	**Angle**	**Test**	v_i [m/s]	v_r [m/s]	**Difference** [%]
BP1	0	1	923.1	909.7	1.45
	0	2	923.1	912.3	1.17
BP1	45	1	909.6	898.9	1.18
	45	2	926.2	911.8	1.56
BP2	0	1	924.0	914.2	1.06
	0	2	914.2	904.4	1.07
	0	3	931.3	919.1	1.31
	0	4	909.3	899.6	1.07
	0	5	932.2	917.4	1.59
	0	6	933.8	921.3	1.34
	0	7	918.5	906.0	1.36
	0	8	928.9	916.9	1.29
BP3	0	1	921.7	907.2	1.57
	0	2	921.7	909.7	1.30
	0	3	903.1	889.7	1.48
	0	4	894.9	884.6	1.15
	0	5	934.0	924.2	1.05
	0	6	921.6	907.2	1.56
	0	7	915.5	902.2	1.45
	0	8	-	-	-
BP3	45	1	926.2	910.0	1.75
	45	2	921.3	904.7	1.80
	45	3	906.6	892.4	1.57
	45	4	920.6	904.0	1.80
	45	5	917.1	902.3	1.61
	45	6	916.4	903.0	1.46
	45	7	926.2	909.2	1.84
	45	8	908.2	892.4	1.74

Table 5.2: Tabulated results from ballistic impact experiments on the Docol 1400M plates. "BP" denotes *ballistic perforation.* The results are sorted after plate configuration and test number. *Difference* states the calculated difference (in %) between the initial- and residual velocity.

Configuration	**Angle**	**Test**	v_i [m/s]	v_r [m/s]	**Difference** [%]
BP1	0	1	917.7	907.5	1.11
	0	2	918.5	909.4	0.99
BP2	0	1	919.1	904.4	1.60
	0	2	926.8	915.2	1.25
	0	3	919.1	909.3	1.07
	0	4	931.4	921.3	1.08
	0	5	921.3	909.3	1.30
	0	6	935.0	919.6	1.65
	0	7	940.5	921.8	1.99
	0	8	939.7	924.0	1.67

The dominant failure mode for both of the materials was petaling, which is the expected primary failure mode for thin steel plates [23]. The formation of petals leads to cracking around the perforation for all experiments. Petaling occurs as the material in front of the projectile is stretched out by the impact, leaving a dent. The top of the dent finally ruptures as the projectile continues to stretch out the material. As it ruptures, the stress in the dent rapidly decreases as cracks radiate from the ruptured area, leaving petals. The petals are bent backward until they allow the projectile to pass through the formed perforation.

Due to similarities in the experiments, it consequently follows that there exists little to no variation in the resulting perforations. The only differences are either yaw or pitch of the projectile before impact. Thus, only a handful of the entry- and exit perforations are presented. The resulting perforations are presented in Figure 5.6 and 5.7. In the figures "F" denotes *front* and is defined as the side of entry, and "B" denotes *back* and is defined as the opposing side. It is observed that all experiments experienced discoloration around the perforation, which was due to heat caused by friction between the plate and projectile. It is further observed that Docol 1400M experienced more prominent cracking at the base of the petal, which can be linked to Docol 1400M being a less ductile and harder material.

For the projectiles impacting at an oblique angle, petaling still is the dominant failure mode, but with some altercations. The same process as for normal petaling applies, but the material is pushed out at a different angle, causing the material to elongate more before rupturing. On the side where the projectile strikes the plate, petals are observed to form around the lower bound of the projectile with less cracking and less defined petals. These petals extend to the opposing side, causing fringes around the lower half of the perforation. The top half is seen to be more smooth with the resemblance of an "eyelid", with no observable cracking through the "eyelid" itself. This is depicted in Figure 5.6.

The majority of the experiments were observed to have no pitch or yaw prior to impact. Consequently, the perforation processes were quite similar, and therefore not depicted for all experiments. Figure 5.8 depicts a time-lapse of the penetration for projectiles experiencing no yaw or pitch. By observation of the projectiles after impact, it is seen that blackened finish of the brass tip gets more stripped for Docol 1400M, which probably is linked to it being a harder material. The time-lapse of projectiles experiencing pitch are depicted in Figure 5.9. Here, the experiments with the most pitch for each material have been included. From the figures, it is observed that a part of the plate gets peeled off as the projectile passes through the material. This consequently affects the resulting perforation and can be seen in Figure 5.7d and 5.7e for Docol 600DL, and in Figure 5.7f for Docol 1400M.

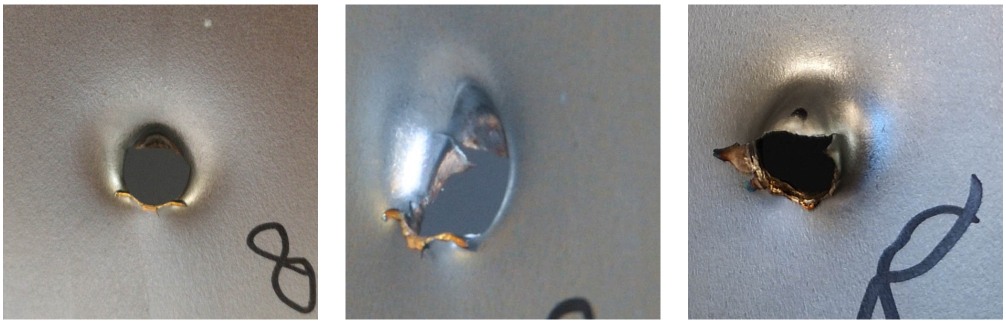

(a) D600_BP3_45_8_F **(b)** D600_BP3_45_8_F **(c)** D600_BP3_45_8_B

Figure 5.6: A selection of entry- and exit holes from the conducted experiments, taken at different angles. Here, "F" denotes *front* and is defined as the side of entry, and "B" denotes *back* and is defined as the opposing side.

(a) D600_BP3_0_4_F **(b)** D600_BP3_0_4_B **(c)** D600_BP3_0_4_B

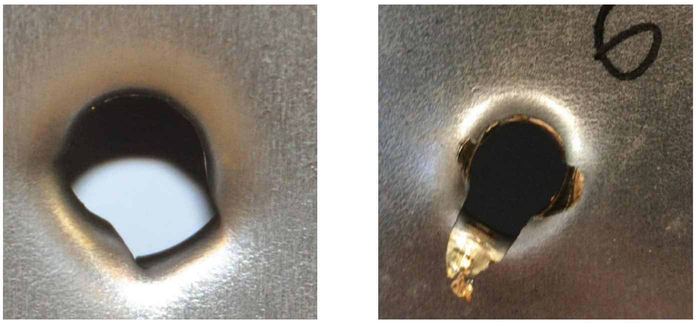

(d) D600_BP3_0_6_F **(e)** D600_BP3_0_6_B

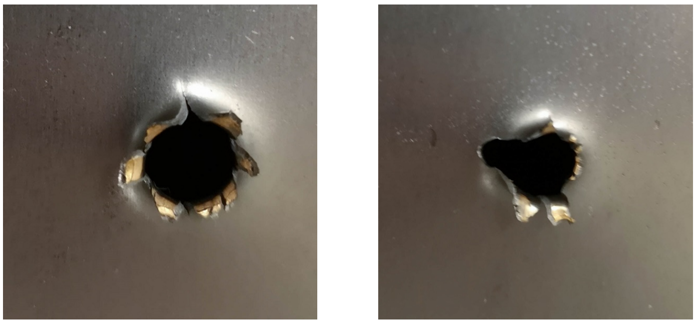

(f) D1400_BP2_0_1_B **(g)** D1400_BP2_0_2_B

Figure 5.7: A selection of entry- and exit holes from the conducted experiments, taken at different angles. Here, "F" denotes *front* and is defined as the side of entry, and "B" denotes *back* and is defined as the opposing side.

(a) D600_0_BP1_1 **(b)** D600_0_BP1_2

Figure 5.8: Time-lapse of the high-speed video showing the perforation of a (5.8a) Docol 600DL and (5.8b) Docol 1400M plate that experienced normal impact, with no initial yaw or pitch.

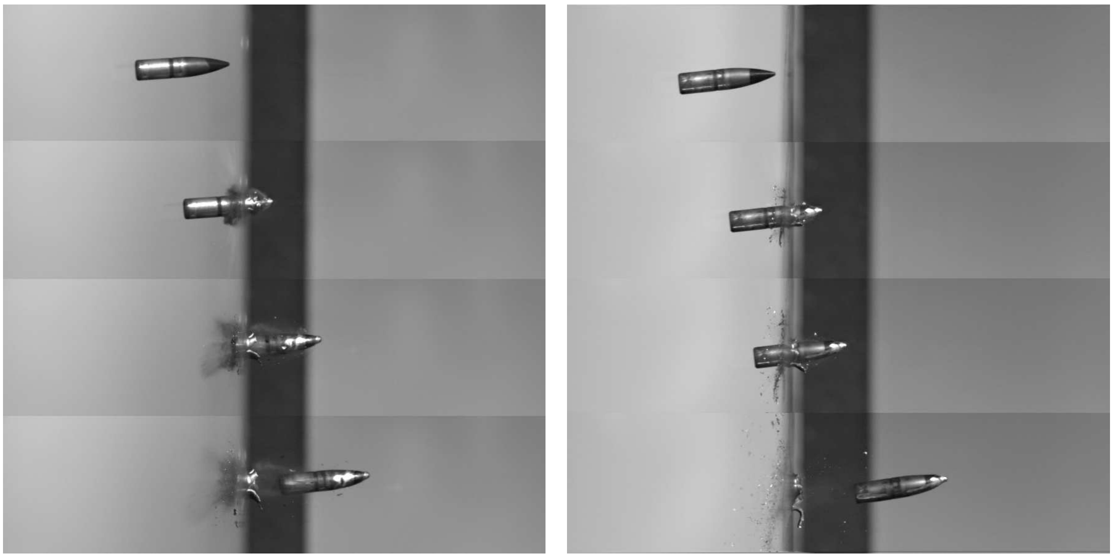

(a) D600_0_BP3_6 **(b)** D1400_0_BP2_1

Figure 5.9: Time-lapse of the high-speed video showing the perforation of a (5.9a) Docol 600DL and (5.9b) Docol 1400M plate that experienced normal impact. Both projectiles had a pitch prior to impact.

In addition, experiments were conducted with oblique impact for both the BP1- and BP3 configuration using Docol 600DL. A time-lapse of this is presented in Figure 5.10. From the figure, it is observed that the tip of the projectile gets broken off as it impacts the plate.

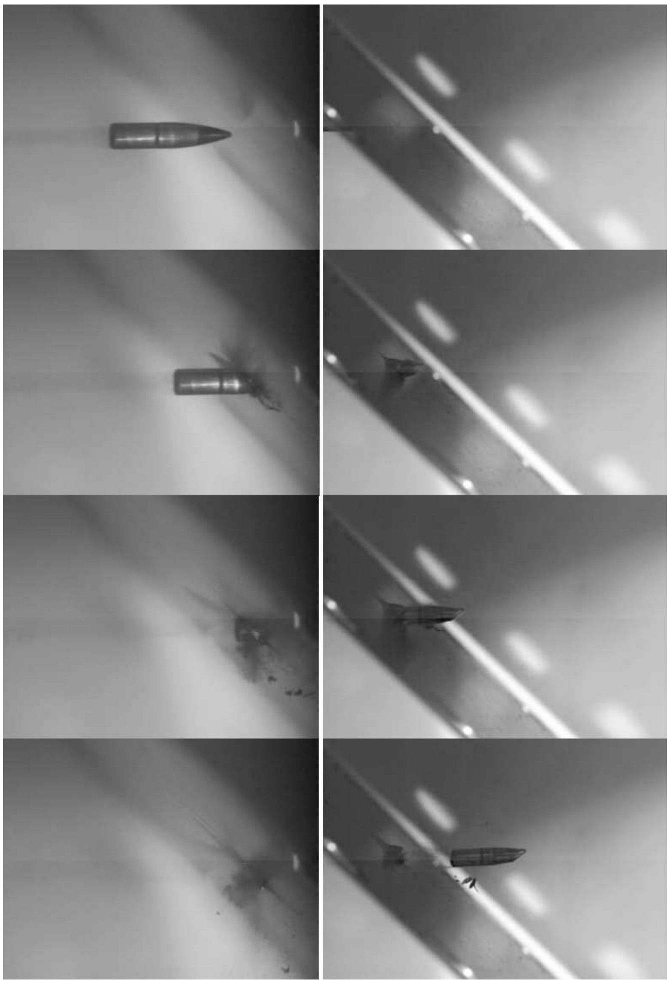

Figure 5.10: Time-lapse of the high-speed video showing the perforation of experiment D600_45_BP1_1, tilted 45° relative to the velocity vector.

5.3 Blast Loading

5.3.1 Experimental Setup

The SIMLab Shock Tube Facility

The blast loading experiments were conducted at the SIMLab shock tube facility (SSTF) at NTNU. The SSTF complies with the requirements of a shock tube given in the Eurocode [37]. An illustration of the shock tube is depicted in Figure 5.11. For the results to be valid from this facility, it needs to be thoroughly tested and validated. This validation has been done in detail by Aune *et al.* (2016) [37], and the SSTF has been thoroughly described as well. The reader is therefore further referred to [37], [31] for a more detailed presentation of the calibration process and the SSTF itself. The SSTF can be divided into four main sections. These sections are the *driver section*, *firing section*, *driven section* and *tank*. Each section is introduced briefly for completeness.

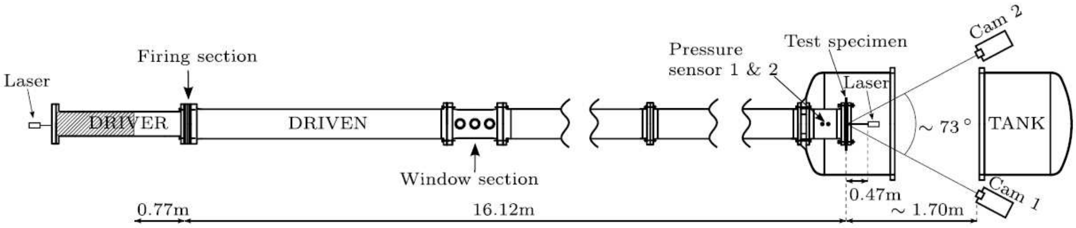

Figure 5.11: Illustration of the dimensions and different sectors of the SSTF. The figure is taken from [37].

Driver Section

A high-pressure chamber which has been pressurized by an air-compressor before the release of a shock wave. The total length of this section is 2.02 m but can be varied in accordance with what pressure level that is desirable. In all blast loading test conducted in this thesis, a driver length of 0.77 m was used. The shock tube, as seen from the end of the driver section, is depicted in Figure 5.12.

Figure 5.12: Picture of the shock tube, seen from the driver section. The picture is taken from [37].

Firing Section

Serves as a divider between the driver and the driven, which holds ambient pressure. In order to get a pressure build-up in the driver section, a step-wise transition between the high-pressure and low-pressure is needed. The pressure build-up is done by the use of three different layers of membranes which are placed in the firing section. This setup gives two intermediate pressure chambers between the highly pressurized driver section and the driven section. To obtain different firing pressures, the rupture strength of the membranes is varied by adding or removing membranes.

Driven section

It is located between the firing section and the tank. This section differs from the previous section as the cross-section is square with a dimension of 300 mm x 300 mm, and not circular. The reason for this is to obtain a shock wave which is uniformly distributed to the target plate, situated at the end of the driven section. The first 0.6 m of the driven section is used as a transition area between the two different cross-sections. Several pressure-sensors sample the pressure throughout the driver section. The two sensors closest to the plate are located at a distance of 24.5 cm (Sensor 2) and 34.5 cm (Sensor 1) upstream of the plate, making it possible to calculate the velocity of the shock wave before impacting the plate.

Tank

Situated at the end of the driven, and are where the blast-exposed plates are mounted. Serves as a protection against fragments and other particles that may originate from the blast loading experiments. The tank has two windows installed which allow two high-speed cameras to capture the experiment. The tank, as well as the two Phantom v1610 high-speed cameras used for these experiments, are depicted in Figure 5.13. The high-speed cameras capture images at the same rate as pressure data is extracted from the pressure sensor. Thus, the pressure data is linked to corresponding images. This synchronization makes it possible to define a common time-axis for all experiments, making comparisons more trivial.

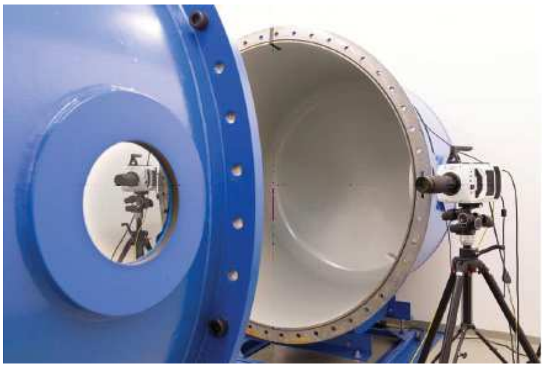

Figure 5.13: Picture of the tank and the two high-speed cameras. The picture is taken from [37].

Plate Setup

The plates were mounted by inserting it onto a set of bolts in the clamping rig and then by adding a metal frame, which was fastened using the bolts. The bolts used in the SSTF were 12 M24 bolts which were evenly distributed over the frame.

In order to post-process the high-speed footage with 3D-DIC, a random speckle pattern needs to sprayed onto the plates before conducting an experiment. The pattern was sprayed onto the plates manually by the use of spray cans and a stencil, in the colors black and white. A mounted plate with the speckle pattern is depicted in Figure 5.14.

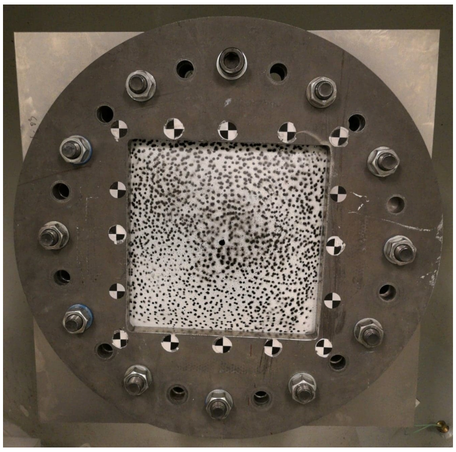

Figure 5.14: Plate of configuration B1 mounted in the clamping frame with the random speckle pattern.

Three-Dimensional Digital Image Correlation

Three-dimensional digital image correlation (3D-DIC) is a non-intrusive optical technique used to measure, inter alia, displacements, and strains by the use of high-speed cameras. The setup of the cameras are depicted at the far right in Figure 5.11 and in Figure 5.13. To measure the displacements, a random speckle pattern must be applied to the plates, which is continuously tracked by the two cameras through the experiment. The 3D-DIC analyses conducted in this thesis were run using the NTNU-developed software eCorr. The reader is further referred to [81] for further reading and documentation on the eCorr-software.

The two cameras are calibrated using a set of images which are taken of a calibration target with know geometry. This gives the coordinates of the target, which is utilized in further 3D-DIC analyses. For this thesis, the calibration target was a cylinder with a diameter of 80 mm, which is depicted in Figure 5.15a. A given tracked point, which is related to the uniqueness of the speck pattern, is captured by the two cameras. This gives the point coordinates for each of the cameras. These separate coordinates are then translated into spatial coordinates by taking the angle of the cameras into account. To get data from the DIC-analysis, an image of the undeformed plate for each of the cameras must be meshed. The meshing is done by applying a Q4 mesh to both images such that the resulting mesh grid coincides with the same points of the speckle pattern for both images. The analysis will then apply the two separate meshes to the same points during the deformation, which is done by using the grey scale values of the images.

The Q4 mesh of one of the undeformed plates is depicted in Figure 5.15b. As the rig itself will have some movement during the blast experiments, the acquired results may get somewhat overestimated. The solution for this is to track the checkerboard stickers on the rig, and then subtract the displacements of the rig itself from the displacement curves.

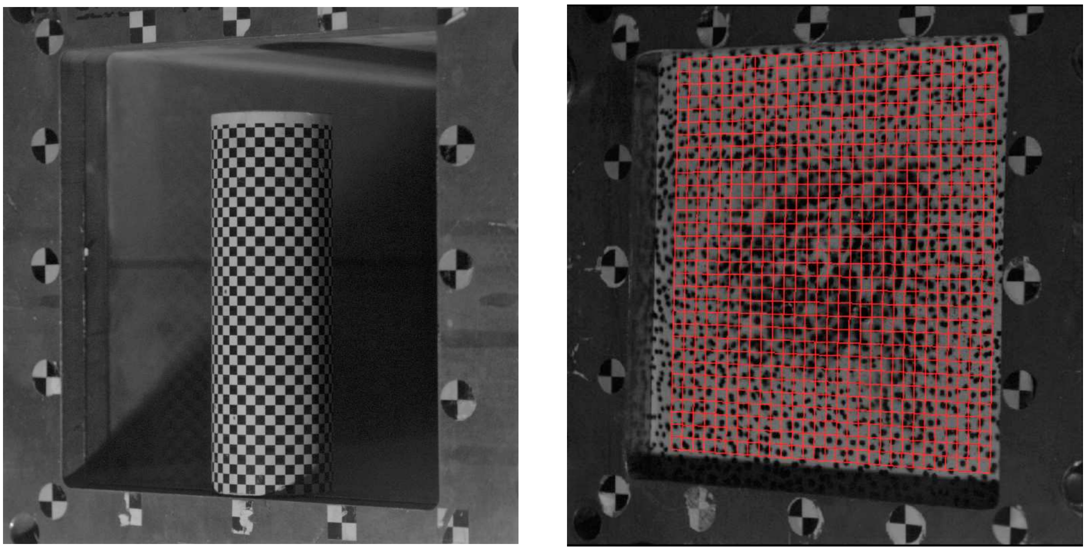

(a) (b)

Figure 5.15: (5.15a) Shows the cylindrical calibration target, and (5.15b) shows the Q4 mesh generated in eCorr for one of the plate configurations.

Laser Scanning

The blast-deformed plates were measured using a laser scanner while the plates were still mounted in the shock tube. The laser scanning was done using a portable laser scanner of the type ROMER Absolute Arm 7525SI delivered by Hexagon Manufacturing Intelligence. The scanning was done by scanning the surface of the plate from different angles. This allowed the scanning-device to accurately capture the surface and possible cracking of the deformed plates, as several small points. For this particular device, the point repeatability is reported to be 0.02 mm, which is defined by measuring a point from several angles. The measured points were then discretized as a pointcloud, and given out a file that specifies the Cartesian coordinates of the scanned plate relative to a chosen origin. The reader is referred to [82] for more technical details and further reading on the ROMER Absolute Arm.

5.3.2 Experimental Results

The results presented in this section are, in order, post test images of all conducted experiments, pressure-time curves, midpoint (or reference point) displacements and displacement profiles obtained with 3D-DIC, the results obtained using laser scan will be presented and compared to the results obtained with 3D-DIC, and finally a presentation of the cracking of the plates.

The naming convention used for the experiments in this section is on the form **MMM_BX_AA_tt**. Here, *MMM* denotes the material (D600 or D1400), *B* denotes the configuration (same configuration as in the previous section: B1 corresponds to BP1, B2 to BP2 and B3 to BP3), *AA* is the angle of projectile impact and *tt* is the nominal firing pressure [bar]. Table 5.3 shows which ballistics experiments that corresponds to which blast loading configuration.

Table 5.3: Table showing which ballistics experiments that have been conducted on the blast loaded plates. "B" denotes *blast*, and as before "BP" denotes *ballistic perforation.*

Material	Blast Configuration	Angle	Firing Pressure	Ballistics Experiment
Docol 600DL	**B1**	0	25	BP1_1
		0	35	BP1_2
		45	35	BP1_45_1
		45	60	BP1_45_2
Docol 600DL	**B2**	0	25	BP2_1, 2, 3, 4
		0	35	BP2_5, 6, 7, 8
Docol 600DL	**B3**	0	25	BP3_1, 2, 3, 4
		0	35	BP3_5, 6, 7, 8
		45	35	BP3_45_1, 2, 3, 4
		45	60	BP3_45_5, 6, 7, 8
Docol 1400M	**B1**	0	25	BP1_1
		0	35	BP1_2
Docol 1400M	**B2**	0	25	BP2_1, 2, 3, 4
		0	35	BP2_5, 6, 7, 8

At the end of Chapter 4, a test matrix was established based on the results of the preliminary study. The test matrix of the blast loading experiments is presented in Table 5.4. Here, "B" denotes *blast*. As can be observed from the table below, the two test matrices differs some, which is quite reasonable as cracking around the petals were observed to lead the propagating cracks.

Table 5.4: The experimental test matrix for all conducted blast loading experiments. It is worth noticing that the angle denotes the angle at which the projectiles perforated the plates. "B" denotes *Blast*.

Material	**Configuration**	**Angle**	**Firing Pressure** [bar]	**Response**
Docol 600DL	**B1**	0	25	Mainly deformation
		0	35	Crack initiation
		45	35	Mainly deformation
		45	60	Crack initiation
Docol 600DL	**B2**	0	25	Mainly deformation
		0	35	Mainly deformation
Docol 600DL	**B3**	0	25	Mainly deformation
		0	35	Mainly deformation
		45	35	Mainly deformation
		45	60	Mainly deformation
Docol 1400M	**B1**	0	25	Crack arrest
		0	35	Total failure
Docol 1400M	**B2**	0	25	Crack arrest
		0	35	Total failure

Post-Test Images

In the following, the post-test images of all conducted experiments are presented. The post-test images are depicted in Figure 5.16 for Docol 600DL and in Figure 5.17 for Docol 1400M. The images are sorted by configuration and nominal firing pressure. From the images, it is seen that Docol 1400M is the only material experiencing crack arrest to such a large extent, as well as total failure. Some of the experiments conducted on the Docol 600DL steel plates have been observed to exhibit crack initiation as well. This is further presented and discussed in Section 5.3.3.

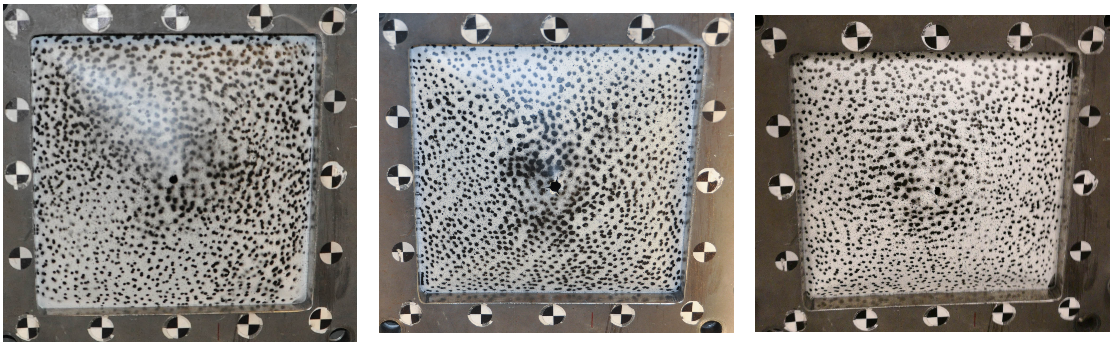

(a) D600_B1_0_25 **(b)** D600_B1_0_35 **(c)** D600_B1_45_35

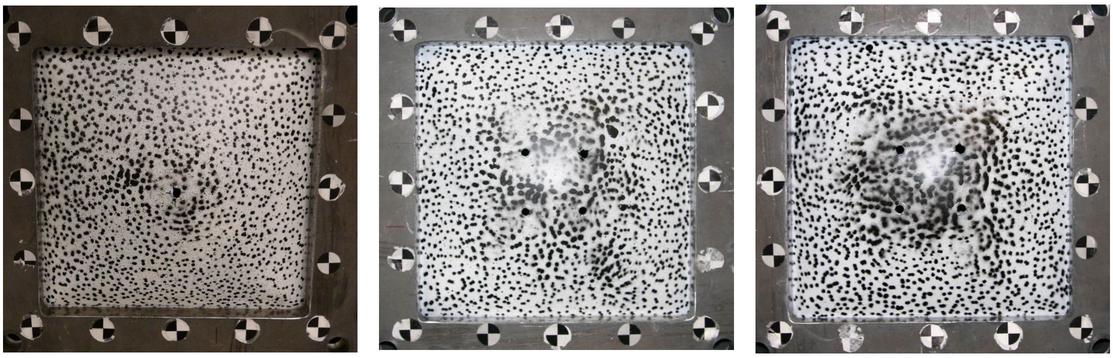

(d) D600_B1_45_60 **(e)** D600_B2_0_25 **(f)** D600_B2_0_35

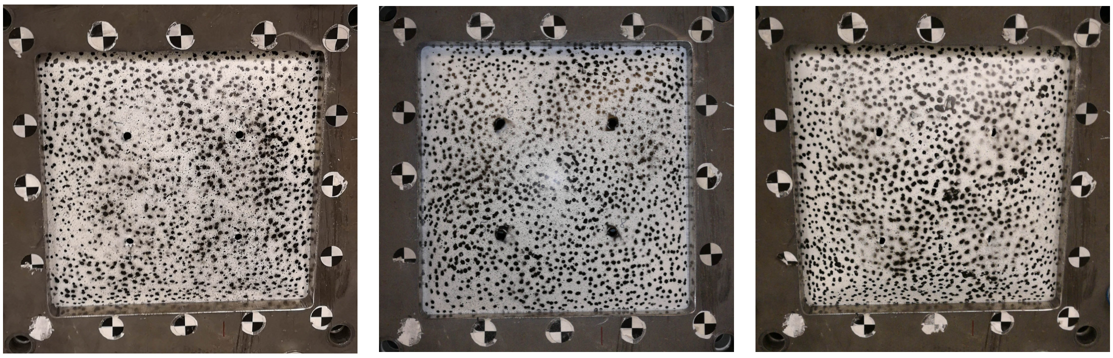

(g) D600_B3_0_25 **(h)** D600_B3_0_35 **(i)** D600_B3_45_35

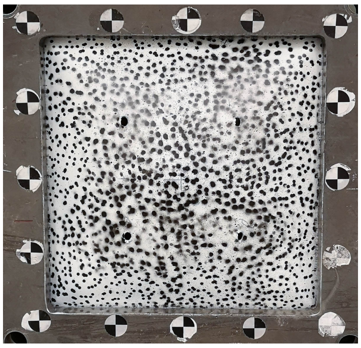

(j) D600_B3_45_60

Figure 5.16: Post-test images of all conducted blast loading experiments using Docol 600DL.

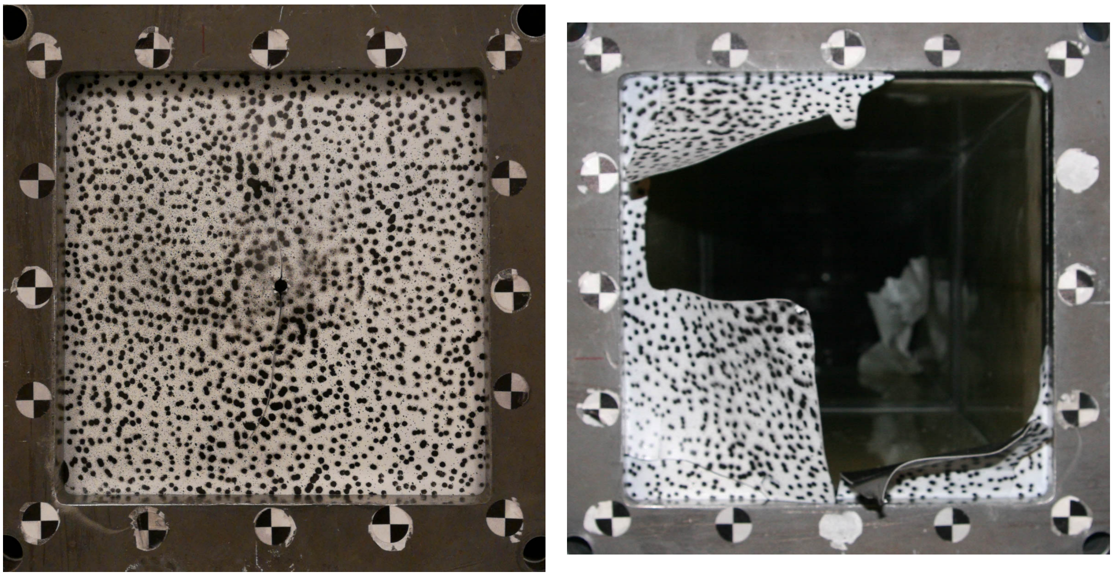

(a) D1400_B1_0_25

(b) D1400_B1_0_35

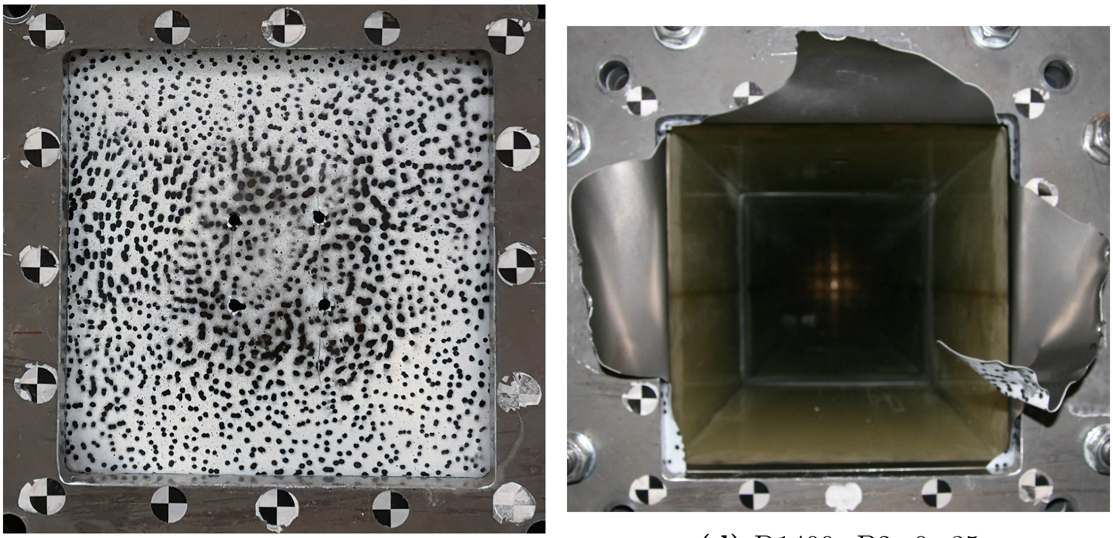

(c) D1400_B2_0_25

(d) D1400_B2_0_35

Figure 5.17: Post-test images of all conducted blast loading experiments using Docol 1400M.

Pressure-Time Data

The nominal- and the measured firing pressures for all conducted experiments are given in Table 5.5. The column *Deviation* is given as the deviation between the measured- and nominal firing pressure (in %). From the table below it is observed that the maximum difference is 8.33%. It is further observed that a nominal firing pressure of 35 bar yielded the highest deviations.

Table 5.5: Nominal- and measured firing pressures for Docol 600DL and 1400M. *Deviation* is given as the deviation between the measured- and nominal firing pressure (in %).

Material	**Configuration**	**Angle**	**Nominal Firing Pressure** [bar]	**Measured Firing Pressure** [bar]	**Deviation** [%]
D600	**B1**	0	25	25.11	0.44
		0	35	38.16	8.28
		45	35	38.18	8.33
		45	60	62.12	3.41
D600	**B2**	0	25	25.14	0.56
		0	35	38.15	8.26
D600	**B3**	0	25	25.15	0.60
		0	35	38.17	8.30
		45	35	37.99	7.87
		45	60	62.10	3.38
D1400	**B1**	0	25	25.11	0.44
		0	35	38.17	8.30
D1400	**B2**	0	25	25.07	0.28
		0	35	38.14	8.23

Pressure-time curves for all successfully conducted experiments are presented in Figure 5.18. The experimental curves have been plotted against the pressure-time histories obtained for solid steel plates [37], which were plotted in black and marked with "*Cal*". The experimental pressure histories were taken from the pressure-sensor closest to the plate (Sensor 2), situated 24.5 cm upstream from the plate. The pressure histories presented are defined as the gauge pressure, i.e., the amount of pressure that exceeds atmospheric pressure.

It is worth noticing that all curves have been shifted such that the incoming pressure passes Sensor 2 at a time equal to zero, which can be seen as the first sudden peak in pressure. As the displacement-data are coupled and synchronized with the pressure-data, this results in an equal shifting of the displacements as well. Doing this gave all the experiments the same reference frame, and it was thus more trivial to present and compare results. To better visualize the data, a moving mean algorithm was utilized, which removed sudden peaks in the datasets and smoothed the curves to a certain degree [83].

From observing Figure 5.18b it is readily seen that the pressure for experiment D1400_B2_0_35 drastically drops after reaching the peak reflected pressure. The pressure drop was due to a complete failure of the plate, which allowed the air to be released into the tank rapidly. From Figure 5.18 it can be seen that there exist negligible differences between the B1- and B3- configuration using Docol 600DL, which in turn differ from the B2 configuration. A possible explanation could be that the B2 configuration allowed more air to pass through as the perforations were placed in close vicinity of the center of the plate. This is not the case for Docol 1400M, where the curves of the B1- and B2 configuration are observed to coincide, which probably was due to extensive crack growth and crack arrest of the two plates. In addition, the effect of impact angle can be considered as insignificant, as there exists little deviation between normal- and oblique impact at 35 bar. From Figure 5.18c, the difference between the two curves may suggest that an increase in pressure leads to more significant deviations between the different configurations and different impact angles. In addition, it is observed that the experimental data differs somewhat from the calibration data, which is due to the fluid-structure interaction (FSI) effects [37], [8]. The FSI effects may be due to the deformations of the plates, and the movement and shape of the boundaries [37].

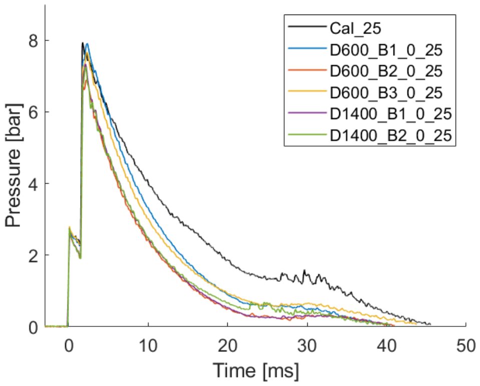

(a) 25 bar.

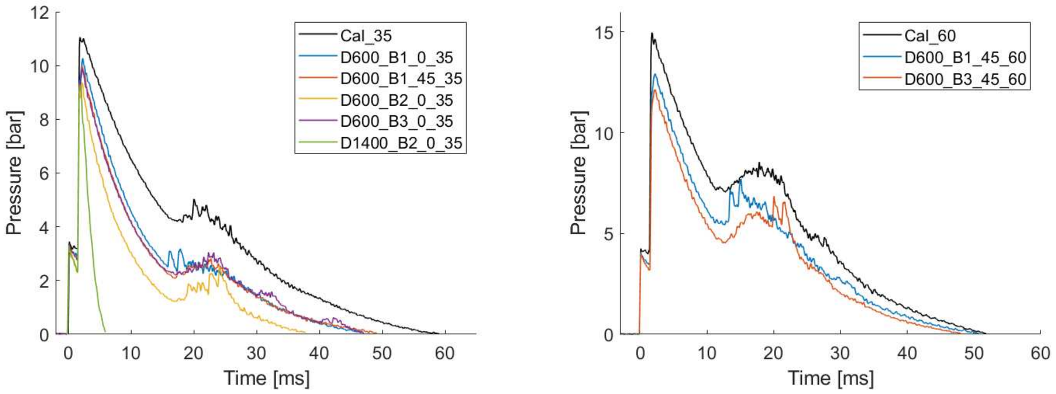

(b) 35 bar. **(c)** 60 bar.

Figure 5.18: Reflected pressures measured at the pressure sensor (Sensor 2) located 24.5 cm upstream from the mounted plates in the SSTF. (5.18a) Shows the pressure histories at 25 bar, (5.18b) at 35 bar and (5.18c) at 60 bar.

A comparison of the peak reflected pressures, as well as the positive time duration, is presented in Table 5.6. Here, the experiments have been grouped after nominal firing pressure and sorted after peak reflected pressure. The columns *Pressure Deviation* are defined as the deviation in peak reflected pressure from the calibrations, measured in both bar and %. From the table below it is observed that the deviation in measured peak reflected pressure increases as the nominal firing pressure increases, which possibly may explain the increasing differences of the curves at 60 bar.

Table 5.6: Measured peak reflected pressure and positive time duration for all successfully conducted experiments. The data was obtained from the closest sensor to the mounted plates. Listed deviations are given relative to the calibration experiments using massive steel plates.

Experiment	**Peak Reflected Pressure** [kPa]	**Positive Duration** [ms]	**Pressure Deviation** [kPa]	**Pressure Deviation** [%]
Cal_25	793.54	45.54	-	-
D600_B1_0_25	790.67	40.47	-2.87	0.36
D600_B3_0_25	766.34	43.75	-27.20	3.42
D1400_B1_0_25	739.80	39.62	-53.74	6.77
D1400_B2_0_25	725.28	40.25	-68.12	8.58
D600_B2_0_25	688.94	41.01	-140.6	17.72
Cal_35	1105.91	59.01	-	-
D600_B1_0_35	1026.81	47.02	-79.91	7.23
D600_B1_45_35	996.00	49.17	-109.91	9.94
D600_B3_0_35	987.47	46.92	-118.44	10.71
D1400_B2_0_35	936.57	49.17	-169.34	15.31
Cal_60	1496.76	51.80	-	-
D600_B1_45_60	1293.14	50.76	-203.62	13.60
D600_B3_45_60	1215.09	48.02	-281.67	18.82

The velocity of the shock wave u_s can be calculated by considering the time it takes for the shock wave to propagate from Sensor 1 to Sensor 2. The distance between these two sensors was 10 cm, and the wave velocity was assumed to be constant while propagating this distance. The shock Mach number, as recalled, is the ratio of the speed of an object moving through a fluid, and is given by

$$M_s = \frac{u_s}{c_a}$$

where c_a is the speed of sound in the non-shocked medium, which for air at room temperature is equal to 342.2 m/s. The shock wave velocities and the Mach number for the different experiments are given in Table 5.7. Here, it is observed that an increase in nominal firing pressure leads to an increase in shock wave velocity, and consequently, in the Mach Mach number. This can be validated by the Rankine-Hugoniot relations [33],[34],[35],[36] which were briefly presented in Section 2.3.1. This was also observed in the doctoral thesis of Aune (2017) [31].

Table 5.7: The shock wave velocity and calculated Mach number for all successfully conducted experiments.

Experiment	Velocity [m/s]	Mach Number
D600_B1_0_25	609.76	1.78
D600_B3_0_25	602.41	1.76
D1400_B1_0_25	602.41	1.76
D1400_B2_0_25	602.41	1.76
D600_B2_0_25	609.76	1.78
D600_B1_0_35	649.35	1.90
D600_B1_45_35	641.03	1.87
D600_B2_0_35	649.35	1.90
D1400_B2_0_35	649.35	1.90
D600_B1_45_60	694.44	2.03
D600_B3_45_60	684.93	2.00

Results Obtained with 3D-DIC

The results presented are midpoint displacements and deformation profiles, which are presented for all successfully conducted experiments that did not experience failure. For results obtained with 3D-DIC in the SSTF, it is worth noticing that results no longer are valid if the plexiglass in front of the cameras start to vibrate, as this makes the images from the high-speed cameras blurry. The 3D-DIC may then lose track of the previously defined gridpoints in the speckle pattern, which may result in inaccurate results with spurious oscillations. This occurs as air rapidly passes into the tank and was only observed for experiments experiencing failure.

For the B1 configuration, the mesh in the immediate vicinity of the perforation was deactivated such that the perforation did not induce mesh distortions as the plate deformed. As a consequence of this, neither the reference point nor the vector defining the cross-section were defined at the center of the plate but were selected below the deactivated section of mesh. This is depicted in Figure 5.19a, where the reference point has been visualized with yellow, and the vector in blue. From this, it consequently follows that the displacement histories may be somewhat inaccurate.

For experiments experiencing cracking, the mesh was distorted due to the propagating cracks. Consequently, a coarser mesh was applied, which allowed for crack initiation and growth without excessively distorting the mesh. It is worth noticing that this mesh had fewer nodes, which subsequently lead to less smooth deformation profiles.

As the 3D-DIC analyses were conducted manually, it is worth noticing that there exist some uncertainties. Some factors contributing to potential errors are presented briefly. The mesh was applied to the undeformed plate configuration for both cameras, where a point on the mesh must correspond to the same point for both views. Failing to do so may induce inaccurate responses. Further, the movement of the rig must be subtracted from the overall response. This was done by creating subsets which were tracked throughout the analysis. The subsets are depicted as green squares in Figure 5.19a. In addition, the extraction of midpoint deflection and deformation profiles were done manually, which in turn may yield some uncertainties as well. The vector is ideally defined through the center of the plate and is depicted in Figure 5.19b.

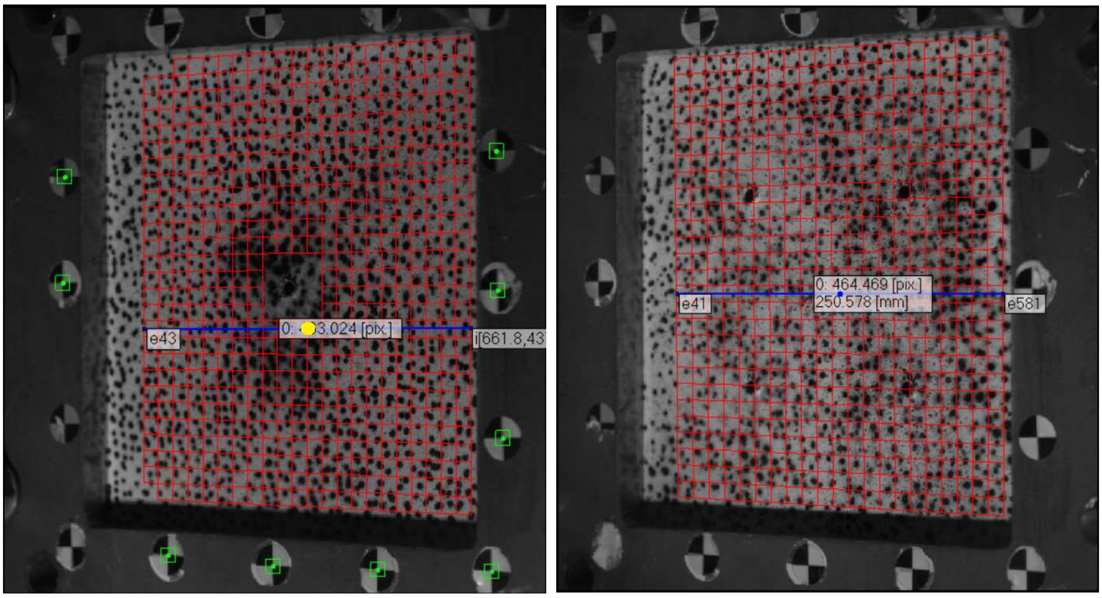

(a) D600_B1_0_25.

(b) D600_B3_0_25.

Figure 5.19: Meshing of two different experiments in eCorr. (5.19a) Shows the deactivation of elements in the vicinity of the perforation where the reference point is indicated with yellow and (5.19b) shows the vector used for sampling deformation profiles.

Midpoint Displacement

The time-displacement curves for all successfully conducted experiments are depicted in Figure 5.20 and 5.21. The displacement- and the pressure-data are synchronized and have been shifted to define a time equal to zero as the incoming pressure wave passes Sensor 2. From the observation of the figures below, it is observed that configurations experiencing the same nominal firing pressure exhibits the same initial response. Consequently, all results were grouped after nominal firing pressure, which is presented in Figure 5.22. As there only was one successfully conducted experiment at 60 bar, this plot was omitted.

From Figure 5.22, it is evident that the structural response is identical for all experiments. Namely, a sudden increase in displacements, followed by a phase of oscillations. By comparison, it is seen that Docol 1400M oscillates with a greater amplitude than Docol 600DL, where the oscillations are observed to be more insignificant. In addition, Docol 600DL is observed to deform more globally than Docol 1400M, which may be linked to Docol 1400M having higher strength, which yields a lesser extent of deformations of the plates. It can further be noticed that the B1- and B2 configurations yield a higher displacement than the B3 configuration for Docol 600DL. This can be explained by the fact that perforations closer to the center of the plates results in a lower structural stiffness. This consequently leads to a softer and more flexible response, which subsequently resulted in a reduction of capacity. The measured maximum displacements from Figure 5.22 are presented in Table 5.8 for all experiments presented in this section.

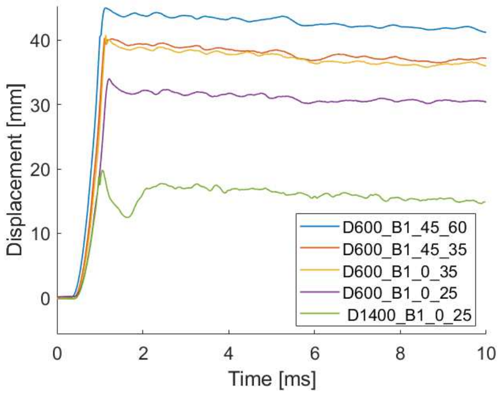

Figure 5.20: Time-displacement curves measured using 3D-DIC for configuration B1, for experiments not experiencing failure.

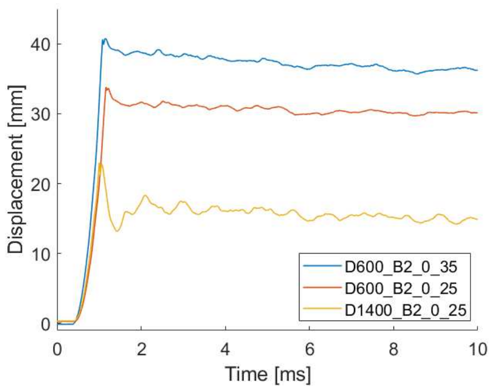

(a) B2 Configuration

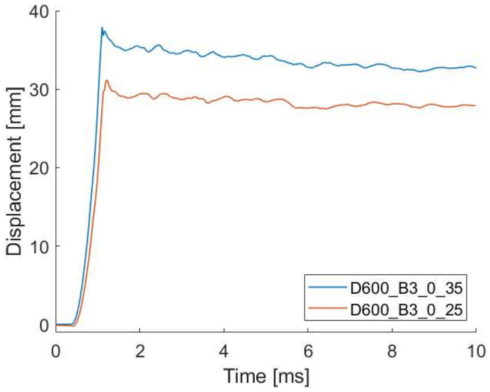

(b) B3 Configuration

Figure 5.21: Time-displacement curves measured using 3D-DIC for experiments not experiencing failure. (5.21a) Shows configuration B2 and (5.21b) shows B3.

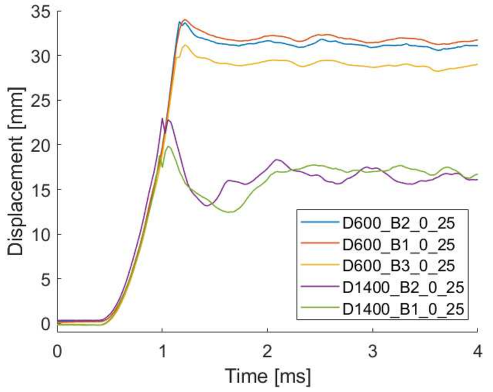

(a) 25 bar

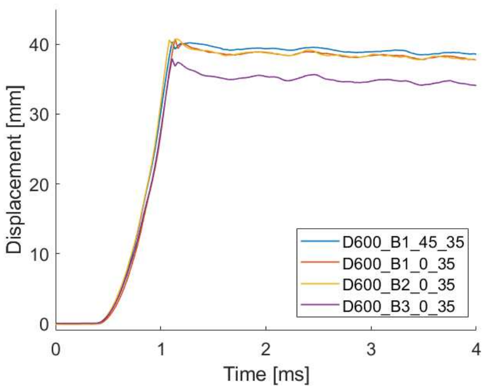

(b) 35 bar

Figure 5.22: Time-displacement curves for all successfully conducted experiments not experiencing failure. (5.22a) Shows the displacements at 25 bar and (5.22b) at 35 bar.

Table 5.8: Measured maximum deflection for all successfully conducted experiments not experiencing failure.

Material	Configuration	Angle	Firing Pressure [bar]	Maximum Deflection [mm]
Docol 600DL	**B1**	0	25	34.04
		0	35	40.80
		45	35	40.34
		45	60	45.02
Docol 600DL	**B2**	0	25	33.80
		0	35	40.73
Docol 600DL	**B3**	0	25	31.19
		0	35	37.94
Docol 1400M	**B1**	0	25	19.85
	B2	0	25	23.00

Deformation Profiles

The displacement profiles have been plotted at maximum displacement, and at 90%, 75%, 60% and 40% of maximum displacements. This was done to give an indication of how the materials deformed. The deformation profiles are presented in Figure 5.23 for 25 bar and in Figure 5.24 for 35 and 60 bar. The time of each profile extraction is specified in the figures. Here, it is seen that all deformation profiles are close to identical for the different firing pressures for each material. This corresponds well with previous observations, where displacements histories were observed only to deviate moderately. It is further observed that Docol 1400M have approximately the same shape in deformation profiles as Docol 600DL up until maximum deflection. This is again consistent with the displacement histories and with observations made in Section 4.3.1. From the observation of the high-speed footage from the Docol 1400M experiments, it was observed that the cracks propagate as the plates oscillate. This may be linked to Docol 1400M being a less ductile material. Also, that oscillations induced higher levels of plastic straining on the initiated cracks, which caused them to propagate further. Deformation profiles could be obtained for Docol 1400M after reaching maximum deflection in order to characterize the structural behavior further, but as the propagating cracks caused element distortions, an accurate depiction would require a coarser mesh which in turn would lead to a less smooth profile. Subsequently, this was omitted from the thesis.

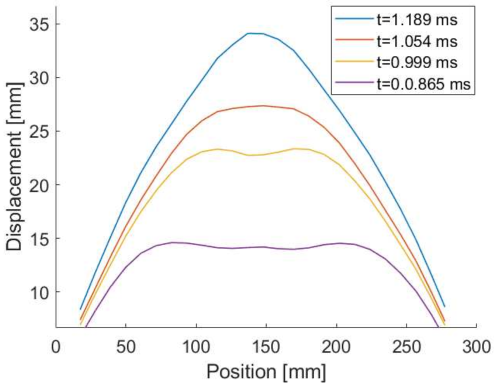

(a) D600_B1_0_25

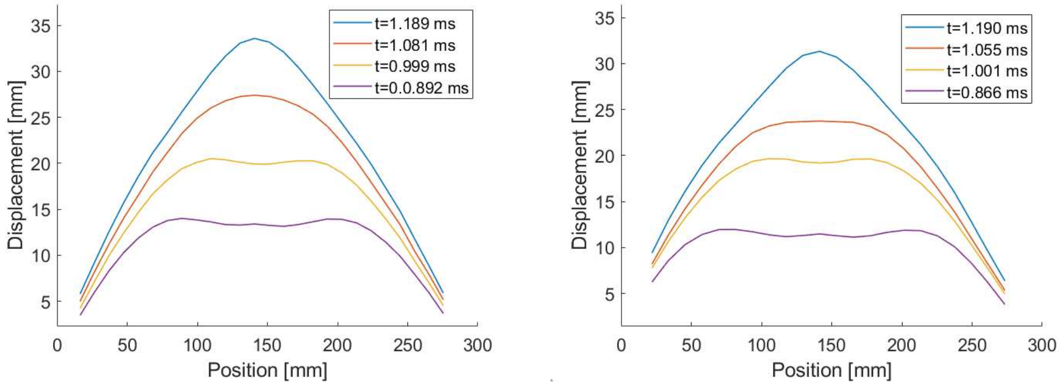

(b) D600_B2_0_25

(c) D600_B3_0_25

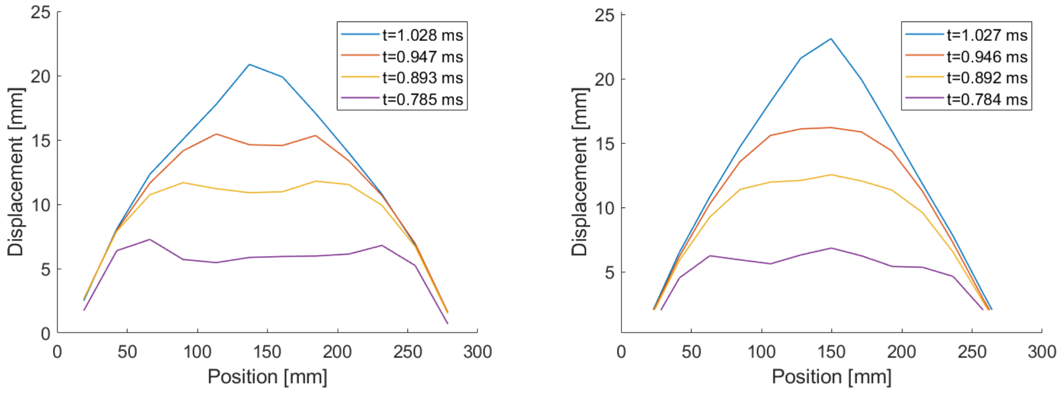

(d) D1400_B1_0_25

(e) D1400_B2_0_25

Figure 5.23: Deformation profiles obtained using 3D-DIC for all successfully conducted experiments at 25 bar.

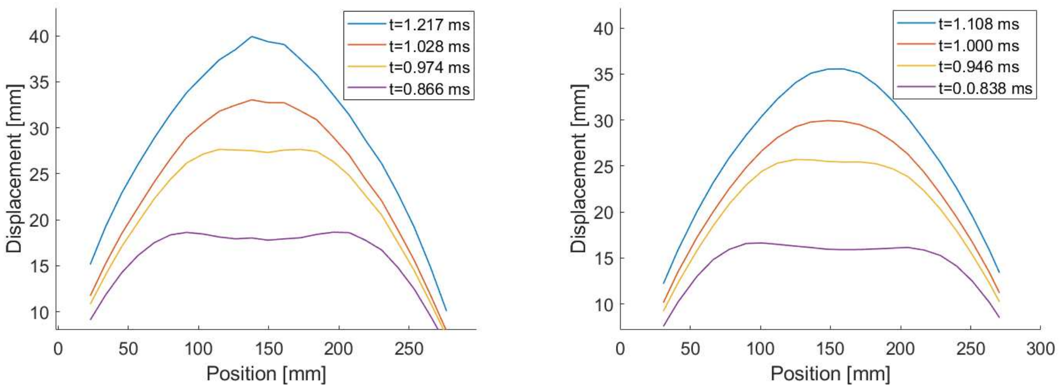

(a) D600_B1_0_35 **(b)** D600_B1_45_35

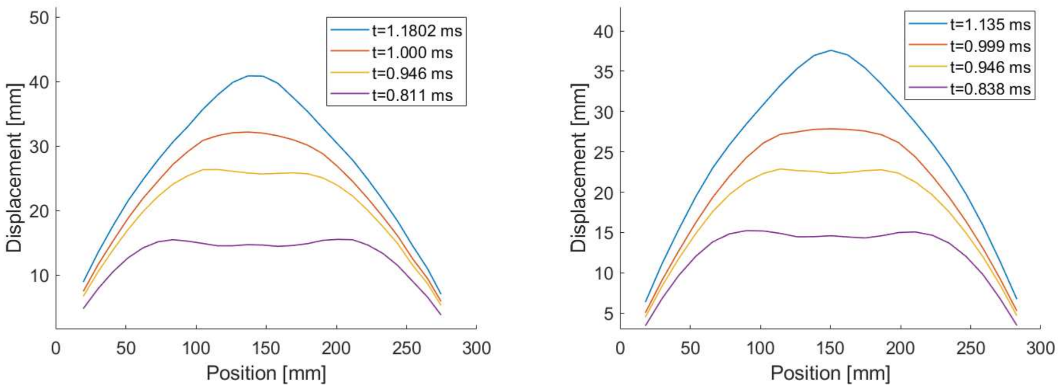

(c) D600_B2_0_35 **(d)** D600_B3_0_35

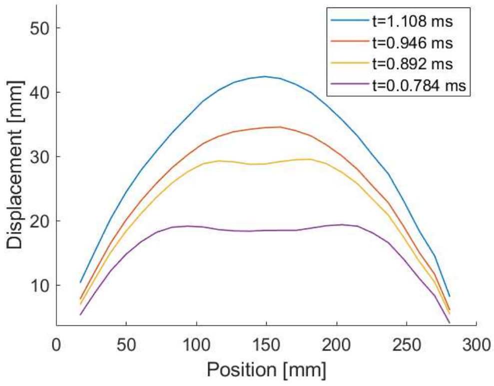

(e) D600_B1_45_60

Figure 5.24: Deformation profiles obtained using 3D-DIC for all successfully conducted experiments at 35 and 60 bar.

Laser Scanning

The results from the laser scan are presented as a full 3D pointcloud representation of the final deformation, as well as a deformation profile which has been extracted through the center of the plate along the horizontal axis. The choice of axis was observed to be indifferent, and since the deformation profiles were extracted using the horizontal axis in eCorr, this axis was selected for the laser scanning as well.

As the deformation profiles of the B1 configuration were selected at a small distance below the deactivated elements of the mesh (see Figure 5.19a), the final deformation profile obtained with 3D-DIC will deviate somewhat from that of the laser scanning. Efforts could be made to converge both results on the same location, but this was deemed too tedious, and subsequently, the final deformation profiles from 3D-DIC for the B1 configuration will not be presented in the following. Nevertheless, final deformation profiles obtained with the laser scanning will be presented for all experiments. The final deformation profiles were obtained with 3D-DIC by importing an image taken of the plate after the oscillations have calmed down and it was entirely stationary into the image-set of the 3D-DIC analysis. The eCorr software then tracked the speckle pattern as for the previous images. If the displacements of the speckles were large enough relative to the last frame, the software might have had problems with transferring the mesh, and this might have resulted in a distorted mesh. An example of such a distorted mesh is presented in Figure 5.25. Here, a fragment of the layering membranes got caught in the perforation, causing the mesh to distort heavily. It is also worth noticing that this also could be due to too large displacements relative to the last frame as well. It is further observed that some of the tracked subsets were not accurately tracked as well, which yielded an additional source of error.

The laser scan gave out a pointcloud-file which contained the spatial coordinates of each of the approximately 2,000,00 separately scanned points. These points were further processed in Matlab with a script by Granum *et al.* (2019) [13] which removed excessive points, and plotted the graphical 3D representation of the final deformations with colored contour plots to indicate the magnitude of displacement. The results have been sorted after configuration, material and firing pressure, and are presented in 5.26 for the B1 configuration, in Figure 5.27 for the B2 configuration, and in Figure 5.28 for the B3 configuration. To better differentiate the results, the results from the laser scan are marked with "Laser", whereas the results from 3D-DIC are marked with "DIC".

From the figures below, it is seen that Docol 600DL deforms more globally than Docol 1400M. This is linked to the strain hardenability of the material, which allow the plasticity to spread out across the plate. In addition, it is observed that Docol 600DL experiences more significant deformations than Docol 1400M, which is due to Docol 1400M having higher strength. It is also seen that the 3D visualization of the pointclouds was capable of accurately rendering and depicting the crack initiations and crack arrests of the experiments in question with good accuracy. It is further noticed that the difference in deformation profiles are seen to be negligible, or close to negligible, for the majority of the experiments. With the exception being experiment D1400_B2_0_25, where the two profiles only coincide at a small segment of the overall curve. This was mentioned in the previous section and was linked to a coarse mesh and the fact that crack propagations and oscillations caused the mesh to distort. In addition, the jump between the two last frames of the analysis could also be a contributing factor as well. From this, it can be readily concluded that both the laser scanning and the 3D-DIC gave quite similar results. Although the laser scanning proved to be more tedious than the 3D-DIC it still produced a very accurate representation and visualization of the results, and should, therefore, be considered as a viable method of representing data.

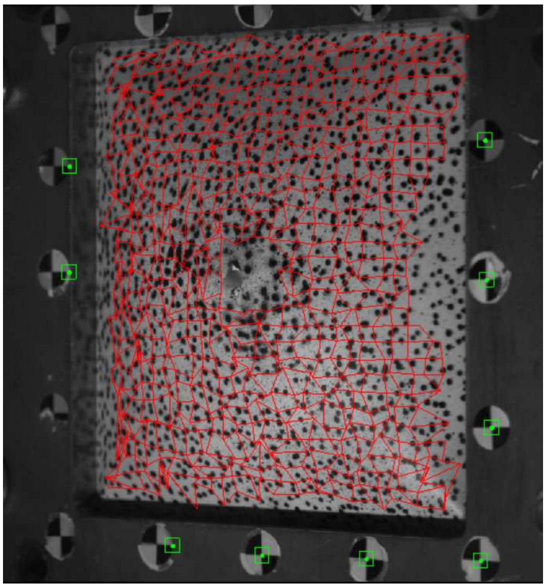

Figure 5.25: Excessive distortion of the mesh and the tracked subsets (indicated with green squares), during a 3D-DIC analysis.

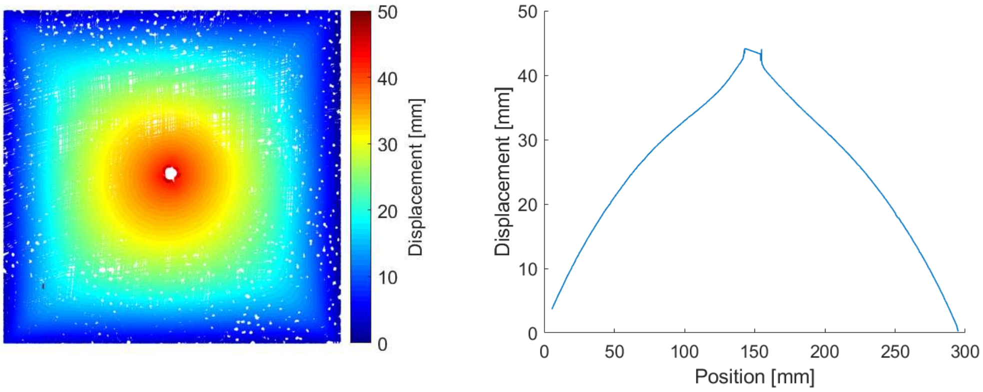

(a) D600_B1_0_35.

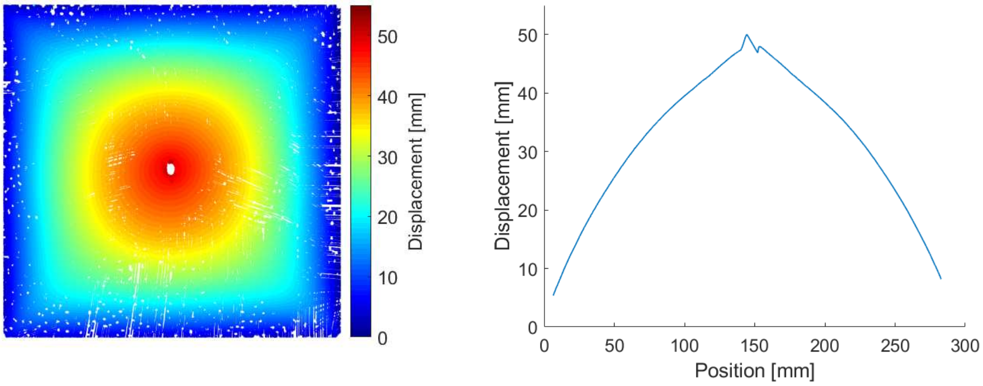

(b) D600_B1_45_60.

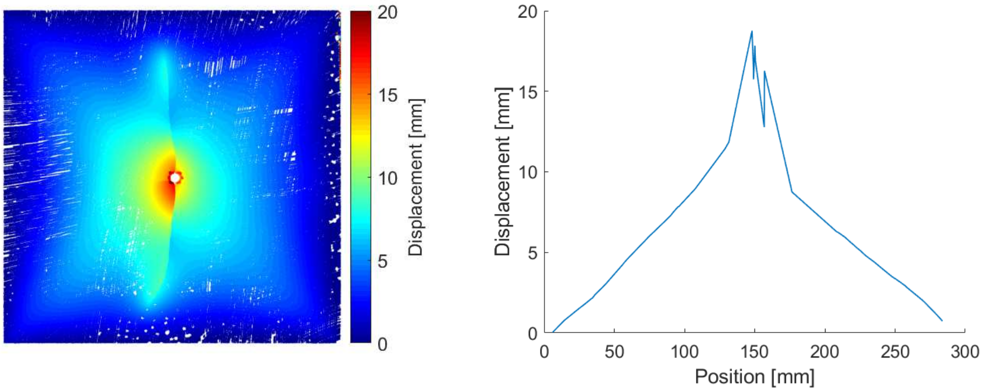

(c) D1400_B1_0_25.

Figure 5.26: Final deformation (left) and deformation profiles obtained along the horizontal axis, through the center of the plate (right), obtained user laser scanning for the B1 configuration.

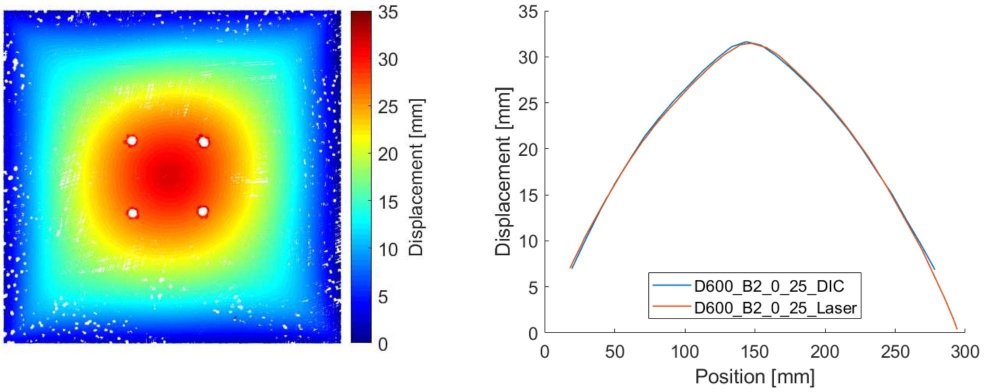

(a) D600_B2_0_25.

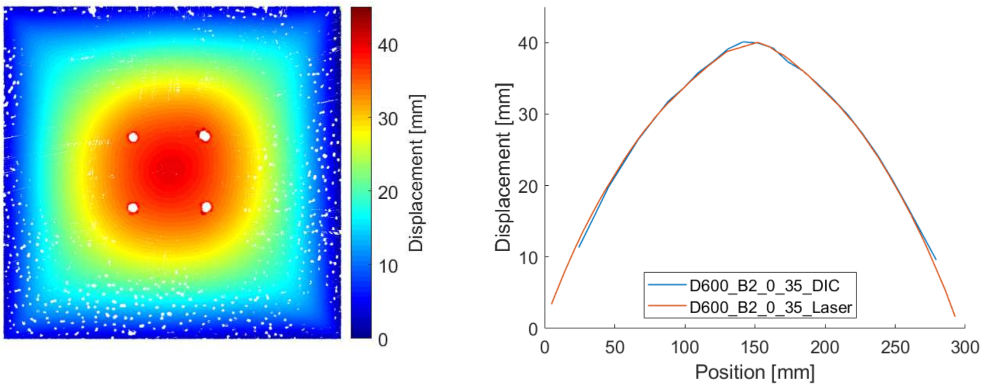

(b) D600_B2_0_35.

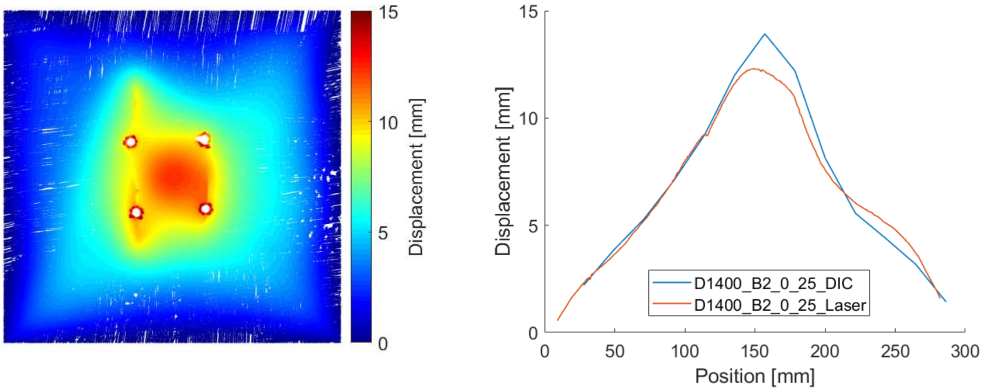

(c) D1400_B2_0_25.

Figure 5.27: Final deformation (left) and deformation profiles obtained along the horizontal axis, through the center of the plate (right), obtained user laser scanning for the B2 configuration. The deformation profiles have been compared to profiles obtained with 3D-DIC.

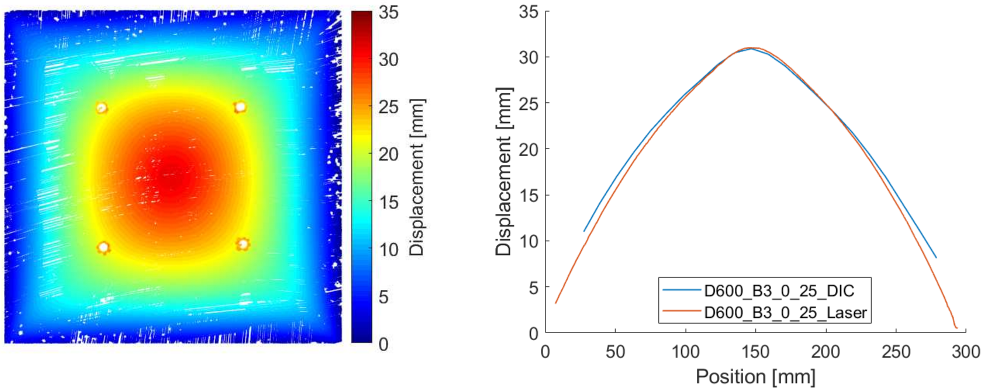

(a) D600_B3_0_25.

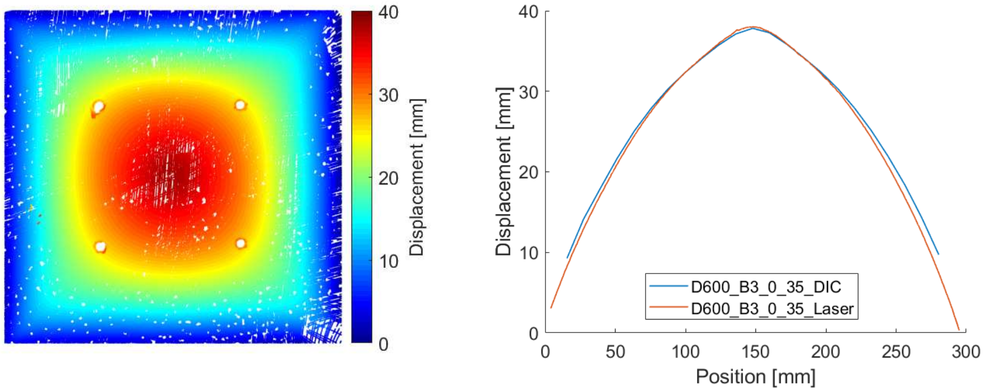

(b) D600_B3_0_35.

Figure 5.28: Final deformation (left) and deformation profiles obtained along the horizontal axis, through the center of the plate (right), obtained user laser scanning for the B3 configuration. The deformation profiles have been compared to profiles obtained with 3D-DIC.

5.3.3 Cracking

Experiments that experienced cracking are presented in the following in term of projectile perforation(s) prior to blast loading, and the resulting crack formation. For the Docol 1400M plates experiencing 25 bar, the crack propagation process has been presented as images from the high-speed footage. This section aims to identify the mechanism proving to be detrimental with respects to blast loading. In the following, the resulting cracks are named in a clock-wise manner, with the first crack being denoted "C1", the second "C2" and so on. The measured crack lengths have been presented in Table 5.9.

The crack initiation of experiments D600_B1_0_35 and D600_B1_45_60 are presented in Figure 5.29 and 5.30, respectively. Included in each figure is an image of the ballistic perforation prior to blast loading (left image) and the resulting crack formation when exposed to blast loading (right image). These images are oriented as they were mounted in the shock tube. From Figure 5.29 it is seen that the cracks formed during the blast loading follows the initial cracks of the perforation, and only through the gaps of the petals which extends to the base. This can also be observed in Figure 5.30 as well. Here it is noticed that no cracking occurred through the "eyelid" but originated at the base of the "eyelid" where it was observed to be some initial cracking (this can also be seen in Figure 5.6a and 5.6c as well). From this, it can be concluded that the capacity of the Docol 600DL plates increases when perforated at a 45° angle. This can be due to the fact that there exist more initiated cracks for normal impact, as previously specified.

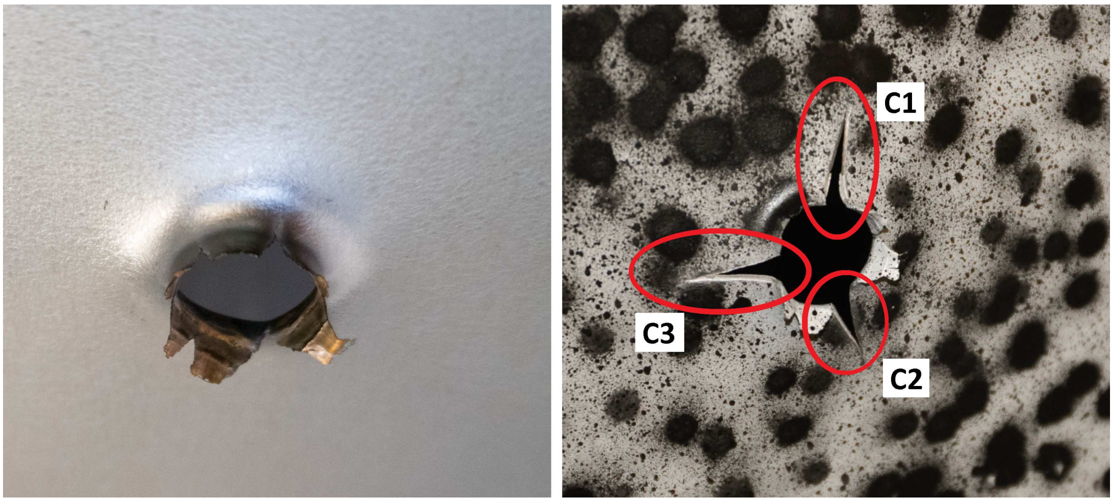

Figure 5.29: Perforation after ballistic impact (left) and after being exposed to blast loading (right), for experiment D600_B1_0_35. The images are oriented as it was in the shock tube, with vertical rolling direction. The cracks are named in a clock-wise manner, with "C1" being defined as the upper crack.

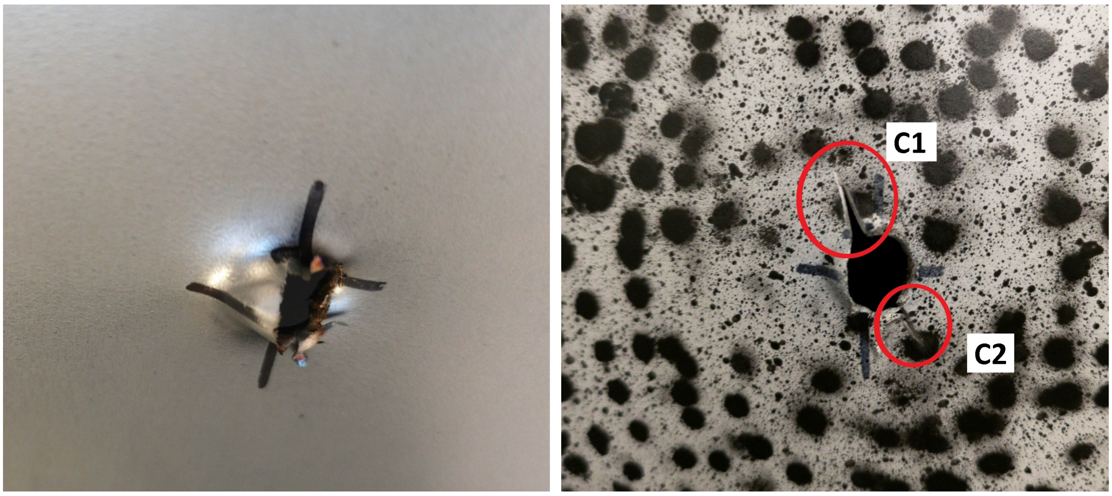

Figure 5.30: Perforation after ballistic impact (left) and after being exposed to blast loading (right), for experiment D600_B1_45_60. The images are oriented as it was in the shock tube, with vertical rolling direction. The cracks are named in a clock-wise manner, with "C1" being defined as the upper crack.

The crack growth processes for experiments D1400_B1_0_25 and D1400_B2_0_25 are depicted in Figure 5.32 and 5.33, respectively. From these images, it is readily observed that the cracks mainly propagate in the vertical direction, i.e., parallel to the rolling direction. It is further seen that the cracks further develop as the plate oscillates, which was linked to the low strain hardenability of the material. For experiment D1400_B1_0_25, it is noticed some crack growth in the horizontal direction as well, albeit not as significant as the vertical crack growth. This will be further presented.

The perforations for the two Docol 1400M plates are presented in Figure 5.31. Here, the leftmost image is the perforation of experiment D1400_B1_0_25, and the remaining images are D1400_B2_0_25, which are sorted in a clock-wise manner: with image 2 being the upper left perforation, image 3 being the upper right, image 4 being the lower right and image 5 being the lower left. From these images, it is observed that there exist small crack initiations between the petals reaching the base of the material. These initial cracks are further seen to be consistent with where the crack propagation process originates. From this, and the observations made from Docol 600DL, it can thus be concluded that these cracks lead the crack propagation as the material deforms due to blast loading.

Figure 5.31: Perforations of experiment D1400_B1_0_25 (image 1) and D1400_B2_0_25 (images 2, 3, 4 and 5) prior to blast loading. The numbering corresponds to that in Figure 5.32 and 5.33.

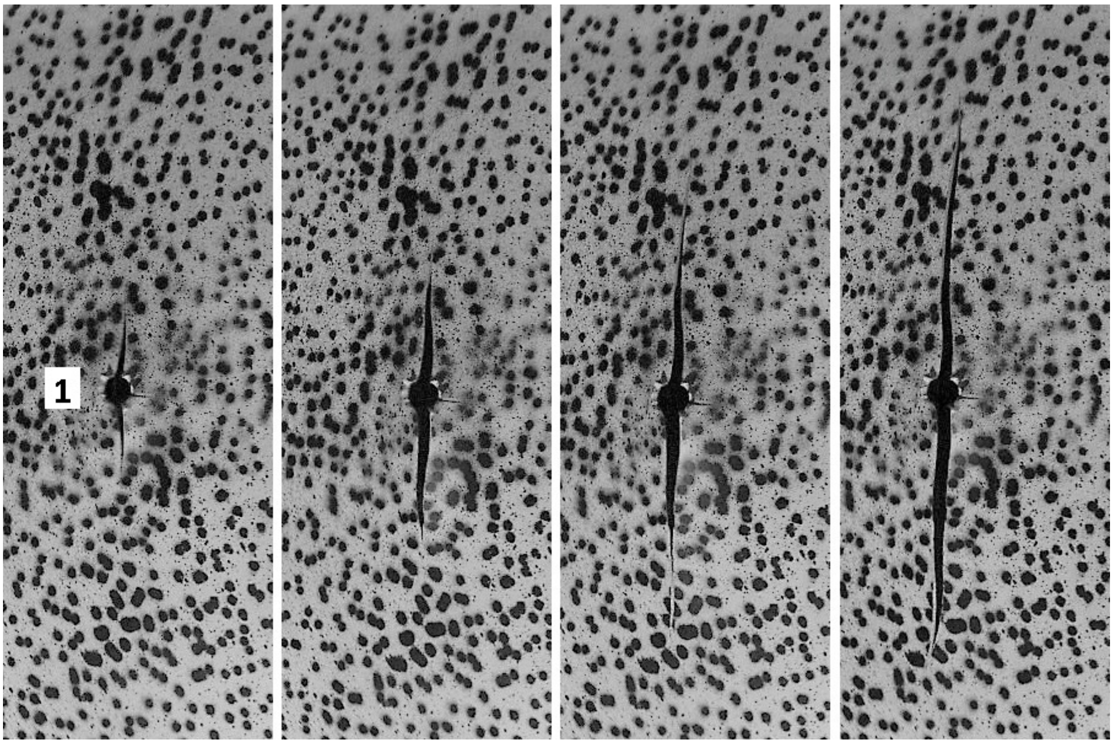

Figure 5.32: Images showing the crack growth process for experiment D1400_B1_0_25, finally leading to crack arrest. The images are zoomed in on the growing crack, which makes it easier to see. The images are taken at a time equal to 1.080 ms, 1.296 ms, 2.025 ms and 2.403 ms, respectively. The numbering of the perforation corresponds to that of Figure 5.31.

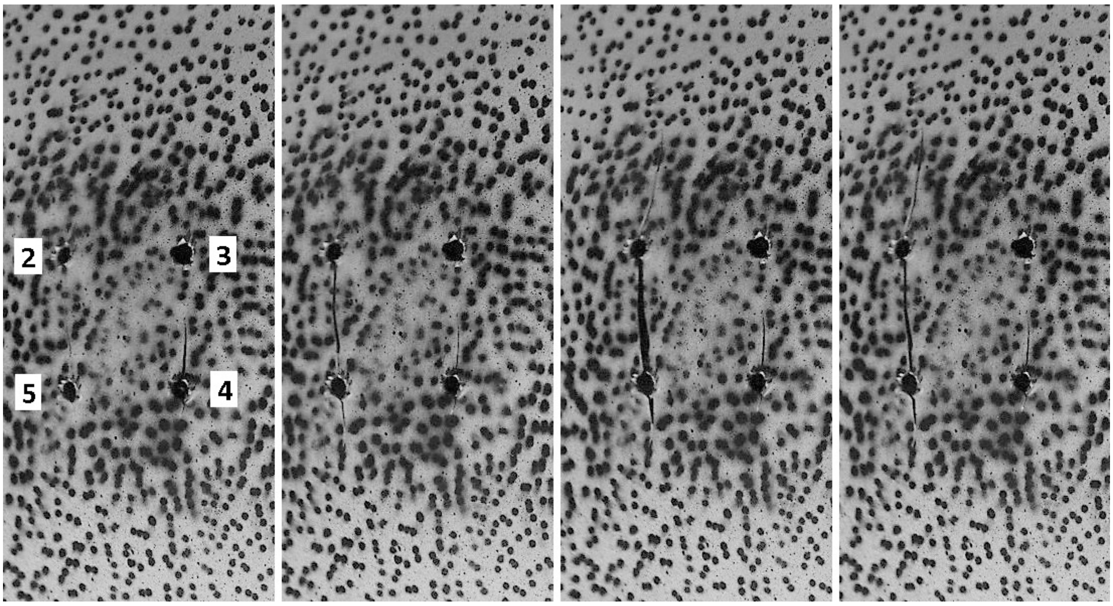

Figure 5.33: Images showing the crack growth for experiment D1400_B2_0_25, finally leading to crack arrest. The images are zoomed in on the growing crack, which makes it easier to see. The images are taken at a time equal to 1.055 ms, 1.201 ms, 2.010 ms and 2.372 ms, respectively. The numbering of the perforations corresponds to that of Figure 5.31.

Measured Crack Lengths

The measured crack lengths are presented in Table 5.9. The cracks were measured using a digital caliper, and it, therefore, exists some uncertainty in the measurements. The uncertainty was estimated to be ±0.5 mm. Due to uncertainties, the excessively long vertical cracks of the Docol 1400M were not measured. The naming convention for the cracks are presented in Figure 5.29 and 5.30 for Docol 600DL, and in Figure 5.34 for Docol 1400M. Here, the cracks have been named in a clock-wise manner, with "C1" being defined as the first crack.

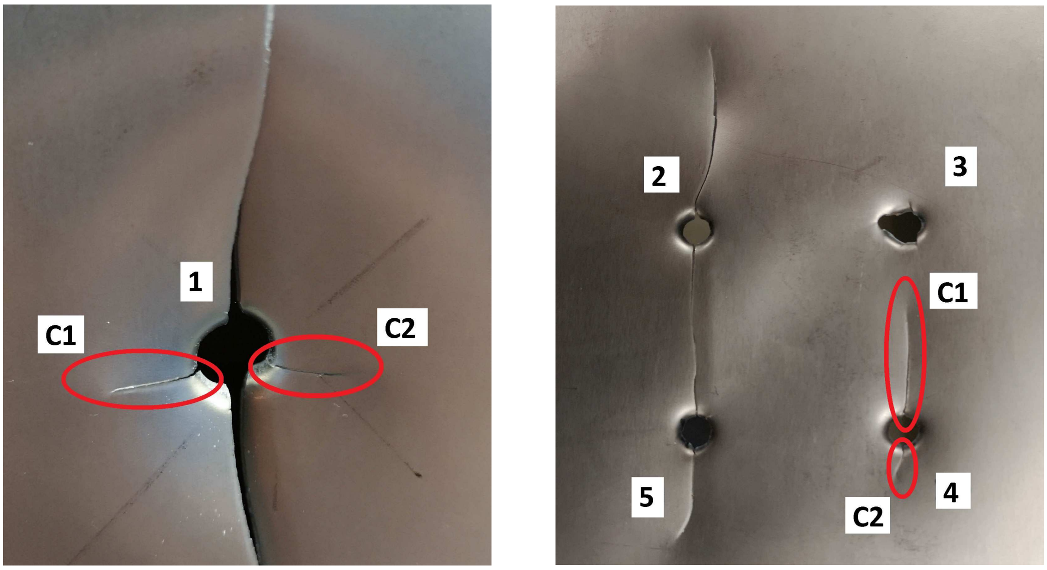

(a) D1400_B1_0_25 **(b)** D1400_B2_0_25

Figure 5.34: Naming of the cracks for Docol 1400M. The cracks are named in a clock-wise manner, with "C1" being defined as the first crack. (5.34a) Shows a zoom-in of the perforation in Figure 5.32, and (5.34b) shows a zoom-in of Figure 5.33.

Table 5.9: Measured crack lengths for the experiments. The naming convention of the cracks follows from Figure 5.29, 5.30 and 5.34.

Experiment	**C1** [mm]	**C2** [mm]	**C3** [mm]
D600_B1_0_35	8.66	9.06	9.24
D600_B1_45_60	9.07	6.67	-
D1400_B1_0_25	11.52	8.55	-
D1400_B2_0_25	51.08	7.47	-

5.4 Concluding Remarks

Petaling was the primary failure mode for all experiments, and the perforations were observed to be close to identical for both materials. The exception was that Docol 1400M exhibited more prominent cracking.

The difference in velocities differed negligibly between experiments and the maximum deviation between initial- and residual velocity was 1.99%.

The test matrix obtained in the preliminary study was in good agreement with the experimental results. The exceptions were Docol 600DL which exhibited cracking for the B1 configuration at 35 bar, and the B2 configuration using Docol 1400M at 25 bar and 35 bar which exhibited crack arrest and total failure, respectively.

For the pressure-time data using Docol 600DL, it was observed negligible differences between plates experiencing normal- and oblique impact, and for the B1- and B3 configuration. These differences were seen to increase with increasing pressure. There were made observations of FSI effects, seen as deviations in peak reflected pressure compared with the calibration results. This effect was seen to increase as the pressure increased.

Docol 1400M exhibited total failure at 35 bar for both configurations, whereas Docol 600DL only showed small signs of cracking for the B1 configuration at 35 bar. From Figure 5.26, 5.27 and 5.28, it was noticed that Docol 600DL deformed more globally, which was linked to the strain hardenability of the material. In addition, Docol 600DL exhibited a more significant amplitude of maximum deflection compared to Docol 1400M, which was coupled to Docol 1400M possessing a higher strength, which in turn lead to a lesser extent of deformations before fracture. At 25 bar Docol 1400M experienced crack arrest with long horizontal cracks whereas Docol 600DL experienced purely deformations. This shows that ductility and strain hardenability are more important material properties than strength when considering blast loading.

For Docol 600DL, it was seen that the angle of impact affected the capacity of the plates, where oblique impact was observed to yield the highest capacity. It was further concluded that the initial cracking of the perforations lead the direction of the crack propagation as the plates deformed due to blast loading.

The results obtained with 3D-DIC were observed to be in good agreement with the laser measurements, except for the B2 configuration using Docol 1400M at 25 bar where only segments of the curves coincided. This was linked to excessive mesh distortion due to crack propagation. Due to fewer sources of error, and exceptional reported point repeatability, the laser arm was deemed the most trustworthy. It also serves an excellent tool for inspecting cracks and other details.

Chapter 6

Numerical Study Part I

6.1 Introduction

In this chapter, a numerical study has been conducted on the ballistic impact. The ballistic study includes an assessment of elastic-, elastoplastic- and rigid projectiles with respect to run-time and potential damage, as well as a mesh sensitivity study over the thickness. The aim of this chapter is to assess what choice of numerical projectile and element size that is favorable when modelling the combination of ballistics and blast loading.

6.2 Numerical Models

Recalling from Chapter 5, initial- and residual velocities of the projectiles were around 900 m/s. At such high velocities, the plastic deformations were highly localized, and it proved sufficient to only consider a plate segment instead of the entire plate for this study. This significantly reduced computational time for the simulations. For such problems, the boundary conditions were of little importance, and they were therefore modelled as fixed. The initial velocity was selected to be 900 m/s, as the average of all ballistic experiments were somewhere above this velocity. As specified in Section 2.5, all simulations in this and the next chapter was run using a friction coefficient equal to zero.

For this study, axisymmetric- and solid element models with different element sizes were considered. Shell element models will not give an accurate response when subjected to impact loading, and thus, no further studies were conducted with these models. The naming convention in the following chapter is a continuation of the labeling convention used in the preliminary study, and are presented in Table 6.1, which specifies the material, angle of impact, element type used (restricted to C3D8R and CAX4R for this study), element size/number of elements over the thickness and the modelling of the projectile. The general label name is given on the form of ***DMMM_XX_AA_YY_Z***.

Table 6.1: Naming convention used to label different models in this Chapter. General label name: ***DMMM_XX_AA_YY_Z***

Part of Name	**Possible Configurations**	**Explanation**
DMMM	D600	Docol 600DL
	D1400	Docol 1400M
XX	C3D8R	Solid element, reduced integration
	CAX4R	Axisymmetric element, reduced integration
AA		Normal impact
	45	45° impact
YY	0xx	Mesh size of 0.xx mm (C3D8R)
	xx	Number of elements (CAX4R)
Z	Elastic	Elastic projectile
	Elastoplastic	Elastoplastic projectile
	Rigid	Analytical rigid projectile

The model parameters used in the following two numerical studies (Chapter 6 and 7) are the same used in the preliminary study in Chapter 4. The parameters are presented in Table 6.2.

Table 6.2: Model parameters used in the final numerical studies.

Material	A [MPa]	Q_1 [MPa]	C_1 [-]	Q_2 [MPa]	C_2 [-]	c [-]	m [-]	$\dot{p}_0$ [s^{-1}]	W_c [MPa]
600DL	325.7	234.8	56.2	445.7	4.7	0.01	1	$5*10^{-4}$	555
1400M	1200	253.6	773.5	97	135	0.004	1	$1*10^{-3}$	741

6.2.1 SIMLab Metal Model

In the two following numerical chapters (Chapter 6 and 7), the SIMLab Metal Model (SMM) has been used. The model in Chapter 4 was a simplification of the SMM. It enables the use of other yield surfaces, by the use the high-exponent Hosford yield function. Here, the shape of the yield surface for Docol 1400M was given by n=6, and Docol 600DL still used von Mises. It takes in 36 parameters for Docol 600DL and 37 for Docol 1400M. The reader is referred to [84] for further reading on the SMM.

6.2.2 Axisymmetric Element Models

Axisymmetric models have been used as they are not as computationally expensive as solid element models, and thus able to run simulations with well over 100 elements over the thickness. The downside is that these models are not able to depict crack initiation and growth around the perforation. The modelled segment had a length of 25 mm and a height equal to the plate thickness, which was mirrored about the vertical axis.

The axisymmetric element models in this study applied quadratic CAX4R elements with reduced integration, element distortion control, and enhanced hourglass control. Element distortion control is used to keep elements from distorting excessively [85]. Enhanced hourglass control is applied to restrain the zero-energy modes to a larger extent than the default setting. In addition, a pinhole of radius 0.1 mm was introduced to the model at the point of impact. This can be introduced such that no failure criterion needs to be applied or to stop numerical instabilities. These controls and the addition of a pinhole was necessary as the models experienced excessive element distortion, resulting in premature abortions.

Meshing

The axisymmetric element models were meshed with a total of 3, 10, 25, 50, 75, and 100 elements over the thickness. The model was divided into partitions, such that the finest elements were placed in the area of contact, with a transition to the coarsest elements near the boundary. This was done to reduce the overall computational time of the problem.

6.2.3 Solid Element Models

The solid element models in this study applied quadratic C3D8R elements with reduced integration and built-in hourglass control. The element sizes of the plate segment were in the range of 0.26 mm to 1 mm, and the deformable projectiles had an approximate minimum element size of 1 mm. The modelled plate segment was 50 mm x 50 mm.

Meshing of Plate Segments

The meshing of the deformable projectiles is described in detail in Section 6.2.3. The plate segments were partitioned using the structured meshing algorithm (previously described in Section 4.2). The partitioning is depicted in Figure 6.1a, and the meshing using an approximate minimum element size of 0.26 mm is depicted in Figure 6.1b. The center circle of the partition, which had a diameter of 14 mm and defined the area of contact, were meshed using 0.26 mm elements. For meshing of the remaining parts of the plate segment, the element size was selected to be 0.8 mm in the outer circle and 1 mm in the remaining parts.

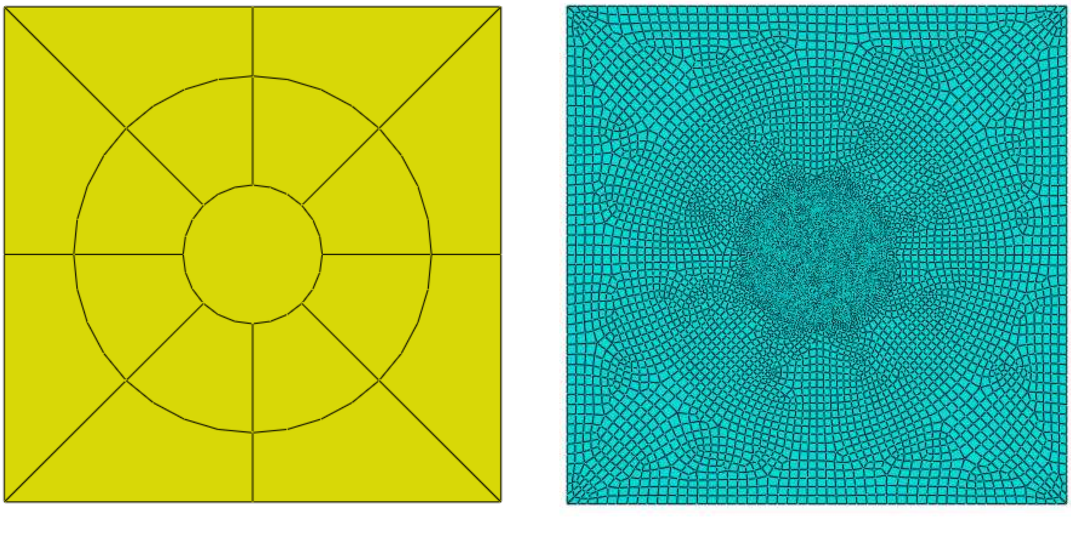

(a) **(b)**

Figure 6.1: Partitioning and meshing the solid element model. (6.1a) Shows the partitioning and (6.1b) shows the meshing using an minimum element size of 0.26 mm.

Numerical Projectiles

The projectiles used in this numerical study were modelled after the 7.62 mm AMP2 bullets used in the ballistic experiments. The exact measurements and necessary material- and model parameters were taken from Børvik *et al.* (2009) [28].

Analytical rigid projectile

An analytical rigid part is used to represent a part that has a significantly higher stiffness than the rest of the model, and deformation can be neglected [86]. The benefit of such a projectile is that it does not require meshing, which reduces the overall computational time. A reference point was applied to the center of the base with a weight of 10.5 g. The reference point was used to give the projectile an initial velocity and track it during simulations.

Elastic- and Elastoplastic Projectiles

Modelling the entire assembled projectile adds to the complexity, which in turn increases the computational time. Therefore, the deformable projectiles were modelled as a complete solid, consisting of a homogeneous material, namely brass. To ensure that the numerical projectiles had the same weight as the experimental projectiles, the density was calculated using the overall volume of the projectile. The density ρ, Young's modulus E and the Poisson's ratio ν as well as the calculated model parameters using the *Power law*, are presented in Table 6.3. For the deformable projectiles, the Johnson-Cook failure criterion was utilized. The model constants are presented in Table 6.4, and the criterion is given as [42]

$$p_f = [d1 + d2exp(d3\sigma^*)][1 + d4ln(\dot{p}^*)][1 + d5T^*] \tag{6.1}$$

where d1, d2, d3, d4 and d5 are model constants, p_f is the failure strain, $\dot{p}^*$ is the user-defined strain rate, σ^* is the stress triaxiality and T^* is the homologous temperature. Fracture is assumed to occur when the damage variable reach unity, i.e., when

$$D = \int_0^p \frac{dp}{p_f} = 1 \tag{6.2}$$

Table 6.3: Material- properties and parameters for the elastoplastic projectile. All values, except the density, are taken from [28].

E [MPa]	ν	ρ [kg/m^3]	A [MPa]	B [MPa]	n	m	c	$\dot{p}_0$ [s^{-1}]
115000	0.31	7939.5	206	505	0.42	1.68	0.0108	0.0005

Table 6.4: Parameters for Johnson-Cook damage used for the elastic- and elastoplastic projectiles. Taken from [28]

d1	d2	d3	d4	d5	Melting Temperature [K]	Transition Temperature [K]	$\dot{p}_0$ [s^{-1}]
0.5072	1.446	1.1512	0	0	1189	1180	0.0005

In contrast to the analytical rigid projectile, the elastic- and elastoplastic projectiles required meshing. Consequently, a finer mesh required a higher computational time than a coarser mesh. For the following simulations, an approximate element size of 1 mm was used for both projectiles. The meshing of the projectiles is depicted in Figure 6.2.

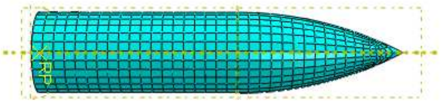

Figure 6.2: Meshing of the elastic- and elastoplastic projectiles. Approximate element size is 1 mm.

6.3 Results

The results from the projectile- and mesh study are presented separately. The conservation of energy plots are presented in Appendix A.2 as the total energy was observed to differ negligibly from constant for all conducted simulations in this chapter. Further, the artificial strain energy plots from the projectile study are presented in Appendix A.2 as well, as the ratios were sufficiently low.

Mesh Sensitivity Study

An analytically rigid projectile was used for simplicity. This assumption was further tested in the next section. Figure 6.3 shows the residual velocity using 3, 10, 25, 50, 75 and 100 elements over the thickness with an initial velocity of 900 m/s for both materials. Here, it is seen that an increase of elements leads to a higher residual velocity. A similar trend was observed by Holmen *et al.* (2017) [87], who noticed that ogival nose-shaped projectiles gave an approximately linear relation for high velocities, with a lower residual velocity for coarser elements, followed by a slight kink in the curve as the mesh was refined. This phenomenon was seen to be more prominent as the initial velocity approached the ballistic limit velocity. From the figure, it is further observed that the difference in residual velocities are maximum 1 m/s, and can thus be considered negligible. From this, it can be concluded that mesh refinement has little influence on the target plate in this study.

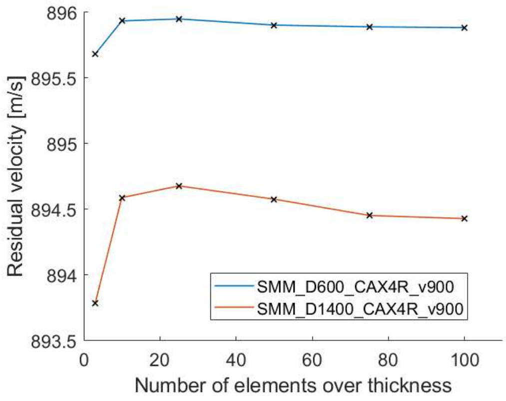

Figure 6.3: Residual velocity plotted for 3, 10, 25, 50, 75 and 100 elements over the thickness for both materials using an initial velocity of 900 m/s.

Motivated by these results, it was decided to run the same study with lower initial velocities. Firstly at v_i=450 m/s and then at v_i=200 m/s. This was done to determine if the differences were more prominent as the initial velocity was decreased. The results are plotted in Figure 6.4a for Docol 600DL and in Figure 6.4b for Docol 1400M. From the figures, it can be observed that the residual velocities are constant for both materials. Consequently, simulations using 75 and 100 elements over the thickness with an initial velocity of 200 m/s were omitted for both materials. Ergo, it can be concluded that mesh refinement and variation of the initial velocity has little to no effects on the residual velocities in this case.

All simulations were run using a friction coefficient equal to zero, which gave a conservative response. To get a feel of potential friction coefficients, a selection of suggestions are presented. Ravid and Bodner (1983) [88] suggested a coefficient of 0.1 for metal working, with 0.05 for impact with higher velocities and temperature. Zukas *et al.* (1990) [89] proposed a value 0.01 for metal-to-metal ballistic impact. Holmen *et al.* (2017) observed that an increase of this coefficient leads to a reduction in residual velocity, which is quite reasonable. They further noticed that the strain rate sensitivity parameter c had a significant impact on the residual velocity, with a higher value for c yielding a lower residual velocity. A parametric study on strain rate sensitivity has been conducted in Section 7.3.3, where the primary focus was on the blast load response.

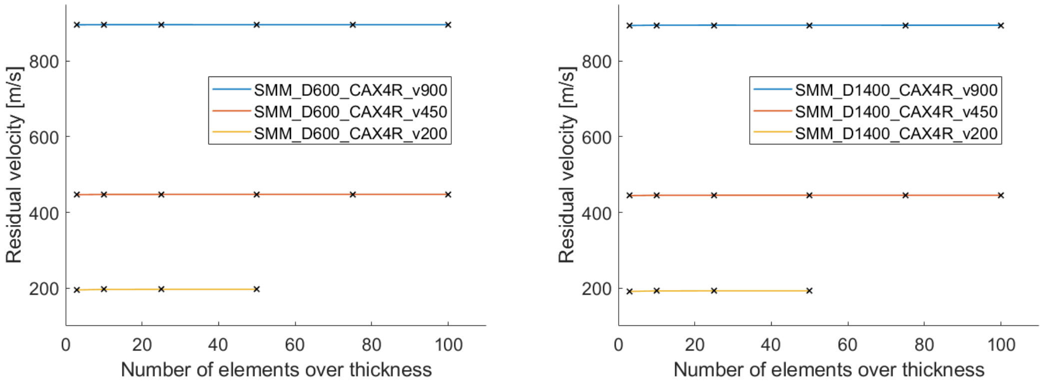

(a) (b)

Figure 6.4: Residual velocities plotted for several elements over the thickness, using initial velocities of 900, 450 and 200 m/s. (6.4a) For Docol 600DL and (6.4b) for Docol 1400M.

To validate and assess the simulations, artificial energy plots are presented. Only three and ten elements over the thickness are presented, as it was observed in the preliminary study that coarser elements gave a higher ratio. The plots are presented in Figure 6.5. Included are the ratio of artificial strain energy (ALLAE) divided by the sum of the internal energy (ALLIE) and the kinetic energy (ALLKE). As recalled, this ratio should be negligible compared with "real" energies [40], [41]. From the figure, it is observed that coarser mesh yields a higher ratio. Also, it is observed that a reduction in velocity leads to an increase in this ratio as well, which may be explained by the increasing global deformations of the plates.

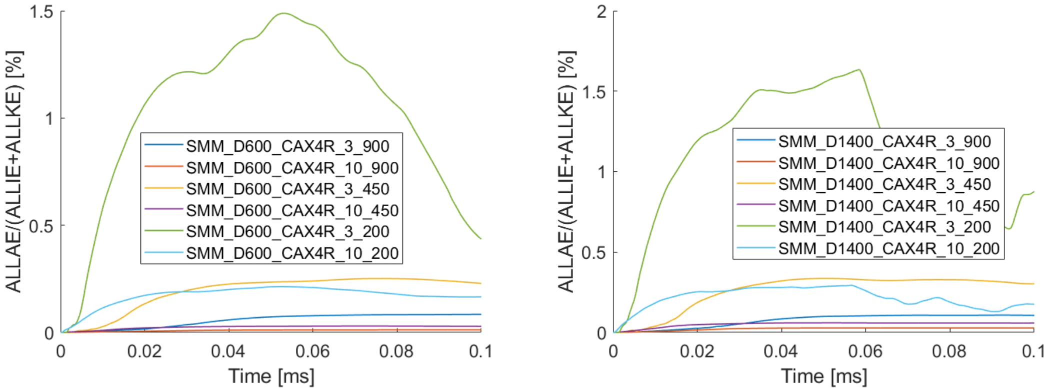

(a) **(b)**

Figure 6.5: Artificial strain energy plots. (6.5a) Shows for Docol 600DL and (6.5b) shows for Docol 1400M.

Projectile Study

No differences in the entry- and exit holes were observed when using the different projectiles, which was expected. The resulting perforations are presented in Figure 6.6 and 6.7. The perforations have been visualized by the use of the damage variable (denoted SDV_D in Abaqus), which is a normalization of the previously defined fracture parameter SDV_W. From the figures, petals are seen for normal impact and a set of "eyelids" for oblique impact, which is consistent with the experimental work. It can further be noticed that the perforation edges are rather coarse and exhibit more cracking than the experiments. This is due to the fact that these models only have three elements over the thickness, but they give a relatively accurate representation.

To accurately depict ballistics, numerous elements over the thickness are needed, as it is a highly localized problem. On the contrary, blast loading is very much a global problem, and thus, several elements over the thickness will be too complex and computationally expensive. For such problems, shell element models are generally preferable. Stensjøen and Thorgeirsson (2017) [9] concluded that several elements over the thickness were necessary to depict the crack propagation of numerical blast loading accurately. From this, it subsequently follows that adjustments and sacrifices must be made in other to best model the combination impact- and blast loading. It can thus be concluded that three elements over the thickness are sufficient for this problem, as the initial cracking were accurately depicted to a certain degree.

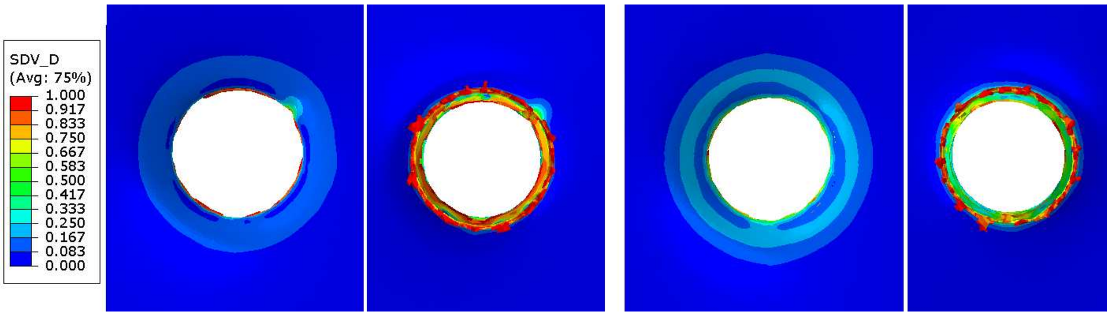

Figure 6.6: Entry- (image 1) and exit hole (image 2) for Docol 600DL, and entry- (image 3) and exit hole (image 4) for Docol 1400M. Both perforations are given by normal impact.

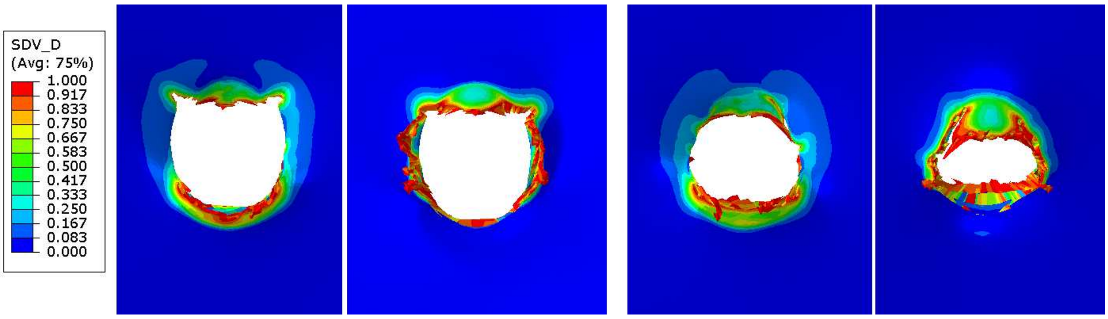

Figure 6.7: Entry- (image 1) and exit hole (image 2) for Docol 600DL, and entry- (image 3) and exit hole (image 4) for Docol 1400M. Both perforations are given by an impact angle of 45 °.

As the elastic- and elastoplastic projectiles did not experience any considerable deformations, it may consequently be inexpedient to model the projectiles as such. Computational time is an important factor for numerical modelling, and it is desirable with as low computational time as possible. The different projectiles have, therefore, been assessed based on their respective run-time. The run-times of the projectiles are presented in Table 6.5. From the table, it is readily observed that an analytical rigid projectile gives the lowest run-time in the majority of cases. Based on this, it can thus be concluded that analytical rigid projectiles are most beneficial for this thesis. Consequently, all further projectile were modelled as analytical rigid.

Table 6.5: Run-time for each numerical projectile for the two materials at an impact angle of 0° and 45°.

Material	**Projectile**	**Impact Angle** [°]	**Run-time [min:s]**
D600	Elastic	0	53:18
	Elastoplastic	0	32:16
	Rigid	0	08:27
D600	Elastic	45	24:18
	Elastoplastic	45	15:21
	Rigid	45	08:10
D1400	Elastic	0	55:10
	Elastoplastic	0	35:36
	Rigid	0	23:55
D1400	Elastic	45	16:38
	Elastoplastic	45	21:12
	Rigid	45	18:06

Although deemed impossible for the modelling of blast loading, a further numerical study was conducted using six elements over the thickness. As three additional elements severely increased the computational time, a decision was made to only model a plate-segment with dimensions 14 mm x 14 mm using an uniform element size of 0.13 mm. The sole purpose of this study was to see if an increase in the number of elements over the thickness had any significant effects on both the residual velocity and the resulting perforations. The difference in residual velocity was seen to be less than 1 m/s and was therefore omitted. The resulting perforations are presented in Figure 6.8.

Here, it is observed more prominent cracking and petals, which may be linked to the prescribed fracture parameter. As the element size decreases, the accumulated damage of the integration points is spread out across a smaller area. By not increasing this parameter, a critical value will be reached faster for smaller elements, and the element is eroded. This parameter should, therefore, be increased. A parametric study was conducted to illustrate this in Section 7.3.3.

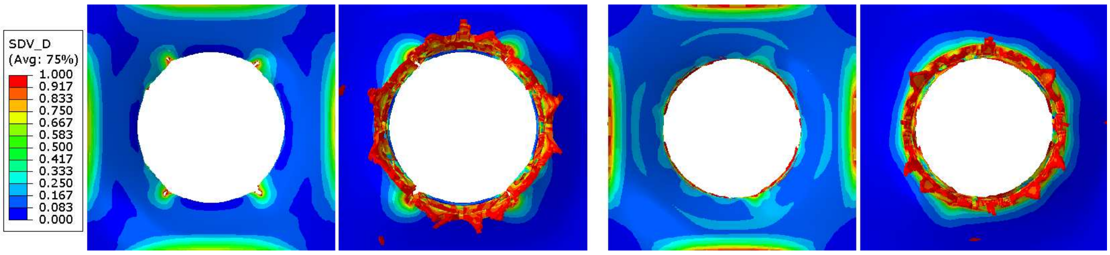

(a) Entry- (image 1) and exit hole (image 2) for Docol 600DL, and entry- (image 3) and exit hole (image 4) for Docol 1400M. Both perforations are given by normal impact.

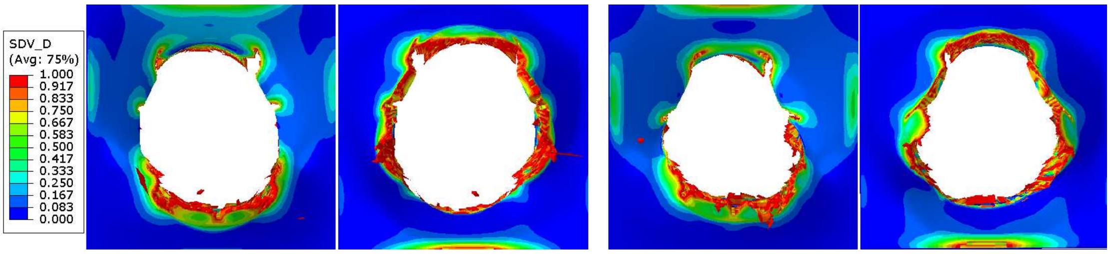

(b) Entry- (image 1) and exit hole (image 2) for Docol 600DL, and entry- (image 3) and exit hole (image 4) for Docol 1400M. Both perforations are given by an impact angle of 45 °.

Figure 6.8: Entry- and exit holes for Docol 600DL and 1400M using six solid elements over the thickness of the numerical model. (6.8a) Depicts the resulting perforations from a normal impact and (6.8b) depicts the resulting perforations from a impact at 45°.

6.4 Concluding Remarks

It was seen negligible differences in the residual velocity as the mesh was refined, and as the initial velocity was decreased towards the ballistic limit velocity. Further, it existed negligible differences in the residual velocities when comparing the materials, which was consistent with the experimental work. The residual velocities were noticed to deviate some from the experimental results, although it can be concluded that these deviations were negligible.

It was established that impact loading requires numerous elements over the thickness to accurately predict the failure modes, whereas it is more convenient for blast loading to employ shell element models. Based on this, coupled with the findings of the studies in this chapter, it was concluded that an element size of 0.26 mm was the most beneficial for this thesis. Also, the resulting perforations yielded somewhat coarse petals, which was accredited to the lack of elements over the thickness. Nevertheless, the results were deemed to be in good agreement with the experiments, based on the underlying assumptions. Further, it was observed that the deformable projectiles did not experience any significant deformations and that an analytical rigid projectile tended to give the lowest run-time in most cases. Based on this, it was subsequently concluded that an analytical rigid projectile was more than sufficient for modelling the ballistics of this thesis.

An additional study was conducted using six elements over the thickness of an even smaller plate segment, in order to assess to resulting perforations and residual velocity. The change in residual velocities was found to be insignificant, and the perforations were observed to be coarser due to the prescribed fracture parameter being too low.

Chapter 7

Numerical Study Part II

7.1 Introduction

This chapter will serve as a final numerical study. Numerical studies have been conducted on the combination of impact- and blast loading in an attempt to reproduce the experimental results, which will be validated and evaluated through comparison with data from the SSTF. These results are firstly sorted after the angle of impact, and secondly after impact- and blast loading. In addition, a parametric study has been conducted on the Cockcroft-Latham fracture parameter W_c as well as the strain rate sensitivity parameter c. This chapter aims to see to what degree the experimental results can be approximated numerically and to determine some of the factors that may affect the numerical structural response when exposed to the combined impact- and blast loading.

7.2 Numerical Models

In this study, only solid element models have been considered. The naming convention from the previous numerical study has been continued to a degree in this study, with a general label name on the form **DMMM_CC_AA_MC_tt**. The naming convention is presented in the Table 7.1. The material parameters are the same used in the previous chapter and are presented in Table 6.2.

Table 7.1: Naming convention used to label different models in this chapter. General label name: ***DMMM_CC_AA_MC_tt***.

Part of Name	Possible Configurations	Explanation
DMMM	D600	Docol 600DL
	D1400	Docol 1400M
CC	BHX	Ballistic Hole, geometry X
AA		Normal impact
	45	45° impact
MC	M1	Mesh configuration using structured mesh
	M2	Mesh configuration using sweep mesh
tt	xx	Nominal firing pressure of xx [bar]

The BHX configurations are presented in Figure 7.2, along with an overview over which perforation that was considered when presenting data. The configurations have been distinguished by color-codes. In the following, a yellow square indicates the BH1 configuration, orange indicates BH2, and red indicates BH3.

The location of the reference points are visualized in Figure 7.1a and 7.1c. Here, the red dot indicates the reference point for configurations BH2 and BH3. The blue dot indicates the reference point for the BH1 configuration. The distance between the two was 8.5 mm. Two different meshing configurations were used in this study, which was done to determine the best-suited technique for impact- and blast loading. The partitioning of the two configurations is presented in Figure 7.1. The meshing configurations are presented shortly for more insight:

- **Mesh configuration 1**, denoted M1, has a square zone surrounding the impact zone where the element sizes were equal to 0.26 mm. The rest of the mesh had an element size of either 1 mm or 2 mm, with 2 mm being the element sizes situated outside of the "cross". The structured meshing algorithm was used. The partitioning and meshing are depicted in Figure 7.1a and 7.1b, respectively.
- **Mesh configuration 2**, denoted M2, has circular zones surrounding the impact zone. An element size of 0.26 mm was used within this impact zone. The rest of the mesh was a transition to an element size of 3 mm. The advancing front sweep meshing algorithm has been used. The partitioning and meshing are depicted in Figure 7.1c and 7.1d, respectively.

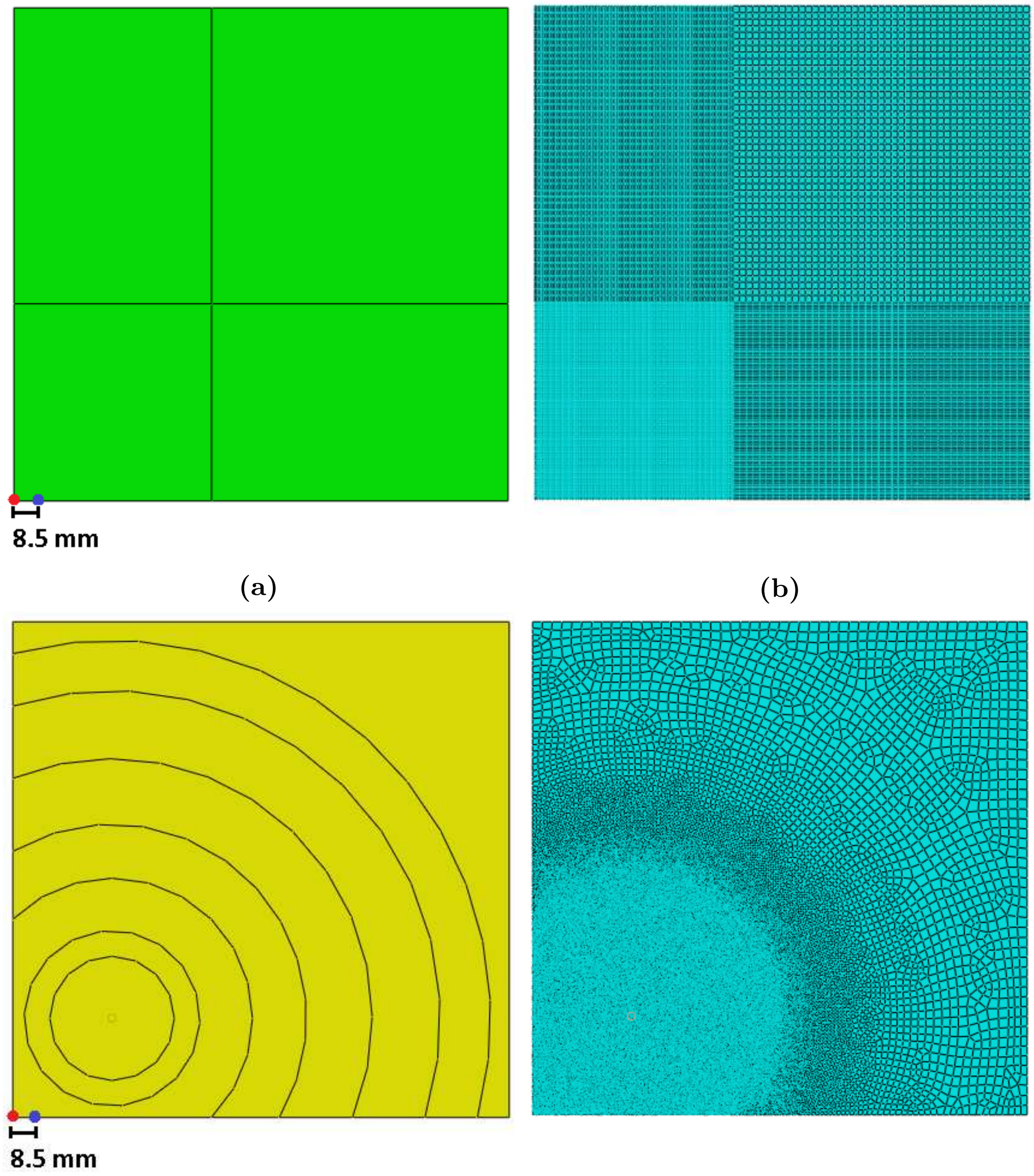

(a) (b)

(c) (d)

Figure 7.1: Partitioning and meshing of the mesh configurations. (7.1a) And (7.1b) shows the partitioning and meshing of the M1 configuration, and (7.1c) and (7.1d) shows the partitioning and meshing of the M2 configuration. Here, the red dot indicates the reference point for configurations BH2 and BH3, and the blue dot indicates the reference point for BH1. The distance between the two was 8.5 mm.

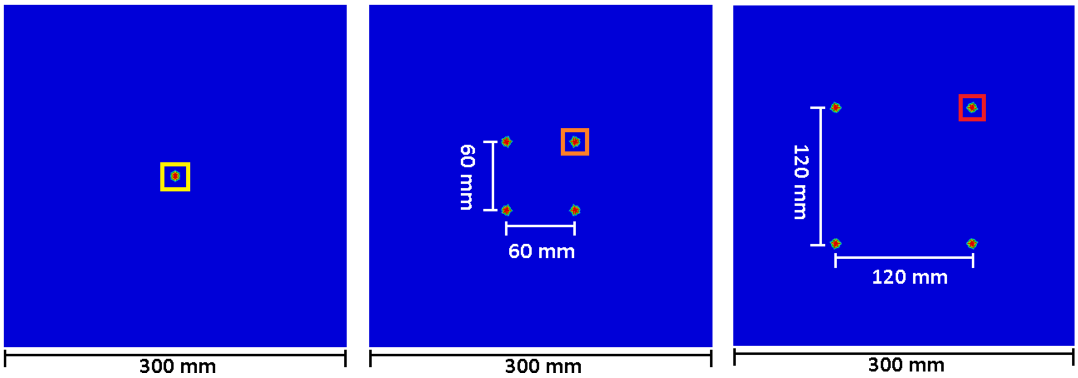

(a) BH1 configuration. **(b)** BH2 configuration. **(c)** BH3 configuration.

Figure 7.2: Depiction of which perforation that was considered for each configuration. (7.2a) The BH1 configuration is marked with yellow, (7.2b) BH2 in orange, and (7.2c) BH3 in red.

7.3 Results

The results presented include, but are not restricted to: damage accumulation plots to assess the difference in damage for the different plate- and meshing configurations, energy plots to validate and assess the simulations and data that are comparable to the experimental data. The damage accumulation plots were visualized using the damage parameter D (denoted SDV_D in Abaqus), which is a normalization of the previously defined parameter SDV_W. Here, fracture is reached when the damage parameter reaches unity.

7.3.1 Normal Impact

Impact Loading

As the perforations not were observed to differ from those presented in Section 6.3, they are subsequently not included in the following. The reader is therefore referred to Figure 6.6.

The total damage accumulated for the three configurations using the different meshing techniques is presented in Figure 7.3 for Docol 600DL and in Figure 7.4 for Docol 1400M. From observations of the figures below, it is observed that the M1 meshing configurations yield a failure-area (indicated by red) which is almost symmetrical about both axes. This is also the case for the BH1 configuration using the M2 meshing configuration but is solemnly due to the mirroring of the quarter plates in Abaqus. Further, it can be observed that the failure-area of the M2 configuration are more arbitrary and not symmetric about either of the axes, which is caused by the arbitrariness of the unstructured mesh. Ballistics is not a symmetrical problem as perforations caused by impacting projectiles or fragments seldom are symmetrical. From this, it consequently follows that the M2 meshing configuration is the most suitable for modelling of ballistics. The energy plots for the simulations were observed to be well within the previously stated recommendations [40], [41], and the conservation of energy plots differed negligibly from constant. These plots are therefore presented in Appendix A.3.1.

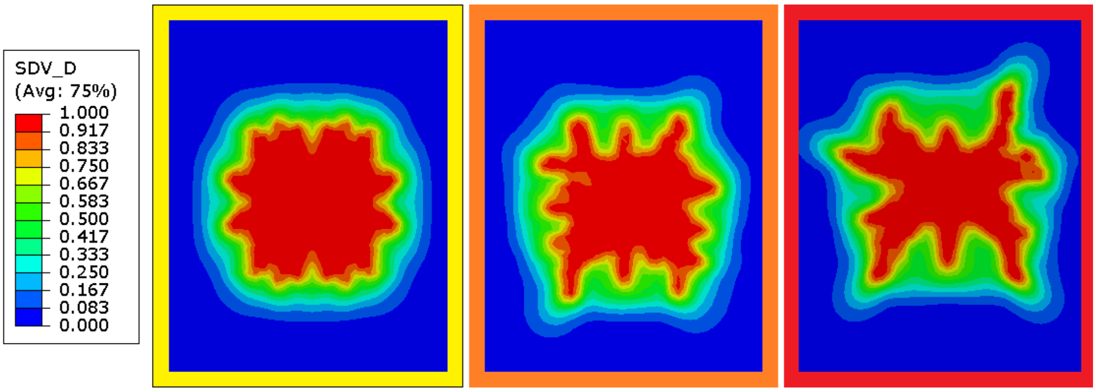

(a) Damage accumulation for configuration BH1 (left), BH2 (center) and BH3 (right) for the M1 mesh configuration using Docol 600DL.

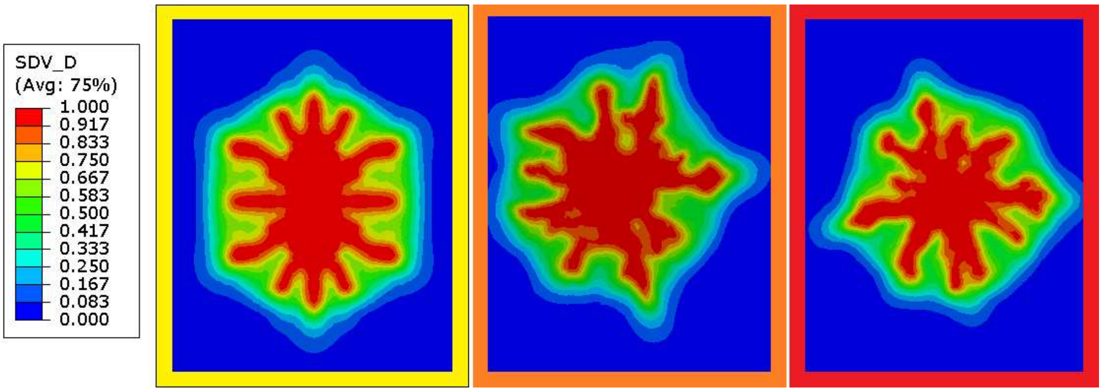

(b) Damage accumulation for configuration BH1 (left), BH2 (center) and BH3 (right) for the M2 mesh configuration using Docol 600DL.

Figure 7.3: Damage accumulation for the different ballistics configuration using meshing configuration M1 and M2 for Docol 600DL. (7.3a) Shows the damage accumulation for M1 and (7.3b) shows for M2. The color-codes correspond to the colors used in Figure 7.2.

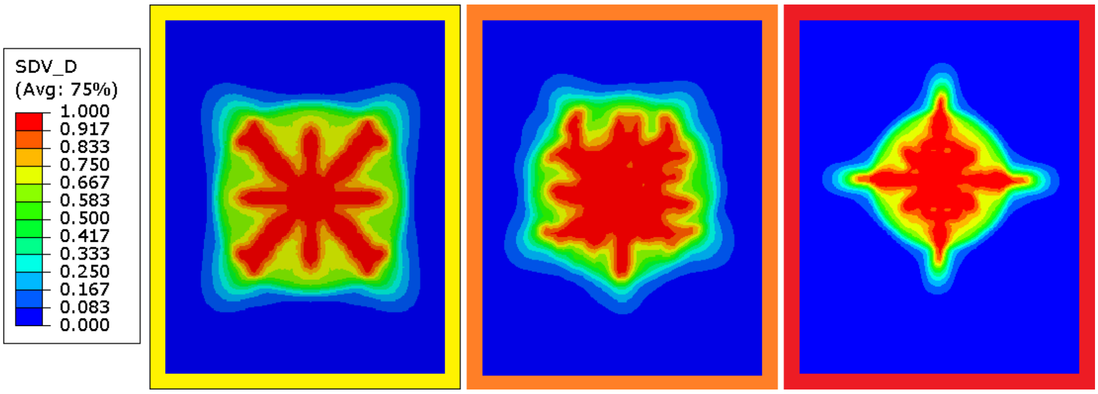

(a) Damage accumulation for configuration BH1 (left), BH2 (center) and BH3 (right) for the M1 mesh configuration using Docol 1400M.

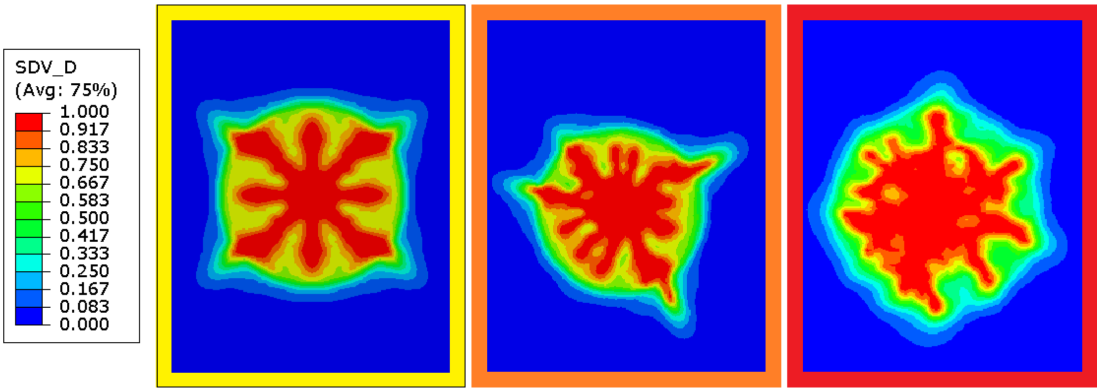

(b) Damage accumulation for configuration BH1 (left), BH2 (center) and BH3 (right) for the M2 mesh configuration using Docol 1400M.

Figure 7.4: Damage accumulation for the different ballistics configuration using meshing configuration M1 and M2 for Docol 1400M. (7.4a) Shows the damage accumulation for M1 and (7.4b) shows for M2. The color-codes correspond to the colors used in Figure 7.2.

Blast Loading

When applying a pressure load in Abaqus, the load is defined as a *follower load* [90], i.e., the load will stay normal to the element faces throughout the analysis. This could, consequently lead to incorrect results. Therefore, simulations were valid until two element faces were perpendicular to each other. Models experiencing fracture are presented in Figure 7.5 for Docol 600DL and in Figure 7.6 for Docol 1400M. From the figures below, it is observed that the plates fail along the yield lines towards the corners.

It is further seen that the crack propagations are highly mesh sensitive, which can be seen from Figure 7.5e and 7.6b. Here, the crack propagates within the finely refined mesh until it reaches the coarser mesh. This resulted in the cracks propagating along the boundary of the fine- and coarse mesh. From Figure 7.6d, 7.6e and 7.6f where the M2 configuration has been utilized, it can be observed that the cracks are freer to propagate without being lead by the mesh.

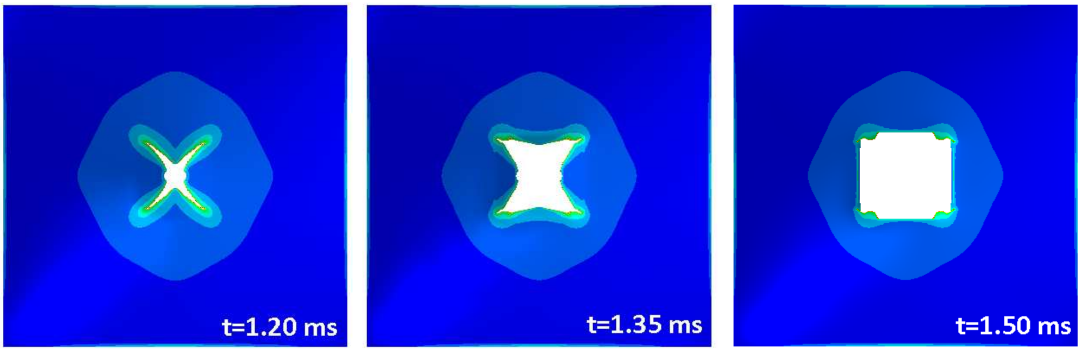

(a) D600_BH1_M1_60 **(b)** D600_BH1_M1_60 **(c)** D600_BH2_M1_60

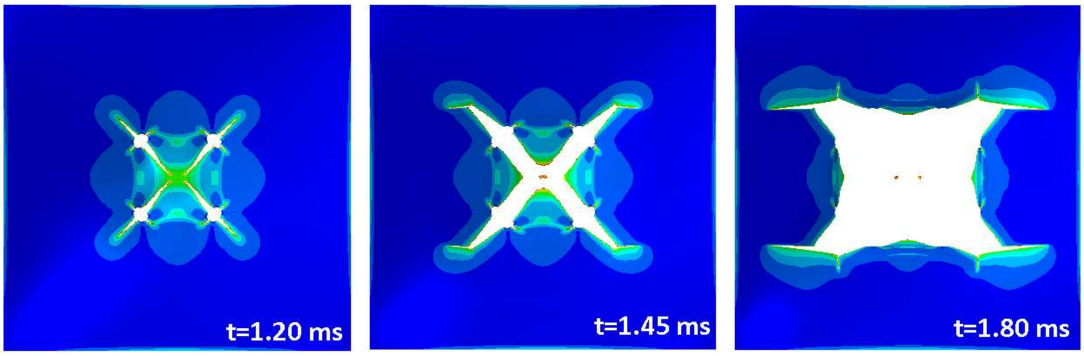

(d) D600_BH2_M1_60 **(e)** D600_BH2_M1_60 **(f)** D600_BH2_M1_60

Figure 7.5: Images taken at three different time-steps depicting the failure modes of the numerical simulations for Docol 600DL.

To further investigate the differences in meshing technique, the damage accumulated at the end of the simulations was plotted. This is presented in Figure 7.7 for Docol 600DL. Docol 1400M only experienced cracking for the BH3 configuration at 60 bar, which is outside the scope of the experimental program. This is, therefore presented in Appendix A.4. From Figure 7.7a, it is observed that the M1 configuration gives failure lines that extend along the yield lines. Whereas the crack propagation for the M2 configuration is somewhat more arbitrary, which can be credited to the unstructured meshing.

Damage accumulation for the M2 configuration is depicted in Figure 7.7b. Due to the high mesh sensitivity of the problem, the fact that ballistic perforations rarely are symmetrical, and the fact that cracks seldom propagate symmetrically, it is evident that the M2 meshing technique is best suited for this thesis. Consequently, all the following simulations were modelled using the M2 meshing configuration.

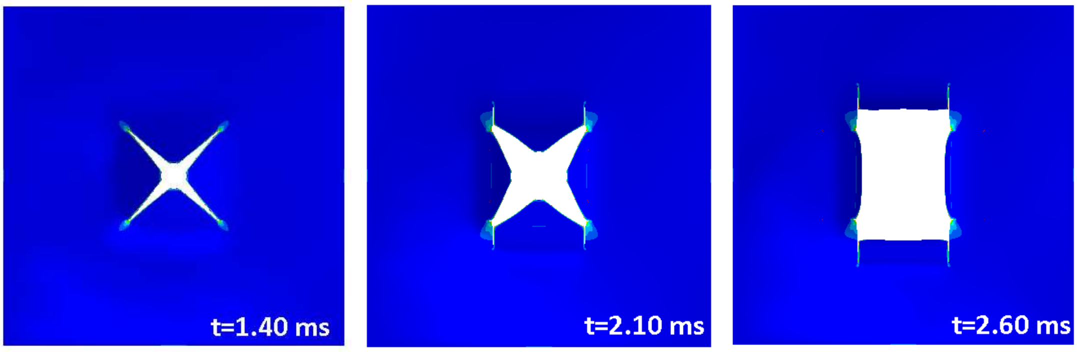

(a) D1400_BH1_M1_25 **(b)** D1400_BH1_M1_25 **(c)** D1400_BH1_M1_25

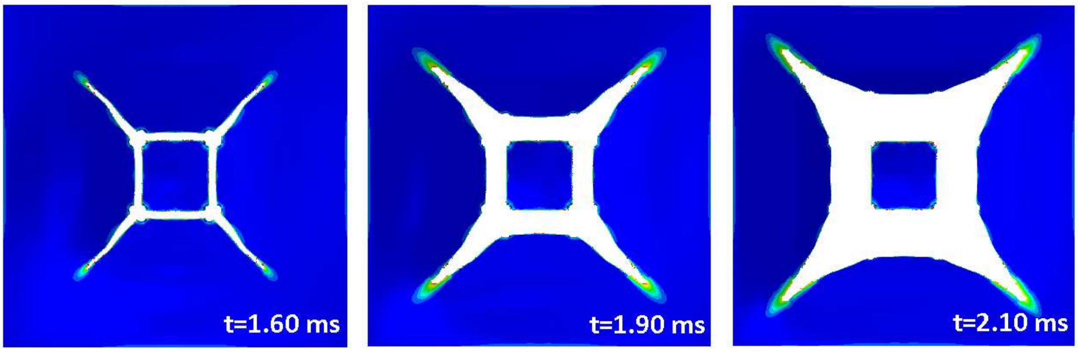

(d) D1400_BH2_M2_35 **(e)** D1400_BH2_M2_35 **(f)** D1400_BH2_M2_35

Figure 7.6: Images taken at three different time-steps depicting the failure modes of the numerical simulations for Docol 1400M.

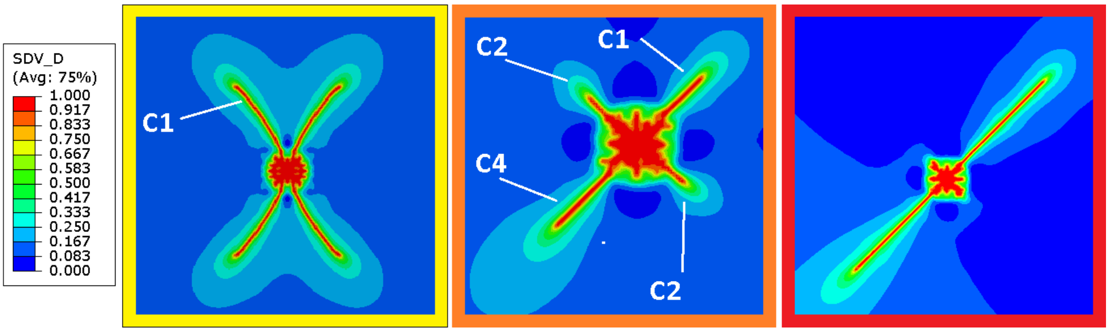

(a) Damage accumulation after blast loading for configuration BH1 at 35 bar (left), BH2 bar 35 bar (center) and BH3 at 60 bar (right) for the M1 mesh configuration using Docol 600DL.

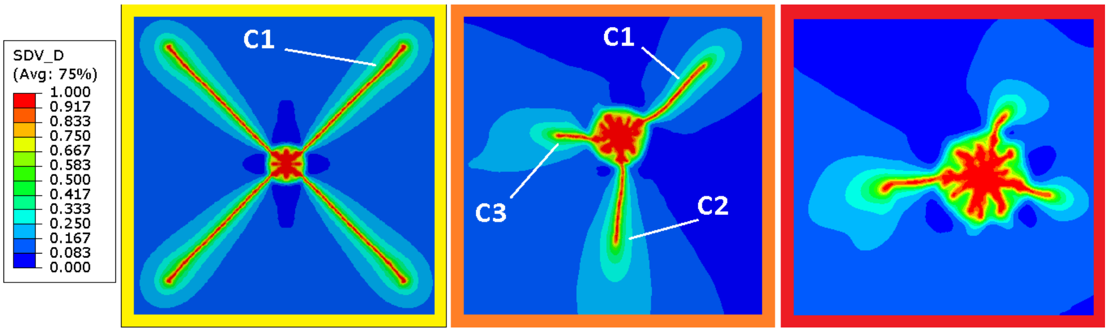

(b) Damage accumulation after blast loading for configuration BH1 at 35 bar (left), BH2 bar 35 bar (center) and BH3 at 60 bar (right) for the M2 mesh configuration using Docol 600DL.

Figure 7.7: Damage accumulation for the different configurations using the different meshing techniques for Docol 600DL after blast loading. (7.7a) Shows the damage accumulation for M1 and (7.7b) shows for M2. The color-codes correspond to the colors used in Figure 7.2.

The displacements have been plotted against the experimental data in Figure 7.8. The experimental data are plotted with dashed lines and marked with "_*Exp*". In addition, the deflection curves from the preliminary study have been plotted to see if they yield an accurate response. This data have been plotted with dotted lines and are marked with "_*prelim*". All displacement histories for simulations outside the experimental test program not experiencing failure are presented in Appendix A.5. The figures below are sorted by material, configuration, and nominal firing pressure. Simulations experiencing fracture that may affect the displacement histories are not included. As aforementioned in Section 5.3.2, the reference time was defined as zero when the incoming pressure passed the sensor closest to the plate. This was subsequently done for the simulations as well.

From the figures below, it is seen that the simulated response of Docol 600DL gives a good approximation to the experimental data. The data in Figure 7.8a should be handled with care as the reference point for both the experimental- and numerical data are taken at a distance from the perforation, as not to be affected by fracture (see Figure 5.19a and 7.1). From observation of Figure 7.8b and 7.8c it is seen that the results from the preliminary study yield a less conservative answer. For Docol 1400M, on the other hand, the simulated response experiences way too heavy oscillations but seems to approach the experimental response as the plate gets damped. As stated in Section 2.6, a purely Lagrangian description should yield a more conservative response since the loading has been overestimated. From the figures below, it is noted that the majority of the simulations are not as conservative as initially expected. This could be due to several factors, with some factors being errors in the extraction of displacement histories from eCorr, boundaries, applying of loads, fluid-structure interaction (FSI) effects and the strain rate sensitivity parameter c.

Granum and Løken (2016) [7] observed that the modelling of the boundaries affected the response of full Docol 600DL plates. They modelled three different levels of the clamping frame. Based on the results, they concluded that a fully clamped assembly yielded the most conservative answer. This was also seen by Aune (2017) [31], who further noticed that the deviations between a fully clamped assembly and a simplified model diminish for plates with square perforations. These observations were also made by Elveli and Iddberg (2018) [11]. Based on this, it can be concluded that simulations using a fully clamped assembly should be conducted in order to assess and evaluate the differences in displacements for this particular load case. Due to the complexity of these models, such analyses are deemed too computationally expensive and consequently considered outside the scope of this thesis.

It is worth noticing that even though the numerical results are close to the experimental results, they should be handled with caution. Aune (2017) [31] observed that the FSI effects played a significant role in the response of the plates, and the plates should thus be examined in a coupled analysis. Based on the numerical findings, Aune concluded that the effects of neglecting FSI and the overestimation of the applied pressure caused a coincidental effect that equalizes the two. Consequently, the results should, therefore, be treated with caution, and fully coupled FSI simulations should be conducted.

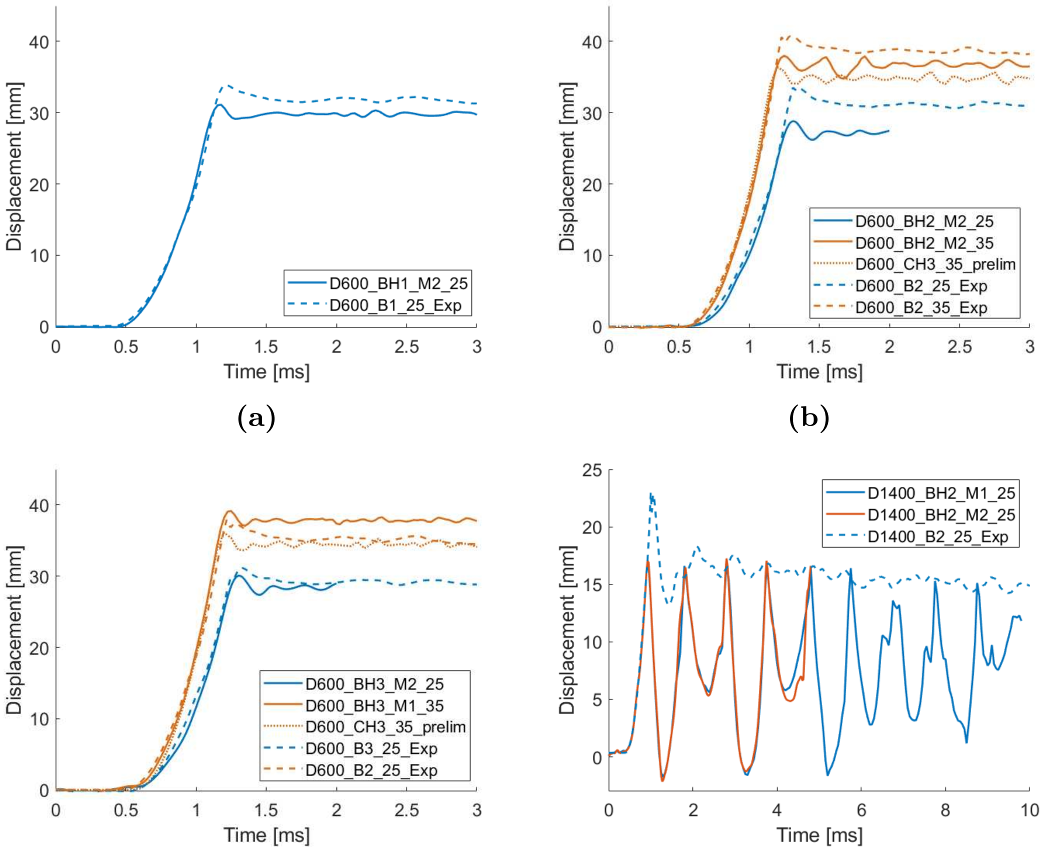

(a)

(b)

(c)

(d)

Figure 7.8: Displacement histories. (7.8a), (7.8b) And (7.8c), shows the histories for Docol 600DL using the BH1, BH3 and BH3 configuration, respectively, and (7.8d) shows the histories for Docol 1400M using the BH2 configuration.

Plots of the ratios of artificial strain energy (ALLAE) divided by the sum of the internal- (ALLIE) and kinetic energy (ALLKE) are presented in Figure 7.9 and 7.10 for Docol 600DL and 1400M, respectively. Here, it is seen that the initial energy ratios are rather high, but drop after approximately 1 ms. For Docol 600DL, the ratios are observed to drop to more acceptable values, whereas the ratios for Docol 1400M are seen to increase further. The reason for a high initial ratio is believed to be linked to how Abaqus conducts restart analyses. Based on this, it was decided to plot the different energies (ETOTAL, ALLIE, ALLKE, and ALLAE) for the ballistics simulations and the first 1.5 ms of the blast simulations. A black dotted line indicates the transition between the two steps. The plot is presented in Figure 7.11.

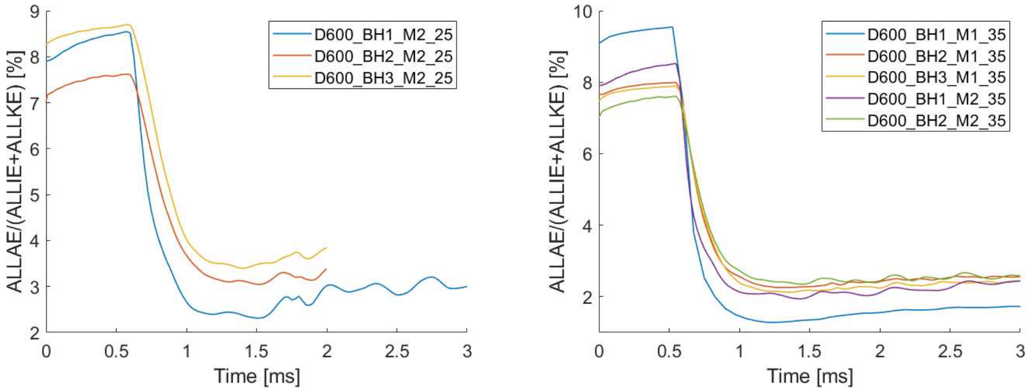

(a) 35 bar

(b) 35 bar

Figure 7.9: Artificial strain energy plots for the blast loading simulations using Docol 600DL at 35 and 60 bar. (7.9a) Shows the artificial strain energy ratio at 25 bar and (7.9b) shows the ratio at 35 bar.

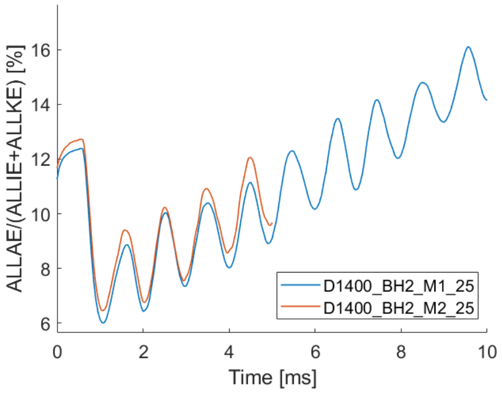

Figure 7.10: Artificial strain energy for Docol 1400M with plate configuration BH2 at 25 bar.

From Figure 7.11a it is seen that the total- and kinetic energy drops drastically after the end of the ballistics simulations. This is due to the fact that the projectiles were prescribed a velocity of zero at the start of blast simulations, which reduced the kinetic energy to approximately zero (there was some kinetic energy in the plate due to propagating stress waves). This is seen in Figure 7.11c. From Figure 7.11b, a slight discontinuity can be observed between the two curves depicting the internal energy.

This is also noticed to a larger extent in Figure 7.11d, which shows the artificial energy. These discontinuities were observed for other simulations as well, with some simulations not exhibiting discontinuities in either of the curves. The artificial- and energy plots across the transition are presented in Appendix A.3 for the remaining simulations. These discontinuities are believed to be linked to how restart analyses are conducted in Abaqus.

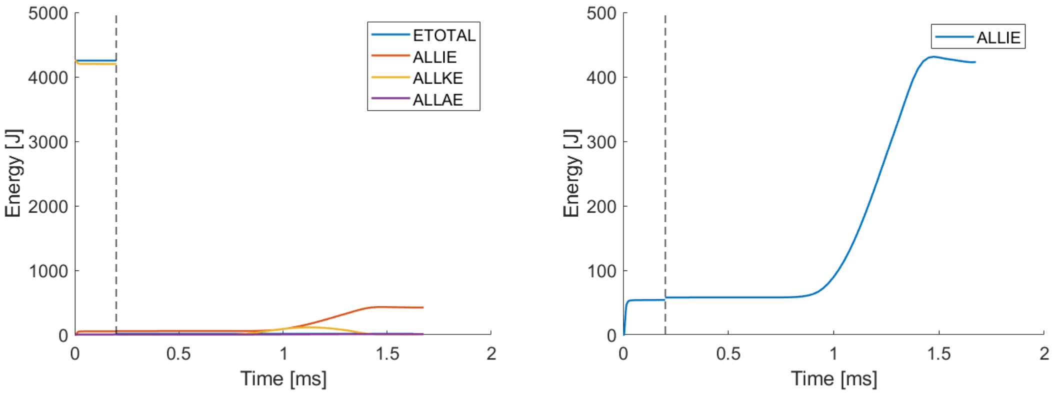

(a) All energies **(b)** Internal energy

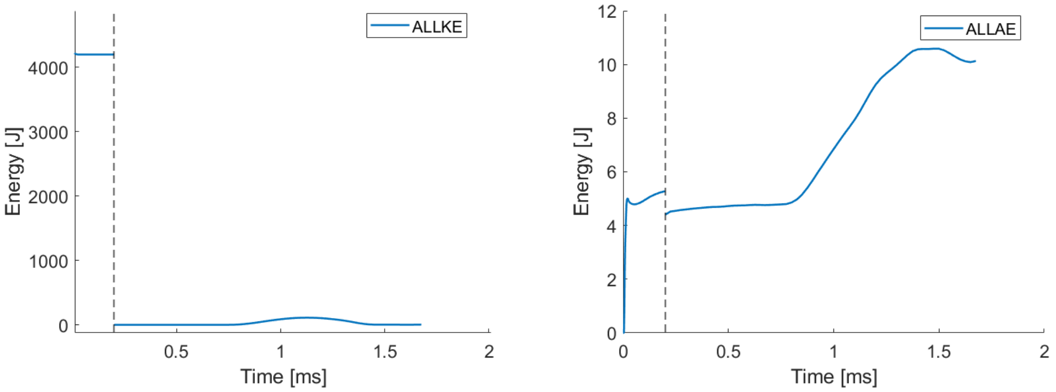

(c) Kinetic energy **(d)** Artificial energy

Figure 7.11: Plot showing different energies in the transition between two steps in a restart analysis in Abaqus for Docol 600DL with plate configuration BH2, meshing technique M2 and a pressure of 35 bar. The different steps are separated by the black dotted line. (7.11a) Shows all interesting energies, (7.11b) shows the internal energy, (7.11c) shows the kinetic energy and (7.11d) shows the artificial strain energy.

The measured crack lengths and maximum deflection for the simulations within the experimental program are presented in Table 7.2. The table is sorted after material, plate configuration, firing pressure, and mesh configuration. For symmetric cracks, only the length of one symmetrical crack has been specified. The cracks are named in a clock-wise manner, with the upper crack being defined as "C1". The name of the cracks is specified in Figure 7.7. The measured crack lengths and maximum deflections for simulations outside the experimental program are presented in Appendix A.4 and A.5, respectively.

Table 7.2: Maximum deflection and measured crack lengths for simulations not experiencing failure. The name of the cracks are specified in Figure 7.7. "X" indicates that the displacements were inaccurate due to cracking.

Simulation	**Maximum Deflection** [mm]	**C1** [mm]	**C2** [mm]	**C3** [mm]
D600_BH1_M2_25	31.11	-	-	-
D600_BH1_M1_35	X	11.89	-	-
D600_BH1_M2_35	X	24.53	-	-
D600_BH2_M2_25	28.81	-	-	-
D600_BH2_M1_35	37.97	4.76	2.20	6.79
D600_BH2_M2_35	37.99	10.90	10.33	4.13
D600_BH3_M2_25	30.06	-	-	-
D600_BH3_M1_35	39.15	-	-	-
D1400_BH2_M1_25	16.85	-	-	-
D1400_BH2_M2_25	17.25	-	-	-

7.3.2 Oblique Impact

All models up until this point have utilized the double-symmetry of the plates. For oblique impact, this simplification was no longer valid, as this would result in projectiles of the upper- and lower halves of the model to have trajectories perpendicular to each other. For the BH1 configuration, two projectiles would impact the same point with 90° between them. This was not consistent with the experimental set-up. Modelling the entire plate proved too computationally expensive. Therefore, half of the plate was modelled, being symmetric about the vertical axis. Due to complex models, simulations were only run with the BH1 configuration.

The same trend was observed in the energy plots for plates experiencing oblique impact as for those experiencing normal impact. Namely, conservation of energy plots differing negligible from constant for all simulations, negligible artificial strain ratios for the ballistics simulations, and the artificial strain energy ratios decreased as a function of time for the blast loading simulations. The energy plots from this section are therefore presented in Appendix A.3.2.

Ballistics

The accumulated damage plotted on the undeformed plate configuration is presented in Figure 7.12 for both materials. These contour plots are observed to correspond to the oblique perforations presented in Section 6.3, and as a consequence of this, the resulting perforations were not presented. The reader is therefore referred to Figure 6.7. As previously discussed, these perforations were observed to be too coarse and have too significant cracking around the "eyelid" to accurately represent the experimental data, which was linked to lack of elements over the thickness.

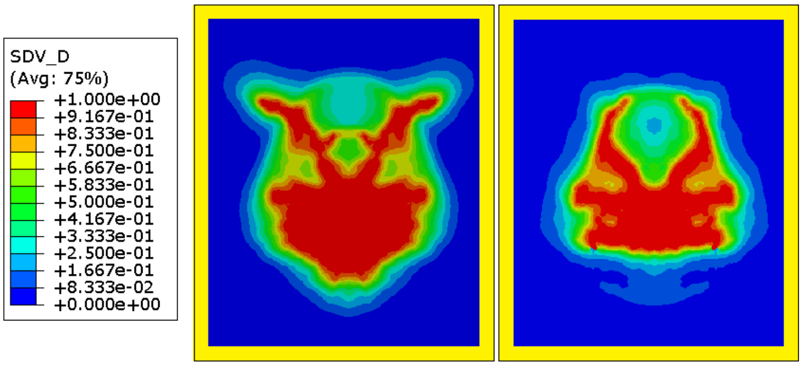

Figure 7.12: Damage accumulation for the BH1 configuration using the M2 meshing technique for Docol 600DL (left) and Docol 1400M (right). The color-code correspond to the colors used in Figure 7.2.

Blast Loading

The simulations were subjected to a pressure of 35 bar for Docol 600DL and 25 bar for Docol 1400M. Both the plates experienced significant cracking, which is presented in Figure 7.13 and 7.14. From the figures, it is seen that the capacity is higher for Docol 600DL. Further, it is observed that the paths of the propagating cracks no longer are symmetrical about both axes. This is consistent with findings from Section 7.3.1. Based on these findings, it can be concluded that the previously established assumption of modelling a quarter-plate [7] or a half-plate, not was entirely valid. For numerical simulations of the combination of impact- and blast loading, the entire plate should, if possible, be modelled. This yields complex and computationally expensive models, and may not be entirely possible. Therefore, the number of symmetry axes should be kept to an absolute minimum. The modelling of perforations on either symmetry axis should be avoided, as this severely limits the arbitrariness of the problem. Due to the fracturing of the plates, the displacement histories are not presented, as this would result in exaggerated displacements.

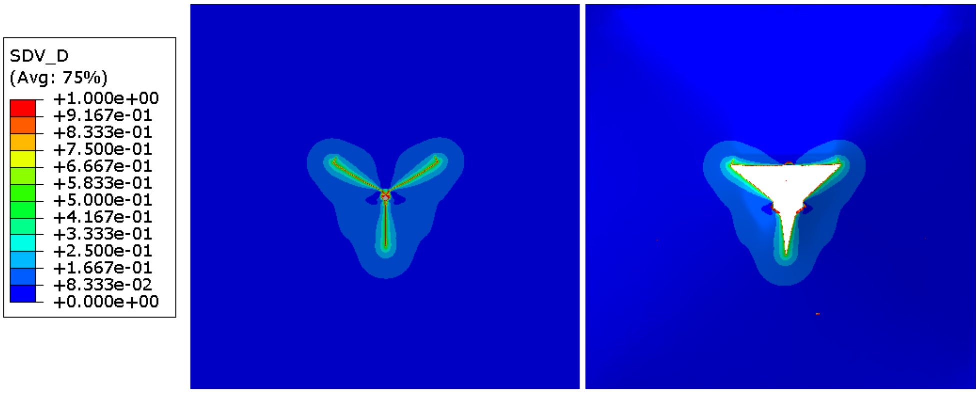

Figure 7.13: Damage accumulation (left) and resulting failure mode (right) for Docol 600DL at 35 bar. Configuration BH1 and M2 meshing technique.

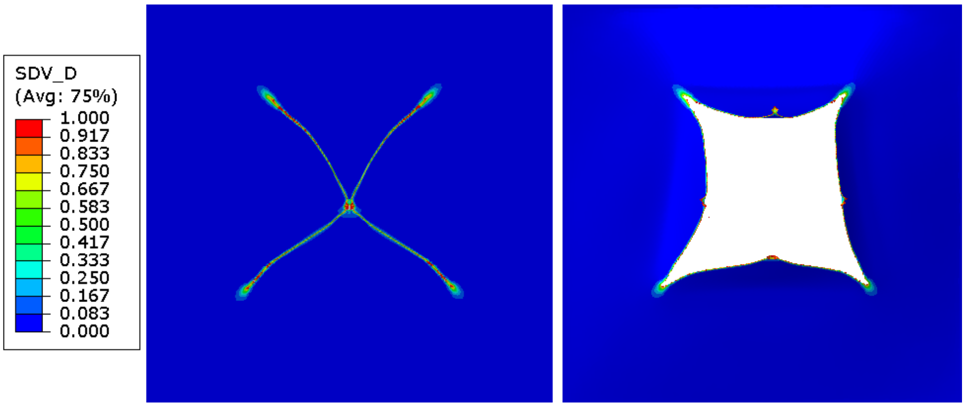

Figure 7.14: Damage accumulation (left) and resulting failure mode (right) for Docol 1400M at 25 bar. Configuration BH1 and M2 meshing technique.

7.3.3 Parametric Study

This study was conducted in order to establish the effect of the Cockcroft-Latham (CL) fracture parameter W_c and the strain rate sensitivity parameter c, as these parameters previously have been observed to affect the structural response for blast loading. As the energy plots of this section deviated negligible from previously presented energy plots, they are presented in Appendix A.3.3.

Cockcroft-Latham Fracture Parameter

The value used for the fracture parameter for both materials was calibrated for shell elements. The fracture parameter should, therefore, be calculated using solid element models with several elements over the thickness. From Section 6.3 it was observed that simulations with six elements over the thickness yielded a very coarse perforation, which was linked to a too low fracture parameter. From this, it was suggested that a higher value should be utilized. Gruben *et al.* (2012) [91] found a CL fracture parameter in the range 722 MPa to 832 MPa by the use of different yield surfaces for 2 mm thick Docol 600DL plates. Motivated by this, a fracture parameter equal to 1.5 and two times the calculated parameter for shell element models (denoted $W_{c,shell}$ in the following), were applied. Simulations were firstly run at normal impact for Docol 600DL with W_c=832.5 MPa and W_c=1110 MPa. Based on these results, it was found that a higher value for the fracture parameter yielded less crack propagation, which was to be expected.

Subsequently, all further simulations were run using W_c=2$W_{c,shell}$, as this gave the most non-conservative response. Simulations for Docol 1400M were run using W_c=1482 MPa. The simulations presented in this section were conducted for the BH1 configuration at both normal- and oblique impact. The difference in residual velocity when increasing the fracture parameter were deemed negligible and was subsequently not presented.

The contour plots of accumulated damage for normal impact with $W_c = W_{c,shell}$ are presented in 7.15 for both materials and served as a basis of comparison. All presented perforations and contour plots of accumulated damage in this study were in the same scale, which made the comparison more trivial.

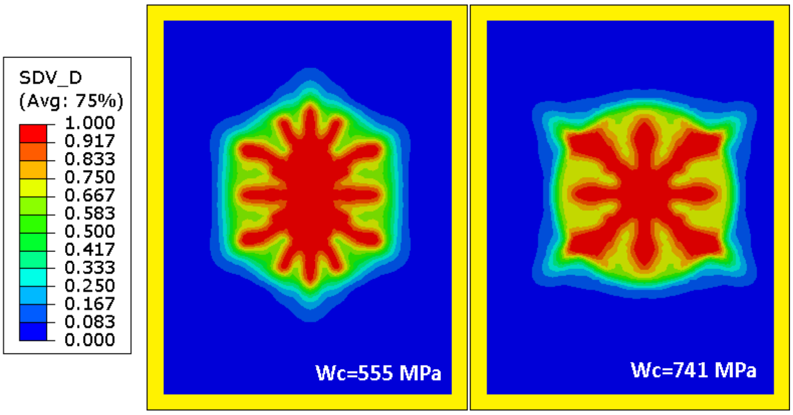

Figure 7.15: Damage accumulation after ballistics using the fracture parameter calculated for shell elements. Docol 600DL with W_c=555 MPa (left) and for Docol 1400M with W_c=741 MPa (right). The color-code correspond to the colors used in Figure 7.2.

The contour plots of accumulated damage and resulting perforations are presented in Figure 7.16 for normal impact. Here, it is seen that the area of accumulated damage gets increasingly more circular. This is due to the cracking caused by ballistics diminishes and the ruptured material gets increasingly more cylindrical. The perforations using $W_c = 2W_{c,shell}$ exhibit no petaling or fringes, yielding a completely smooth perforation. This is questionable when it comes to capturing the failure modes of ballistics, and may be an indication that the fracture parameter was too exaggerated.

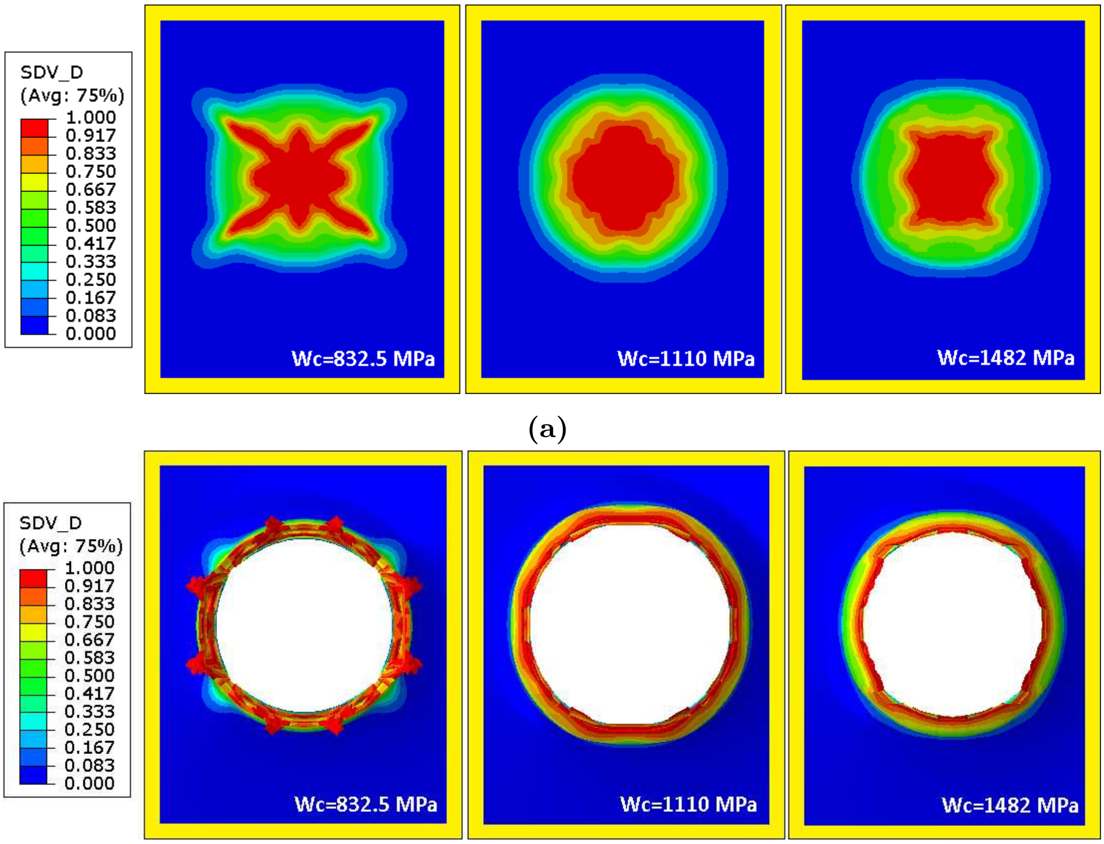

(a)

(b)

Figure 7.16: Damage accumulation for ballistics using plate configuration BH1 and meshing technique M2, for Docol 600DL with W_c=832.5 MPa (left), Docol 600DL with W_c=1100 MPa (center) and Docol 1400M with W_c=1482 MPa. (7.16b) Shows the accumulated damage and (7.16b) shows the resulting perforations. The color-code correspond to the colors used in Figure 7.2.

The resulting perforations for oblique impact are presented in Figure 7.17. From observation, it is noted that the "eyelids" experience a lesser degree of cracking, which is more consistent with the experimental results. The perforations are still observed to be somewhat coarse, which probably can be accredited to the lack of more elements over the thickness. Despite this, it can be concluded that the perforations are a good approximation, and they were deemed adequate for this thesis. From comparison with normal impact, the trend seems to be that oblique impact requires a higher fracture parameter than normal impact.

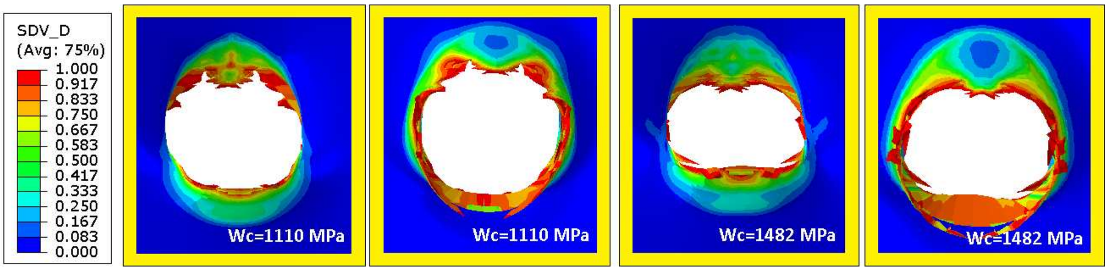

Figure 7.17: Resulting perforations at oblique impact. Entry- (image 1) and exit hole (image 2) for Docol 600DL, and entry- (image 3) and exit hole (image 4) for Docol 1400M. The color-code correspond to the colors used in Figure 7.2.

The simulations experiencing any form of cracking are presented in Figure 7.18. The figures are presented in terms of the entire plate, and a zoom-in on the crack. Also included are the cracks from the experimental work, which has been included for comparison. By comparison of Figure 7.7b and 7.18a, and Figure 7.13 and 7.18c, it is observed that crack propagation paths are independent on the fracture parameter. In addition, it is also seen that cracking diminishes as the fracture parameter is increased.

From Figure 7.18b and 7.18d, the cracking of the two simulations seems to be a good approximation to the experiments. It should be noted that these images are not entirely to scale. By comparison of Table 5.9 and 7.3, it is seen that simulations yielded longer cracks as well as an addition crack. The difference is observed to be maximum 43.3% for D600_BH1_0_15Wc_35 and 64.7% for D600_BH1_45_20Wc_60. Nevertheless, these results can be concluded to be quite consistent with the experimental data. In addition, it can be noted that the trend suggests a higher fracture parameter for oblique impact than for normal impact. This should be further investigated.

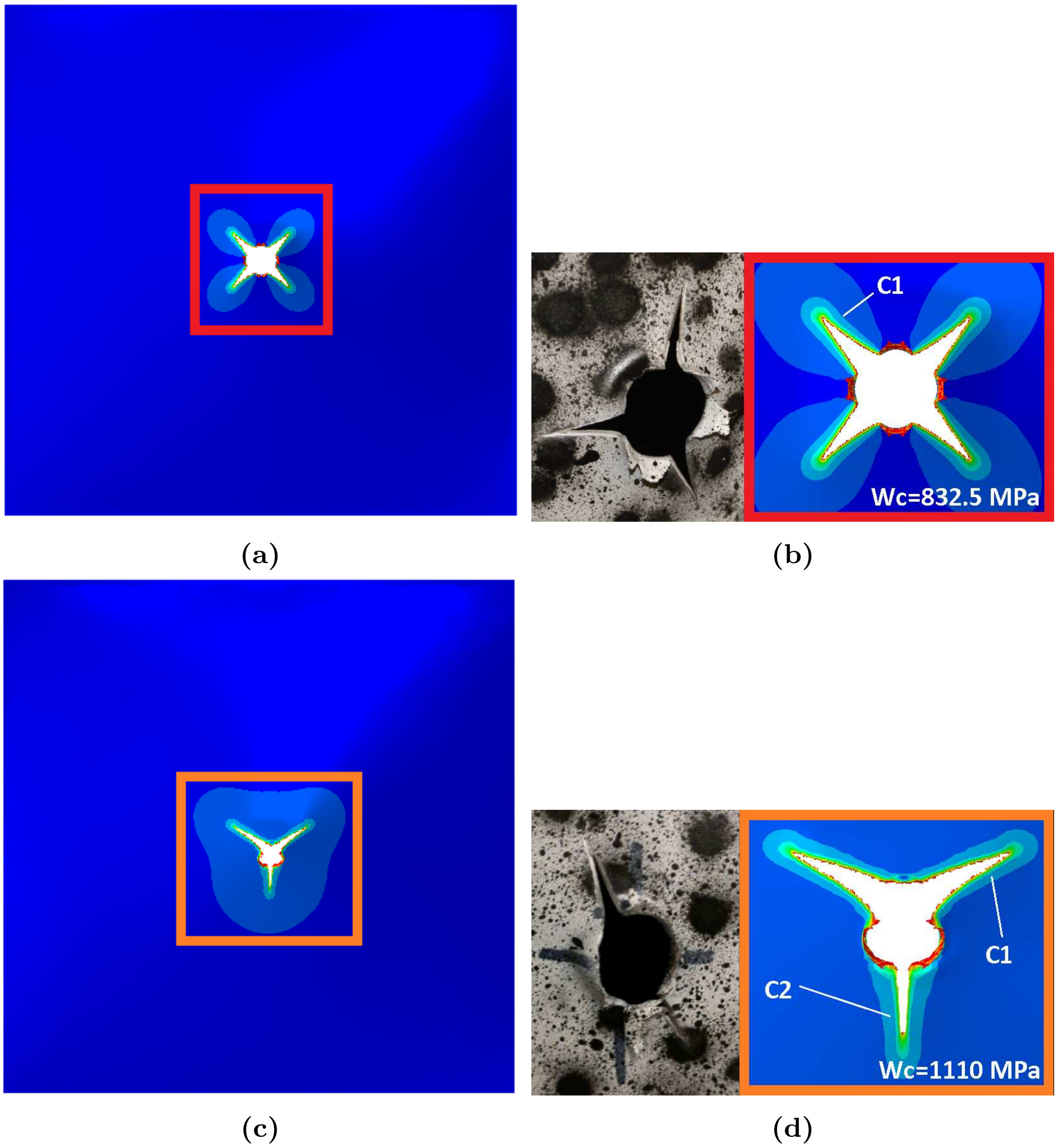

Figure 7.18: Cracking for Docol 600DL, W_c=825.2 MPa for normal impact at 35 bar and W_c=1110 MPa for oblique impact at 60 bar. (7.18a) And (7.18c) shows the entire plate for normal- and oblique impact, respectively, and (7.18b) and (7.18d) shows the experimental cracking (left) and a zoom-in of the numerical cracking (right).

The displacement histories are presented in Figure 7.19 and are plotted against the available experimental data. From Figure 7.19a it is seen that the numerical displacements for both normal- and oblique impact at 35 bar negligibly coincide, which also was observed for the experimental data. Further, these two simulations are noted to be less conservative than the experimental data, which was a trend observed for the majority of simulations in Section 7.3.1. For Docol 1400M, the numerical responses oscillate heavily but are too far away from the experimental data when reaching the peaks of the oscillation. The simulations for Docol 1400M should therefore be run longer, but due to high computational expenses, the run-time had to be reduced. Nevertheless, the simulations give quite accurate displacement histories.

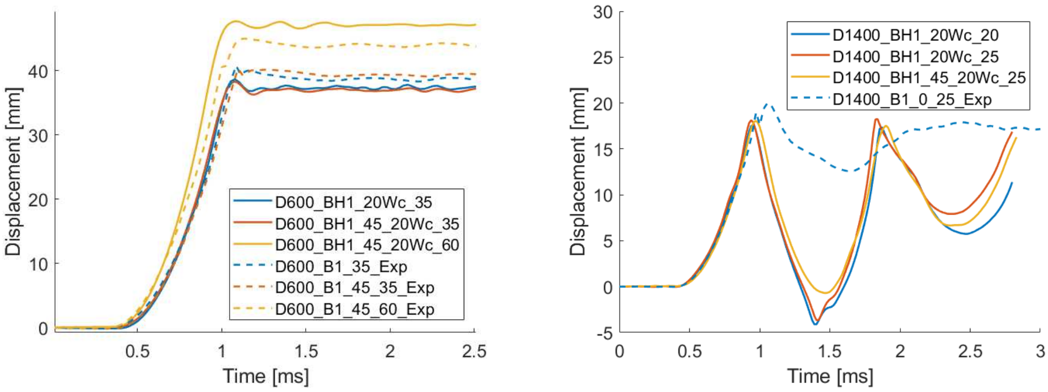

(a) Docol 600DL.

(b) Docol 1400M.

Figure 7.19: Displacement histories using a higher value for the CL fracture parameter. (7.19a) Shows the histories for Docol 600DL using W_c=1100 MPa and (7.19b) shows the histories for Docol 1400M using W_c=1482 MPa.

The measured crack lengths and maximum deflection for the simulations within the experimental program are presented in Table 7.3. The table is sorted after material, firing pressure, impact angle, and fracture parameter. The cracks are named in a clock-wise manner, with the first crack being defined as "C1". The name of the cracks are specified in Figure 7.18b and 7.18d.

Table 7.3: Maximum deflection and measured crack lengths. The name of the cracks are specified in Figure 7.18b and 7.18d. An "X" indicates that the displacement of the reference point were inaccurate due to cracking.

Simulation	**Maximum Deflection** [mm]	**C1** [mm]	**C2** [mm]
D600_BH1_15Wc_35	X	15.27	-
D600_BH1_20Wc_35	38.67	-	-
D600_BH1_45_20Wc_35	38.28	-	-
D600_BH1_45_20Wc_60	47.71	18.59	14.29
D1400_BH1_20Wc_20	17.58	-	-
D1400_BH1_20Wc_25	18.26	-	-
D1400_BH1_45_20Wc_25	18.06	-	-

Strain Rate Sensitivity Parameter

Baglo and Dybvik (2015) [79] conducted a numerical study on the *c*-parameter for continuous Docol 600DL plates with a thickness of 0.8 mm. The results were that a decrease in this parameter leads to an increase in global displacements. This was also observed by Elveli and Iddberg (2018) [11]. Eveli and Iddberg also examined 0.8 mm thick Docol 600DL plates with square perforations using shell element models with an element size of 2 mm. They saw an increase of displacements by 7.59% to 9.75% for the different configurations by changing the strain rate sensitivity parameter from c=0.01 to c=0.001. In addition, a decrease in the parameter was seen to yield a larger extent of crack growth. Motivated by these results, a parametric study was therefore conducted with c=0.001, c=0.004 (only Docol 1400M), c=0.005 (only Docol 600DL) and c=0.01. As previously stated in Section 6.3 changing this parameter has been noted to affect the residual velocity when considering ballistics [87]. The changes in residual velocities were negligible and were subsequently not presented.

The results from the ballistics simulations are presented in Figure 7.20a for Docol 600DL and in Figure 7.21 for Docol 1400M. Presented in each figure is the contour plot of the accumulated damage plotted and the resulting perforations. From the figures, it is seen that the location of the initial cracking changes as the strain rate sensitivity parameter is altered. This can most easily be observed for Docol 1400M in Figure 7.21b. This subsequently leads to different failure modes of the plates, which is noticed in Figure 7.22.

Here, the plates experiencing cracking, which was limited to Docol 600DL plates at 35 bar, are presented. Here, it is seen that a decrease in the strain rate sensitivity parameter leads to an increase in cracking, which is consistent with previous observations [11].

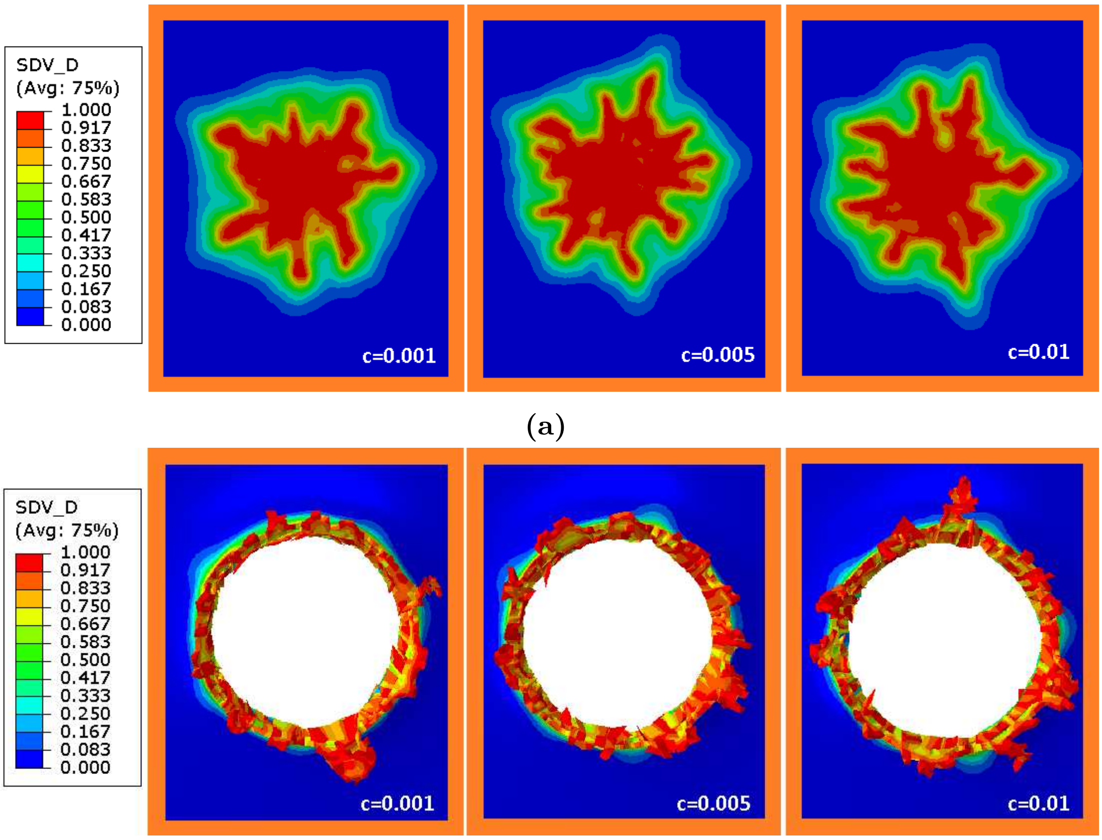

(a)

(b)

Figure 7.20: Damage accumulation for ballistics for Docol 600DL with c=0.001 (left), c=0.005 (center) and c=0.01 (right). (7.20a) Shows the accumulated damage and (7.20b) shows the resulting perforations. The color-code correspond to the colors used in Figure 7.2.

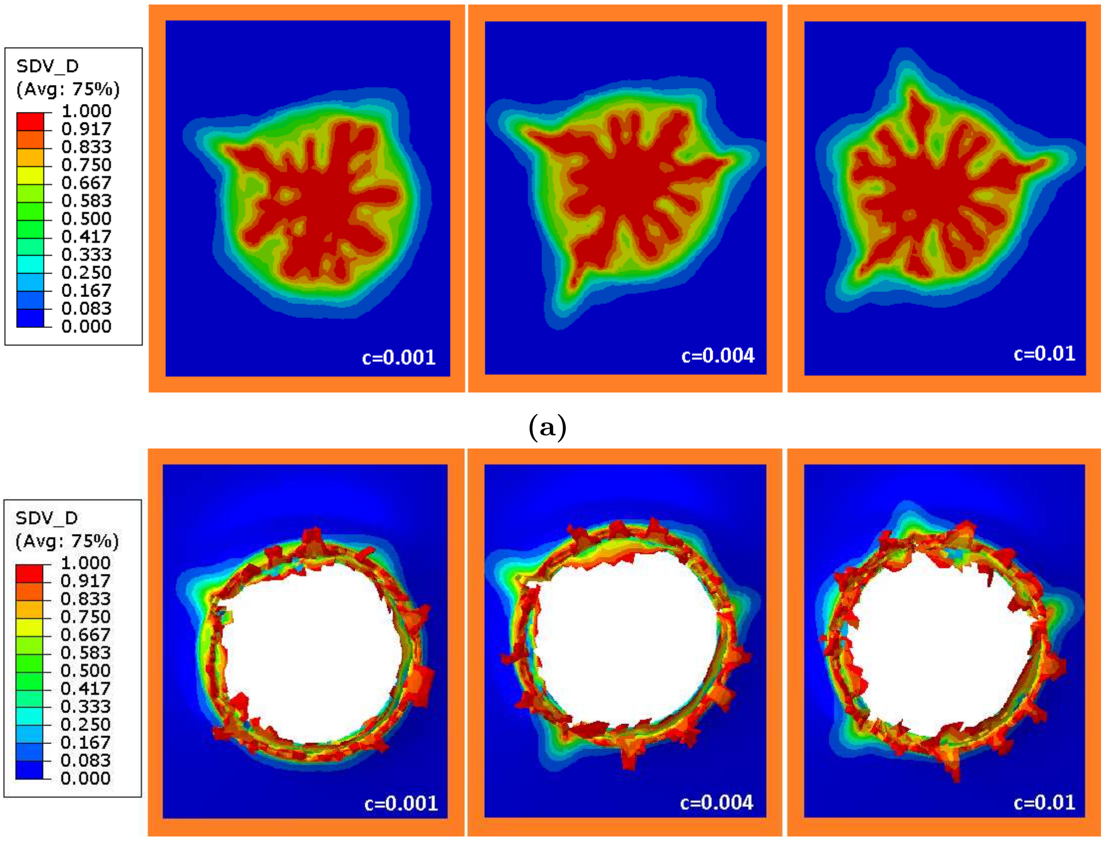

(a)

(b)

Figure 7.21: Damage accumulation for ballistics for Docol 1400M with *c*=0.001 (left), *c*=0.004 (center) and *c*=0.01 (right). (7.21a) Shows the accumulated damage and (7.21b) shows the resulting perforations. The color-code correspond to the colors used in Figure 7.2.

The displacement histories are sorted after material and firing pressure, and presented in Figure 7.23. Here, "X" indicates abortion of D1400_BH2_25_001c due to a power outage. From the figures below, it is readily seen that a lower value for the strain rate sensitivity parameter yields a higher amplitude of deformation for Docol 600DL, which is consistent with previous observations [11], [79]. For Docol 1400M, on the other hand, the displacements are observed to be more in unison throughout the simulations, with slight deviations at the amplitude peaks. These deviations could increase with time, and consequently, simulations should be runt with a longer time.

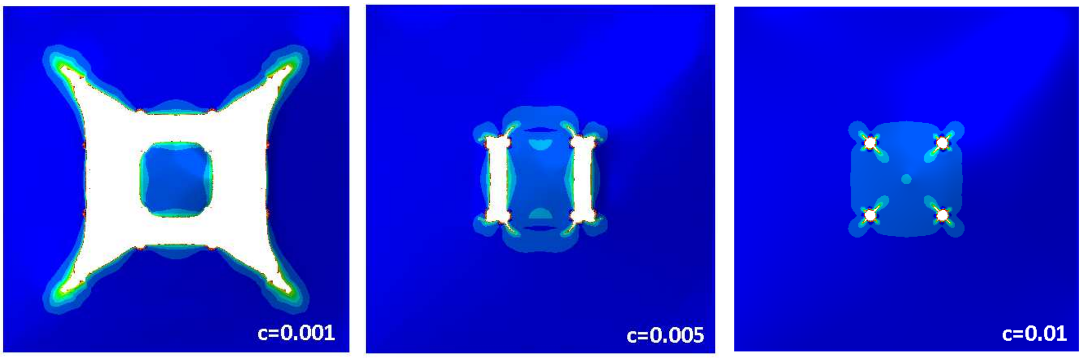

(a) (b) (c)

Figure 7.22: Cracking caused by blast loading for Docol 600DL using the BH2 configuration with different values for the strain rate sensitivity parameter c at 35 bar. (7.22a) Shows the entire plate for c=0.001, (7.22b) for c=0.005 and (7.22c) for c=0.01.

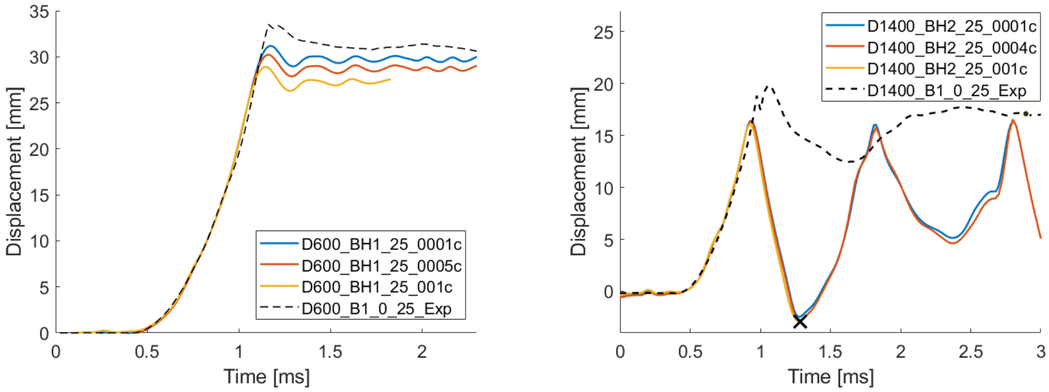

(a) (b)

Figure 7.23: Deflection histories using the BH2 configuration for both materials. (7.23a) Shows Docol 600DL at 25 bar and (7.23b) shows Docol 1400M at 25 bar. The "X" indicates abortion of the simulation due to a power outage.

Rakvåg *et al.* (2013) [6] examined the strain rate sensitivity of Docol 600DL by conduction split Hopkins tests on 0.7 mm thick plate material. From this, it was concluded that the strain rate sensitivity parameter is dependent on the level of plastic strain. The modified Johnson-Cook criterion was then fitted to the experimental data for plastic strain levels of 5%, 8% and 12%, which consequently lead to three different values for the strain rate sensitivity parameter.

Based on this, it was decided to check the levels of plastic straining for both materials. The plastic strain was visualized as a contour plot on the undeformed configurations. As the Docol 600DL plates at 35 bar experienced cracking, they were not included. The contour plots of the plastic strain are presented in Figure 7.24 and 7.25 for Docol 600DL and 1400M, respectively. For Docol 1400M, the levels of plastic strains were observed to develop as the material oscillated; therefore, the plots were presented at the time of maximum deflection. From the figures below, it is noted that the magnitude of plastic strain is 72% greater for Docol 600DL, which is linked to ductility. It is further seen that the levels of plastic strain increase as the strain rate sensitivity parameter is decreased for both materials. This is consistent with observations by Rakvåg *et al.* (2013) [6]. The increase in plastic strain may explain why a decrease of c yields higher global deflection for Docol 600DL, and simulations should be run longer to see if this also it the case for Docol 1400M.

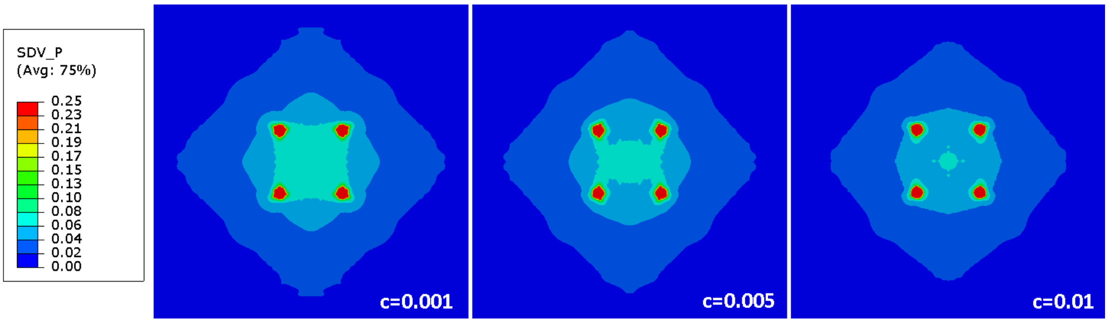

Figure 7.24: Levels of plastic straining for different c-values for Docol 600DL.

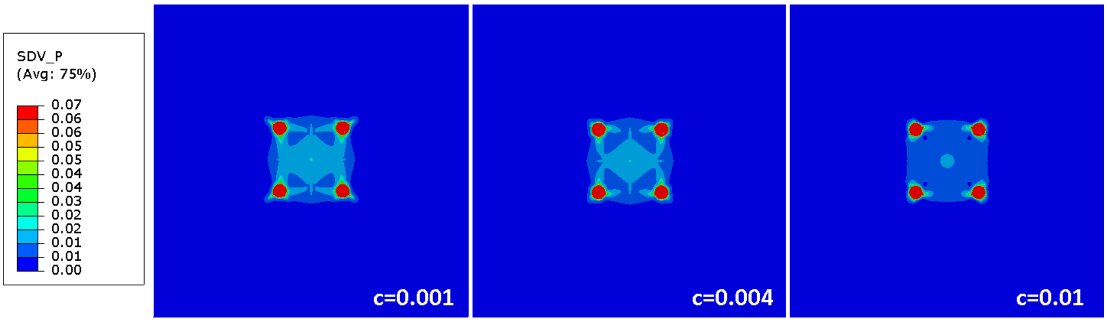

Figure 7.25: Levels of plastic straining for different c-values for Docol 1400M.

7.4 Concluding Remarks

When evaluating numerical results, it is imperative to be critical as there exists several assumptions, simplifications, and uncertainties that, in turn, may cause potential inaccuracies. The modelling of both the ballistics and blast loading proved to be somewhat challenging, and the models were consequently based on a series of simplifications. With a select few being the reduction of elements over the thickness, the representation of boundary conditions and the neglecting of FSI effects. In addition, these models proved to be rather complex, which in turn resulted in run-times of well over 100 hours for some of the simulations. From this, it follows that further simplifications should be made, and techniques should be adopted in order to decrease the complexity further.

From the numerical results, it was seen that an unstructured mesh was the most beneficial when modelling the combination of impact- and blast loading. This was linked to the fact that ballistics yield unique perforations which are not entirely symmetrical in the majority of cases. These perforations were further noted to influence the path of crack propagation, which may be non-symmetrical as well. It was further observed and concluded that the number of symmetry lines, i.e., number of times the model has been mirrored, should be kept to an absolute minimum as this severely affected the ballistic perforations and crack propagation.

From the parametric study, it was seen that both the investigated parameters significantly affected the results. It was concluded that a higher fracture parameter should be selected for both materials as this diminished the extent of forming cracks. In addition, it was noticed a trend that plates experiencing oblique- contra normal impact should utilize a higher fracture parameter. With the adjustment of this parameter, the numerical results were observed to be in quite good agreement with the experimental results. The reduction of the strain rate sensitivity parameter gave a softer response of the material as well as more crack growth for Docol 600DL, which was consistent with observations made by Elveli and Iddberg (2018) [11]. For both materials, this parameter was also perceived to be dependent on the level of plastic straining, which was consistent with observations made for Docol 600DL [6].

Chapter 8

Discussion

For the ballistics experiments, it was seen that both materials exhibited petaling, although the extent of cracking formed around the perforations differed to some degree. It was observed that Docol 1400M experienced more prominent cracking. This was linked to Docol 1400M having a higher strength, and lower ductility and strain hardenability than Docol 600DL. For these experiments, at such high impact velocity and for a plate thickness of 0.8 mm, the results differed negligibly between materials and individual experiments. So, the choice of material for ballistic loading in this thesis can be considered indifferent. Nevertheless, Børvik *et al.* (2009) [28] concluded that the ballistic limit velocity of a target is linearly dependent on the yield strength of the material. As the yield strength of Docol 1400M is approximately 75.6% greater than that of Docol 600DL, it subsequently follows that Docol 1400M is the most suitable material when considering pure impact.

For the blast loading experiments it was noted that the capacity of the two materials differed significantly, with Docol 600DL having the highest capacity with respect to fracture. The difference in capacity was also shown numerically, both in the preliminary- and in the final numerical study. This was linked to the ferrite-content of the material, which yields higher ductility and strain hardenability. The Docol 1400M were observed to exhibit excessive cracking, which developed and propagated as the material oscillated. The oscillations subsequently increased plastic straining, which due to the poor strain hardenability of the material, induced further crack growth. From this, it consequently follows that excessive cracking severely reduces the overall capacity of the structure.

The numerical displacement histories for Docol 600DL were seen to be in good agreement with the experimental data, which was accredited to previous validation of the model parameters. Docol 1400M was observed to exhibit exaggerated oscillations, which increased as the pressure decreased. This may consequently be caused by factors such as the elastic rebound, propagating stress waves, and simplified boundaries. As previously stated, the model parameters for Docol 1400M had been calibrated for a plate thickness of 1 mm. As this may cause an additional source of error, these parameters should be calibrated for a thickness of 0.8 mm, and be further validated through comparison with experimental work. This highlights the importance of validated models, which is important when conducting simulations.

Experimentally, it was remarked that the initial cracking of the perforations was seen to lead to propagating cracks. This observation is consistent with previously conducted research on perforated plates, were it has been noted that cracking originate from pre-formed slits and corners of square perforations [7], [8], [9], [10], [11], [13]. Thus, it can be concluded that initial cracking and sharp edges are a detrimental factor when considering blast loading. From this observation it consequently follows that pre-formed circular holes may not be valid substitutes for fragment- or impact loading, as have been tested by Rakvåg *et al.* (2013) [6] and Li *et al.* [10].

The cracking of the simulations was observed to rather poorly predict that of the experimental data, which was accredited to the Cockcroft-Latham fracture parameter. The value utilized through the entirety of the thesis was calibrated for shell element models. A parametric study was therefore conducted on this parameter, where the results showed that it has to be increased. Increasing the parameter subsequently yielded cracking closer to the experimental data, with a maximum total difference of 64.7%.

A parametric study was further conducted on the strain rate sensitivity parameter, and the obtained showed that a decrease of this parameter for Docol 600DL resulted in a softer response, which was previously seen by Baglo and Dybvik [79], and Elveli and Iddberg [11]. In addition, the parameter was shown to be dependent on the level of plastic straining, which reflects the strain hardenability of the material, which is consistent with work by Rakvåg [6].

The major obstacle for the numerical work was to combine the numerical assumptions for both impact- and blast loading with satisfying results. This consequently resulted in high complexity and computational time for the established models, with run-times of well over 100 hours for several simulations. Subsequently, it would be beneficial to use simplified models as this would reduce the overall complexity and computational run-times significantly.

From observations made in this thesis, both experimentally and numerically, it is evident that the synergistic effects of combined impact- and blast loading cannot be neglected, or simplified to a too large extent. This corresponds well with the findings of previous work [15], [16], [19], [20]. This consequently leads to more tedious work but results in better insight, knowledge, and comprehension of the threat at hand. As little work exists on the combination of ballistics and blast loading, these results are significant but incomplete. A series of new experiments, as well as replication experiments, should be conducted to expand the underlying experimental database, and increase the general knowledge of this field.

In a world where the need for protective structures has increased within the last year, it consequently follows that reliable structures are needed. From the results of this thesis, it was recognized that the strength and hardness of a material not always are the most beneficial properties. As blast loading is a highly global structural problem, it may consequently lead to large deformations and moderate strains. Thus, it can be concluded that the most reliable choice is to select a material that, in addition to strength, is ductile and possesses good strain hardenability. Nevertheless, this claim should be further and more thoroughly tested, as the underlying experimental database was somewhat scarce.

Chapter 9

Conclusions

This chapter will briefly conclude on the most important findings obtained through the work on this thesis. The main objectives of this thesis were to determine how thin steel plates of different steel grades behaved under combined impact- and blast loading and to validate to which extent this could be predicted numerically.

After conducting the experimental- and numerical work of this thesis, the following can be concluded:

- Initial cracking formed by the ballistics experiments were seen to lead the path of crack propagations. This was also observed to some degree numerically.
- Ductility and strain hardening are essential material properties when considering this particular load case.
- The experiments in the SSTF served as a great tool for validating the numerical models in the final numerical study.
- Numerical modelling of the combination of impact- and blast loading is a highly non-symmetric problem. Modelling of full plates should therefore be considered.
- The major obstacle for the numerical work was to combine the assumptions for both load cases with satisfying results, which resulted in high complexity of the models. It would be very beneficial to use simplified models that further reduce the overall complexity.

- The calibrated model parameters and constitutive relations for describing each separate material were noted to be in good agreement for Docol 600DL. This was observed for Docol 1400M as well, despite the spurious oscillations of the material.
- Increase of the Cockcroft-Latham fracture parameter was seen to significantly decrease the forming cracks, resulting in results closer to the experimental data. Crack propagations were seen to be independent of this parameter. Trends showed that this parameter should be higher for oblique impact.
- Changes in the strain rate sensitivity parameter affected the stiffness, capacity, and failure modes observed for the numerical models.

Chapter 10

Suggestion to Further Work

From the experimental results, it was observed that the initial cracking around the perforations was seen to lead the propagating cracks. Based on this, it would be interesting to see if one can control the direction of the cracks by conducting experiments with pre-formed circular holes with notches and to see if this can be recreated numerically as well.

The Docol 1400M plates that experienced crack arrest were seen to have significant crack development along the vertical axis when mounted in the shock tube,i.e., along the rolling direction of the material. As concluded in Section 3.4, steel plates get increasingly more anisotropic as the thickness decreases. Thus it would be interesting to conduct a series of experiments similar to those in this thesis with horizontal rolling direction instead, to see if the difference in results is significant.

The scarcity of available Docol 1400M plates lead to some configurations being omitted. Therefore it would be beneficial to conduct more experiments on this material. It would also be interesting to examine different ballistics configurations for both materials, with different perforation patterns and perforations outside the yield lines, and closer to the boundaries. Crack propagation was observed to be dependent on the failure mode as well as the impact angle; consequently, it would be exciting to conduct tests using different projectile-nose shapes, fired at different angles and with different initial velocities, ranging from near the ballistic limit to an ordnance velocity regime. In addition, it would be interesting to conduct the tests mentioned above at plates with different thicknesses as well.

In the experimental work, it was observed that ductility and strain hardenability were more critical for the blast resistance of the plates than material strength. Therefore, it would be interesting to conduct similar experiments as those mentioned above on other materials with different strength, strain hardenability, and ductility. Such experiments would be very beneficial as it further investigates the claims made in this thesis, as well as maps if other materials are more suitable as protective structures. It further broadens the experimental database, and more knowledge is acquired.

From the numerical study in Chapter 7, it was established that altering the CL fracture parameter W_c as well as the strain rate sensitivity parameter c had a significant effect on the structural response. In light of this, the fracture parameter should be accurately calculated for three elements over the thickness using solid elements. A parametric study should be conducted for c combined with the calibrated values for W_c. In addition, the effects of both parameters should be accurately studied using a fully clamped assembly model instead of simplified boundary conditions. It was also stated in Section 7.3.1, that neglecting the FSI effects, using a simplified model and a purely Lagrangian approach, gave numerical results that coincidental appeared to be a close approximation of the experimental results. It would therefore be interesting and very beneficial to use another FEM-code like EUROPLEXUS [12] to model the different configurations with included FSI effects.

Bibliography

[1] S. Mannan, *Lees' Loss Prevention in the Process Industries.* Elsevier Butterworth-Heinemann, fourth edition, 2012.

[2] Wikipedia, "Deepwater Horizon explosion." `https://en.wikipedia.org/wiki/Deepwater_Horizon_explosion`, December 2018. Accessed on 15-01-2019.

[3] Institute for Economics and Peace, "Global Terrorism Index 2018." `http://globalterrorismindex.org/`, 2018. Accessed on 23-04-2019.

[4] R. W. Guerney, "The initial velocities of fragments from bombs, shell, and grenades," *Ballistics Research Laboratories: BRL Report No. 405*, 1943.

[5] SAGE Publishing, "International Journal of Protective Structures." `https://uk.sagepub.com/en-gb/eur/international-journal-of-protective-structures/journal202501`, 2019. Accessed on 21-05-2019.

[6] K. G. Rakvåg, N. J. Underwood, G. K. Schleyer, T. Børvik, and O. S. Hopperstad, "Transient pressure loading of clamped metallic plates with pre-formed holes," *International Journal of Impact Engineering, Volume 53: 44-55*, 2013.

[7] H. M. Granum and L. M. Løken, "Master thesis: Experimental and numerical study on perforated steel plates subjected to blast loading," 2016.

[8] V. Aune, G. Valsamos, F. Casadei, M. Langseth, and T. Børvik, "On the dynamic response of blast-loaded steel plates with and without pre-formed holes," *International Journal of Impact Engineering, Volume 108: 27-46*, 2017.

[9] S. Thorgeirsson and J. Stensjøen, “Master thesis: An experimental and numerical investigation of the blast response of pre-damaged aluminium plates,” 2017.

[10] Y. Li, W. Wu, H. Zhu, Z. Wu, and Z. Du, “The influence of different preformed holes on the dynamic response of square plates under air-blast loading,” *Engineering Failure Analysis, Volume 78: 122-133*, 2017.

[11] B. Elveli and M. Iddberg, “Master thesis: Experimental and numerical study on perforated steel plates subjected to blast loading,” 2018.

[12] EPX, “Europlexus.” `http://www-epx.cea.fr/`, 2019. Accessed on 25-05-2019.

[13] H. M. Granum, V. Aune, T. Børvik, and O. S. Hopperstad, “Effect of geometry and heat-treatment on the structural response of blast-loaded aluminium plates with pre-cut slits (unpublished paper),” 2019.

[14] P. D. Linz, S. Fan, and C. Lee, “Modeling of combined impact and blast loading on reinforced concrete slabs,” *Latin American Journal of Solids and Structures, Volume 13(12): 2266-2282*, 2016.

[15] H. Y. Grisario and A. V. Dacygier, “Characteristics of combined blast and fragments loading,” *International Journal of Impact Engineering, Volume 116:51-64*, 2018.

[16] K. Osnes, O. S. S. Dey, Hopperstad, and T. Børvik, “On the dynamic response of laminated glass exposed to impact before blast loading,” *Experimental Mechanics: 1-14*, 2019.

[17] C. Y. Ma and J. Y. R. Liew, “Blast and ballistic resistance of ultra-high strength steel,” *International Journal of Protective Structures, Volume 4(3): 379-413*, 2013.

[18] ThyssenKrupp, “XAR-450 material specifications.” `https://www.thyssenkrupp-steel.com/media/content_1/publikationen/grobblech_migration/xar/werkstoffblaetter_6/xar_450_en.pdf`, September 2017. Accessed on 25-04-2019.

[19] K. A. Marchand, M. M. Vargas, and J. D. Nixon, “The synergistic effects of combined blast and fragment loadings,” *AIR FORCE ENGINEERING SERVICES CENTER*, 1992.

[20] X. Kong, W. Wu, J. Li, P. Chen, and F. Liu, “Experimental and numerical investigation on a multi-layer protective structure under the synergistic effect of blast and fragment loadings,” *International Journal of Impact Engineering, Volume 65: 146-162*, 2013.

[21] ANSYS Inc., “ANSYS Autodyn.” `https://www.ansys.com/products/structures/ansys-autodyn`, 2019. Accessed on 16-05-2019.

[22] H. Ebrahimi, R. Ghosh, E. Mahdi, H. Nayeb-Hashimi, and A. Vaziri, “Honeycomb sandwich panels subjected to combined shock and projectile impact,” *International Journal of Impact Engineering, Volume 95:1-11*, 2016.

[23] T. Børvik, O. S. Hopperstad, and M. Langseth, “An introduction to penetration and perforation mechanics,” 2016.

[24] J. A. Zukas, *Impact Dynamics*. John Wiley and Son, 1982.

[25] M. E. Backman and W. Goldsmith, “The mechanics of penetration of projectiles into targets,” *International Journal of Engineering Science, Volume 16(1): 1-99*, 1978.

[26] Wikipedia, “Ballistic limit.” `https://en.wikipedia.org/wiki/Ballistic_limit`, October 2017. Accessed on 25-04-2019.

[27] T. Børvik, M. Langseth, O. S. Hopperstad, and K. A. Malo, “Perforation of 12 mm thick steel plates by 20 mm diameter projectiles with flat, hemispherical and conical noses: Part i: Experimental study,” *International Journal of Impact Engineering, Volume 27(1): 19-35*, 2002.

[28] T. Børvik, S. Dey, and A. H. Clausen, “Perforation resistance of five different high-strength steel plates subjected to small-arms projectiles,” *International Journal of Impact Engineering, Volume 36(7): 948–964*, 2009.

[29] V. Aune, T. Børvik, and M. Langseth, “An introduction to blast mechanics,” 2016.

[30] Wikipedia, “Shock wave.” `https://en.wikipedia.org/wiki/Shock_wave`, April 2019. Accessed on 26-04-2019.

[31] V. Aune, “PhD Thesis: Behaviour and modelling of flexible structures subjected to blast loading,”

[32] Wikipedia, “Ideal gas law.” `https://en.wikipedia.org/wiki/Ideal_gas_law`, April 2019. Accessed on 11-05-2019.

[33] W. J. M. Rankine, “On the thermodynamic theory of waves of finite longitudinal disturbance,” *Philosophical Transactions of the Royal Society London, Volume 160: 277-286*, 1870a.

[34] W. J. M. Rankine, “On the thermodynamic theory of waves of finite longitudinal disturbance,” *Philosophical Transactions of the Royal Society London, Volume 160: 287-288*, 1870b.

[35] P. Hugoniot, “Mémoire sur la propagation du mouvement dans les corps et ples spécialement dans les gaz parfaits, 1 e partie,” *Journal de l’École Polytechnique Paris, Volume 57: 3-97*, 1887.

[36] P. H. Hugoniot, “Mémoire sur la propagation du mouvement dans les corps et ples spécialement dans les gaz parfaits, 2 e partie,” *Journal de l’École Polytechnique Paris, Volume 58: 3-125*, 1889.

[37] V. Aune, E. Fagerholt, M. Langseth, and T. Børvik, “A shock tube facility to generate blast loading on structures,” *International Journal of Protective Structures, Volume 7(3): 340-366*, 2016.

[38] D. J. Benson, *Encyclopedia of Computational Mechanics, Part 2. Solid and Structures.* John Wiley and Sons, 2007.

[39] LS-Dyna, “What are the differences between implicit and explicit?,”

[40] Dassault Systems Simulia Corp., “Lecture: Overview of abaqus/explicit.” `http://support.xitadel.com/035727-Overview-of-ABAQUSExplicit`. Accessed on 01-03-2019.

[41] SIMULIA Abaqus/CAE User’s Guide, “Section: Explicit dynamic analysis,”

[42] O. S. Hopperstad and T. Børvik, “Modelling of plasticity and failure with explicit finite element methods,” 2016.

[43] O. S. Hopperstad and T. Børvik, “Material mechanics - part i,” 2017.

[44] T. Belytschko, W. K. Liu, B. Moran, and K. I. Elkhodary, *Nonlinear Finite Elements for Continua and Structures. Second Edition.* John Wiley and Son, 2014.

[45] K. Mathisen and V. Prot, “Lecture 10: Imposing constraints,” 2018.

[46] SIMULIA Abaqus/CAE User’s Guide, “Section: Contact,”

[47] SIMULIA Abaqus/CAE User’s Guide, “Element selection in abaqus,”

[48] Wikipedia, “First law of thermodynamics.” `https://en.wikipedia.org/wiki/First_law_of_thermodynamics`, February 2019. Accessed on 14-03-2019.

[49] B. Després, *Numerical Methods for Eulerian and Lagrangian Conservation Laws.* J Springer International Publishing AG, 2017.

[50] SAS IP, Inc., “Lagrangian and Eulerian Reference Frames.” `https://www.sharcnet.ca/Software/Ansys/16.2.3/en-us/help/wb_sim/exp_dyn_theory_lag_eul_360.html`, June 2015. Accessed on 24-05-2019.

[51] SIMULIA Abaqus/CAE User's Guide, "Section: Multiphysics analysis, co-simulation:overview,"

[52] F. G. Friedlander, "The diffraction of sound pulses: diffraction by a semi-infinite plane," *Proceedings of the Royal Society of London. Series A, Mathematical and Physical Sciences (1934-1990), Volume 186(1006): 322-344*, 1946.

[53] G. Gruben, M. Langseth, E. Fagerholt, and O. S. Hopperstad, "Low-velocity impact on high-strength steel sheets: An experimental and numerical study," *International Journal of Impact Engineering, Volume 88: 153-171*, 2016.

[54] M. F. Ashby and D. R. H. Jones, *Engineering Materials 1: An Introduction to Their Properties and Applications.* Elsevier Butterworth-Heinemann, second edition, 2002.

[55] Wikipedia, "Allotropy." `https://en.wikipedia.org/wiki/Allotropy`, March 2019. Accessed on 26-04-2019.

[56] Wikipedia, "Allotropes of iron." `https://en.wikipedia.org/wiki/Allotropes_of_iron`, May 2018. Accessed on 24-05-2019.

[57] K. Hermann, *Crystallography and surface structure : an introduction for surface scientists and nanoscientists. 2nd edition.* Wiley-VCH, 2017.

[58] S. Papavinasam, *Corrosion Control in the Oil and Gas Industry: Chapter 3 - Materials.* Elsevier, 2014.

[59] M. Shome and M. Tumuluru, *Welding and Joining of Advanced High Strength Steels.* Woodhead Publishing, 2015.

[60] Wikipedia, "Alloy." `https://en.wikipedia.org/wiki/Alloy`, May 2019. Accessed on 30-05-2019.

[61] Diehl Steel, "Effects of common alloying elements in steel." `http://www.diehlsteel.com/technical-information/effects-of-common-alloying-elements-in-steel`, 2018. Accessed on 20-03-2019.

[62] N. Baddoo and P. Morado, "Niobium microalloyed structural steels." `http://www.oakleysteel.co.uk/niobium-microalloyed-structural-steels`, December 2014. Accessed on 20-03-2019.

[63] Metal Supermarkets, "5 common alloying elements." `https://www.metalsupermarkets.com/5-common-alloying-elements/`, August 2017. Accessed on 20-03-2019.

[64] WebCite, "HSLA Steel." `https://www.webcitation.org/5mVi3a0kt?url=http://machinedesign.com/article/hsla-steel-1115`, November 2002. Accessed on 23-04-2019.

[65] World Auto Steel, "Steel Definitions: Today's AHSS for Automotive." `https://www.worldautosteel.org/steel-basics/automotive-steel-definitions/`, 2018. Accessed on 23-04-2019.

[66] D. Mayer, "Cubic body centered lattice structure." `https://commons.wikimedia.org/wiki/User:Rocha#/media/File:Cubic-body-centered.png`, May 2004. Accessed on 22-04-2019.

[67] D. Mayer, "Cubic, face-centered." `https://commons.wikimedia.org/wiki/User:Rocha#/media/File:Cubic,_face-centered.png`, May 2004. Accessed on 22-04-2019.

[68] D. Mayer, "Tetragonal-body-centered." `https://commons.wikimedia.org/wiki/File:Tetragonal-body-centered.svg`, March 2007. Accessed on 22-04-2019.

[69] Metal Supermarkets, "What is annealing?." `https://www.metalsupermarkets.com/what-is-annealing/`, August 2018. Accessed on 21-04-2019.

[70] World Auto Steel, "Dual Phase (DP) Steels." `https://www.worldautosteel.org/steel-basics/steel-types/dual-phase-dp-steels/`, 2018. Accessed on 23-04-2019.

[71] SSAB, "DATASHEET: 13-02-14 GB8201 DOCOL." `http://www.meracing.com/UserFiles/Products/Sheetmetal/201_Docol_DP_DL.pdf`. Accessed on 05-02-2019.

[72] SSAB, "DATASHEET: 09-03-18 GB8207 DOCOL." `https://www.yumpu.com/en/document/read/11500088/docol-m-ssab`. Accessed on 05-02-2019.

[73] W. F. Hosford, "A generalized isotropic yield criterion," *Journal of Applied Mechanics, Volume 39(2): 607-609*, 1972.

[74] O. Björklund, "Modelling of failure in high strength steel sheets," *Linköping Studies in Science and Technology: Thesis No. 1529*, 2012.

[75] J. K. Holmen, O. S. Hopperstad, and T. Børvik, "Low-velocity impact on multi-layered dual-phase steel plates," *International Journal of Impact Engineering, Volume 78: 161-177*, 2014.

[76] G. Gruben, D. Morin, M. Langseth, and O. S. Hopperstad, “Ductile fracture of steel sheets under dynamic membrane loading,” *Procedia Engineering, Volume 197: 185-195*, 2017.

[77] SIMULIA Abaqus/CAE User’s Guide, “Section: The mesh module,”

[78] G. Sigstad and H. H. Kristiansen, “Master thesis (unpublished): Experimental and numerical study on perforated steel plates subjected to blast loading,” 2019.

[79] C. Baglo and T. M. Dybvik, “Master thesis: Experimental and numerical study on plated structures subjected to blast loading - numerical simulations and experimental validation,” 2015.

[80] J. K. Holmen and J. Johnsen, “Master thesis: Effects of heat treatment on the ballistic properties of aa6070 aluminium plates,” 2012.

[81] E. Fagerholt, “eCorr v4.0 Documentation.” `http://folk.ntnu.no/egilf/ecorr/doc/`, 2019. Accessed on 22-03-2019.

[82] Hexagon Manufacturing Intelligence, “ROMER Absolute Arm.” `https://www.hexagonmi.com/en-GB/products/portable-measuring-arms/romer-absolute-arm`, 2019. Accessed on 23-03-2019.

[83] MathWorks, “movmean.” `https://se.mathworks.com/help/matlab/ref/movmean.html`, 2019. Accessed on 29-02-2019.

[84] Structural Impact Laboratory, “SIMLab Metal Model (SMM): Theory-, User’s- and Example Manual: SMM v3.2,” September 2015.

[85] SIMULIA Abaqus/CAE User’s Guide, “Section: Adaptive meshing and distortion control,”

[86] SIMULIA Abaqus/CAE User’s Guide, “Section: The part module,”

[87] J. K. Holmen, O. S. Hopperstad, and T. Børvik, “Influence of yield-surface shape in simulation of ballistic impact,” *International Journal of Impact Engineering 108 (2017) 136-146*, 2009.

[88] M. Ravid and R. Bodner, “Dynamic perforation of viscoplastic plates by rigid projectiles,” *International Journal of Engineering Science, Volume 21(6): 577-591*, 1983.

[89] J. A. Zukas, *High velocity impact dynamics*. Wiley, New York, 1990.

[90] SIMULIA Abaqus/CAE User’s Guide, “Section: Prescribed conditions, loads,”

[91] G. Gruben, O. S. Hopperstad, and T. Børvik, “Evaluation of uncoupled ductile fracture criteria for the dual-phase steel docol 600dl,” *International Journal of Mechanical Sciences, Volume 62: 133-146*, 2012.

Appendices

Appendix A

Numerical Results

A.1 Energy Plots from Chapter 4

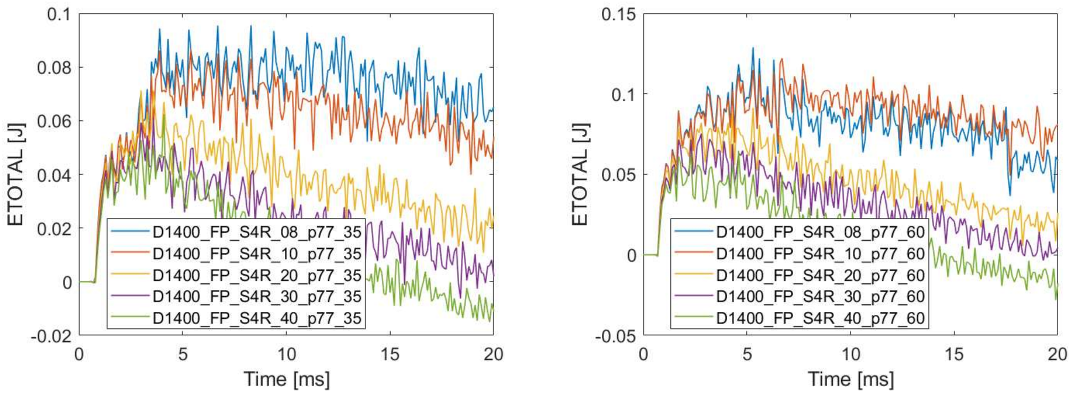

(a) Conservation of energy.

(b) Conservation of energy.

Figure A.1: Conservation of energy plots from the preliminary study in Chapter 4.

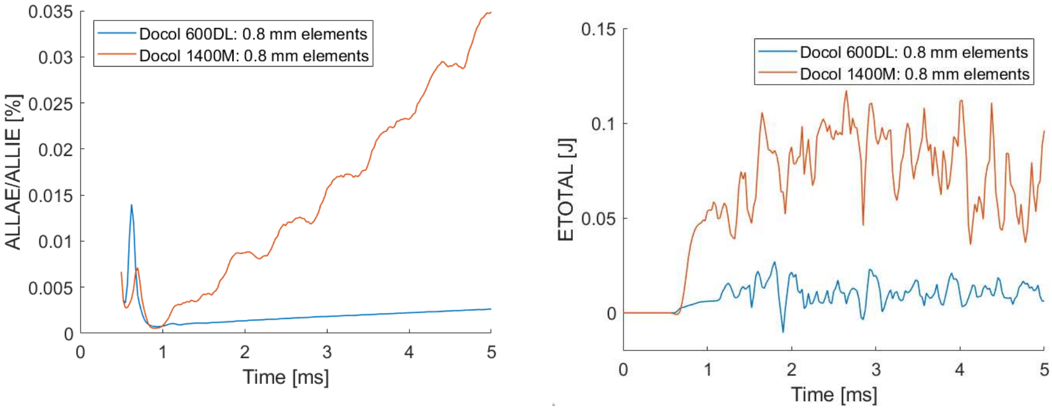

(a) Docol 600DL and 1400M FP 75 bar
Artificial energy.

(b) Docol 600DL and 1400M FP
Conservation of energy.

Figure A.2: Artificial energy ratio and conservation of total energy plots from preliminary study in Chapter 4.

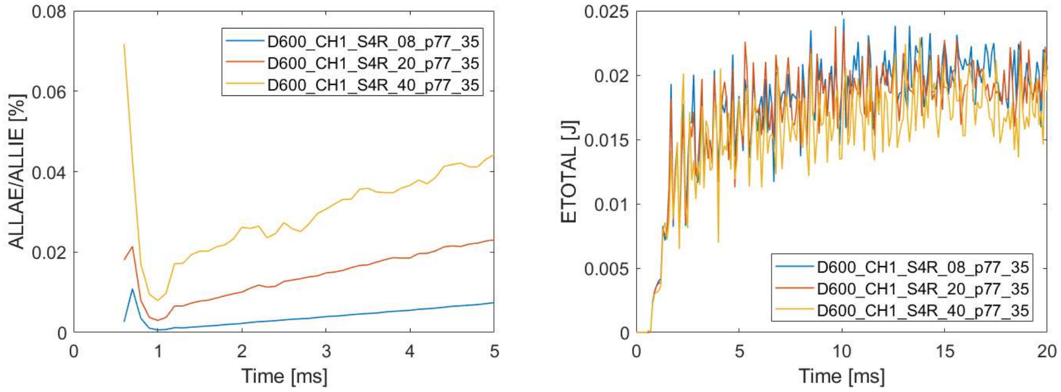

(a) Docol 600DL CH1 35 bar
Artificial energy.

(b) Docol 600DL CH1 35 bar
Conservation of energy.

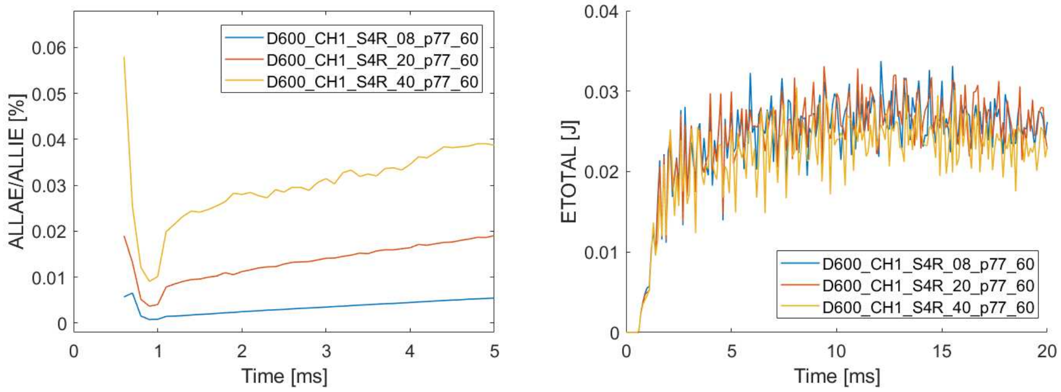

(c) Docol 600DL CH1 60 bar
Artificial energy.

(d) Docol 600DL CH1 60 bar
Conservation of energy.

Figure A.3: Artificial energy ratio and conservation of total energy plots from preliminary study in Chapter 4.

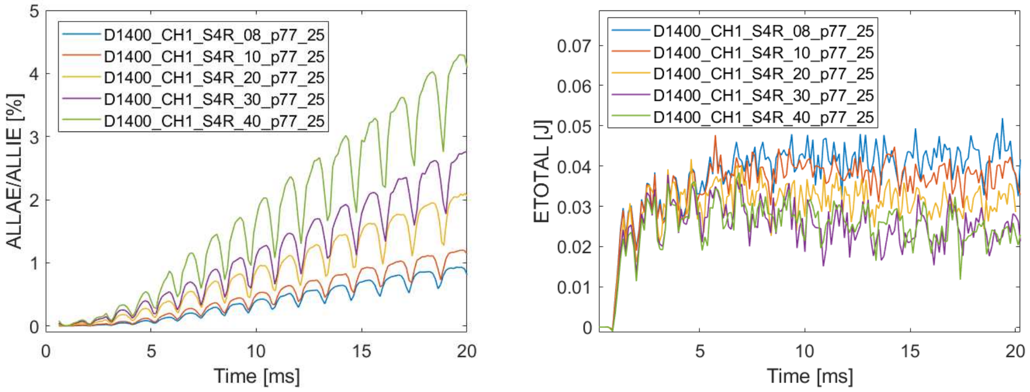

(a) Docol 1400M CH1 25 bar
Artificial energy.

(b) Docol 1400M CH1 25 bar
Conservation of energy.

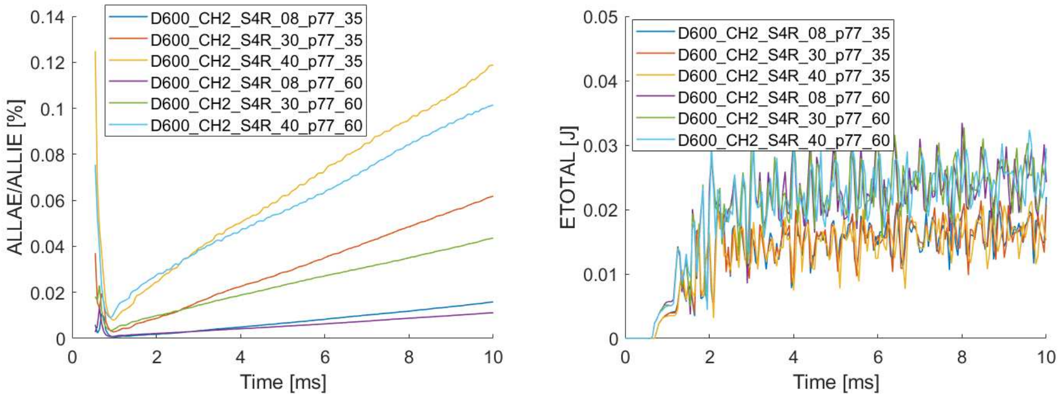

(c) Docol 600DL CH2 35 and 60 bar
Artificial energy.

(d) Docol 600DL CH2 35 and 60 bar
Conservation of energy.

Figure A.4: Artificial energy ratio and conservation of total energy plots from preliminary study in Chapter 4.

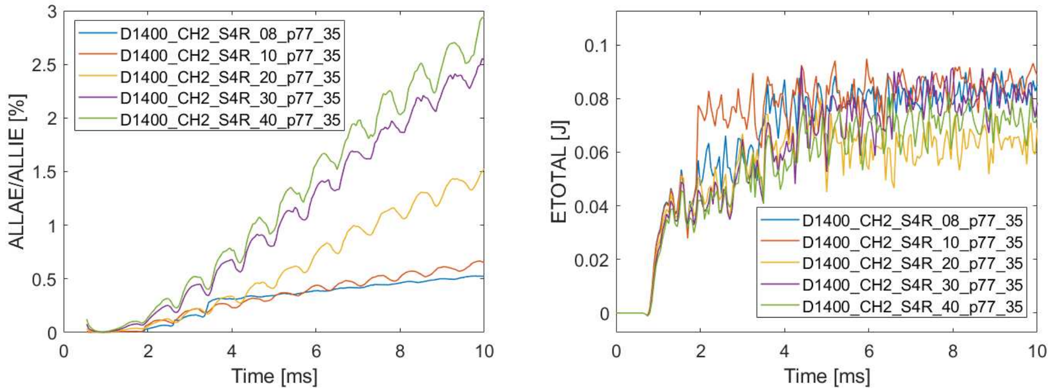

(a) Docol 1400M CH2 35 bar
Artificial energy.

(b) Docol 1400M CH1 35 bar
Conservation of energy.

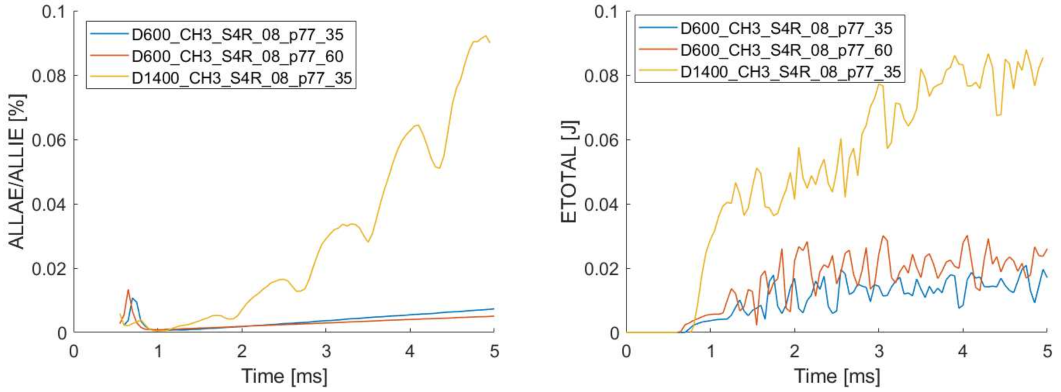

(c) Docol 600DL and 1400M CH3
Artificial energy.

(d) Docol 600DL and 1400M
Conservation of energy.

Figure A.5: Artificial energy ratio and conservation of total energy plots from preliminary study in Chapter 4.

A.2 Energy Plots from Chapter 6

Mesh Study

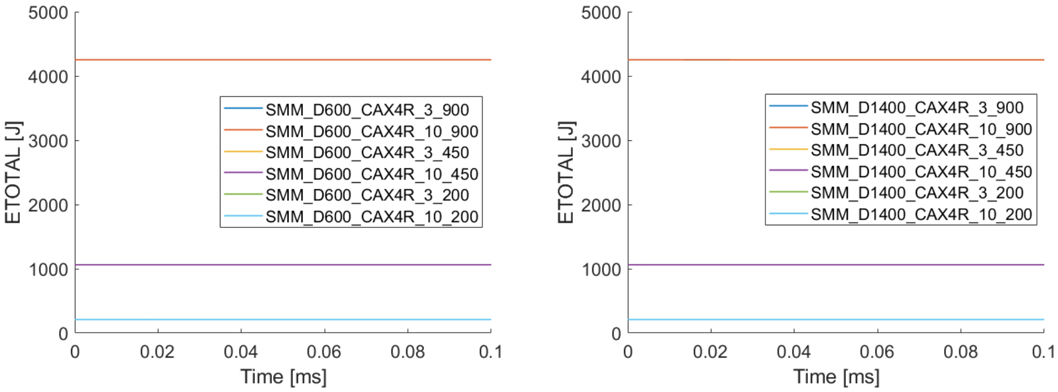

(a) Docol 600DL: conservation of energy. **(b)** Docol 1400M: conservation of energy.

Figure A.6: Conservation of energy plots from the mesh study in Chapter 6.

Projectile Study

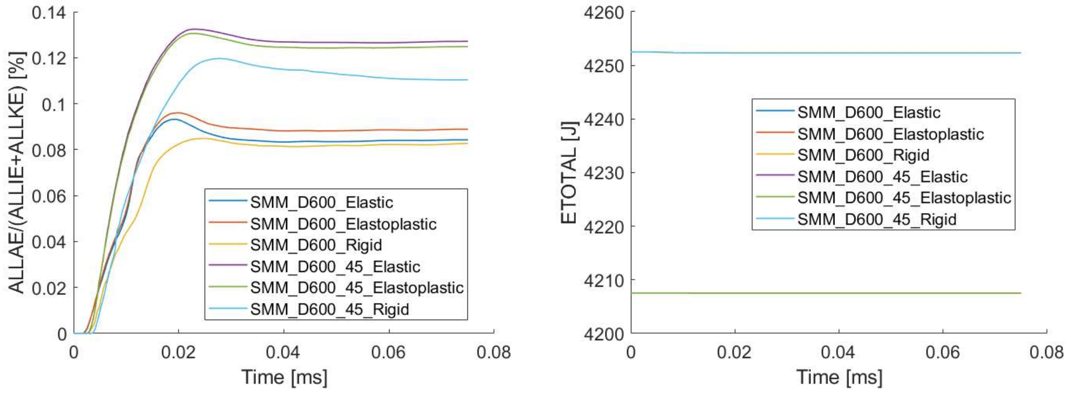

(a) Docol 600DL: artificial strain energy. **(b)** Docol 600DL: conservation of energy.

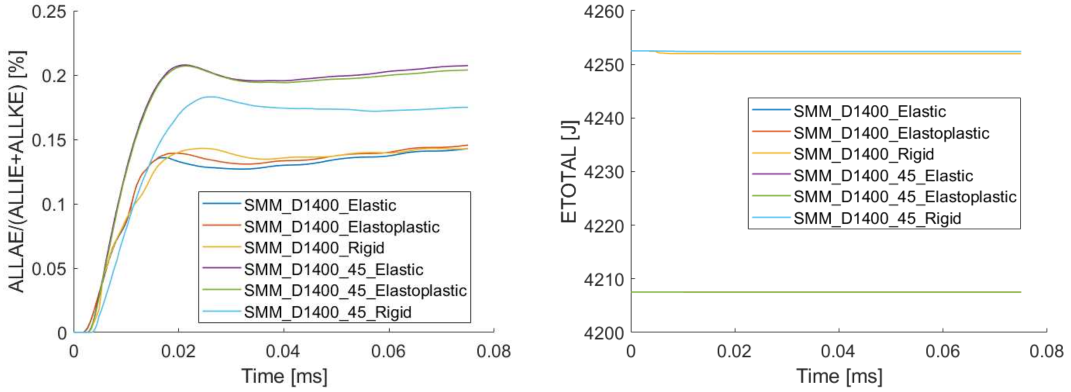

(c) Docol 600DL: artificial strain energy. **(d)** Docol 600DL: conservation of energy.

Figure A.7: Artificial strain energy plots and conservation of energy plots from the projectile study in Chapter 6.

A.3 Energy Plots from Chapter 7

A.3.1 Section 7.3.1.

Ballistics Simulations

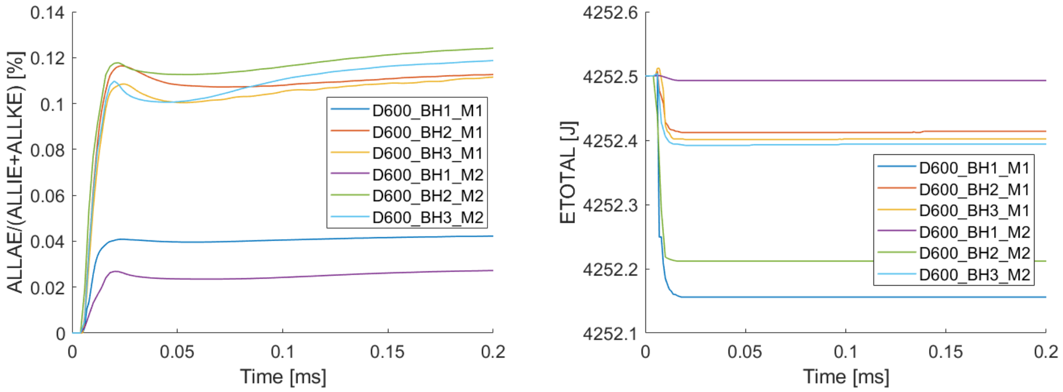

(a) D600: ALLAE/(ALLIE+ALLKE) **(b)** D600: ETOTAL

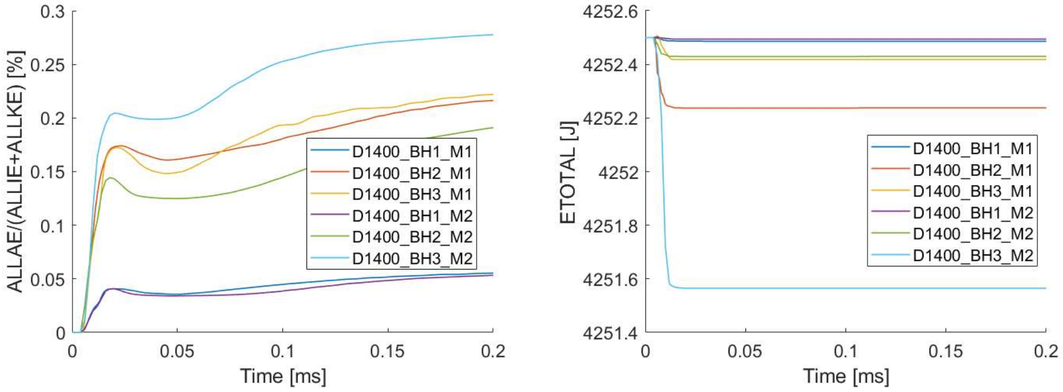

(c) D1400: ALLAE/(ALLIE+ALLKE) **(d)** D1400: ETOTAL

Figure A.8: Energy plots for the ballistics simulations at normal impact from Section 7.3.1.

Blast Loading Simulations

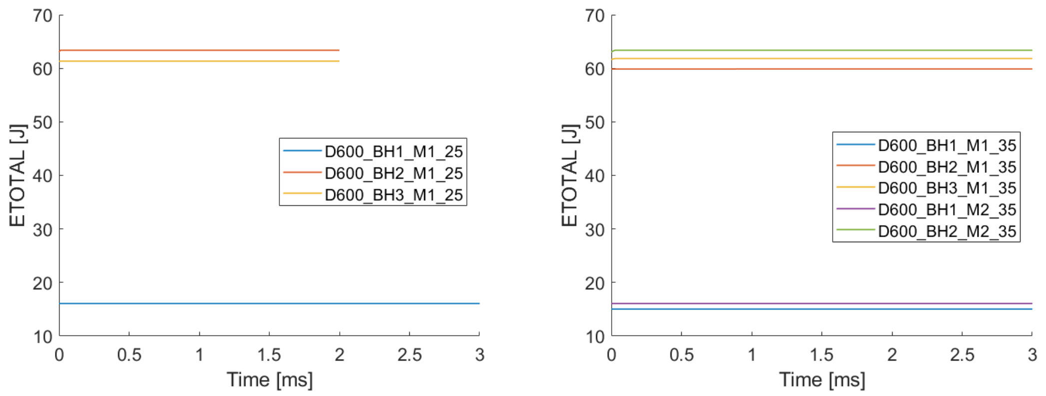

(a) Conservation of energy. **(b)** Conservation of energy.

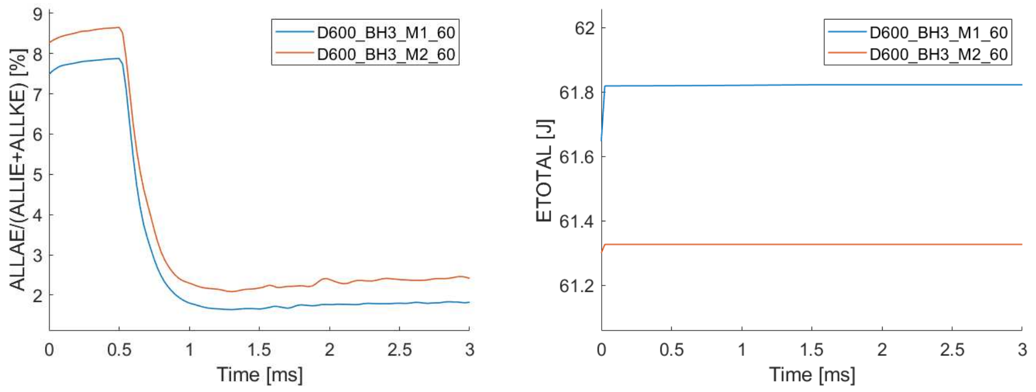

(c) Artificial strain energy. **(d)** Conservation of energy.

Figure A.9: Energy plots for Docol 600DL blast loading simulations from Section 7.3.1..

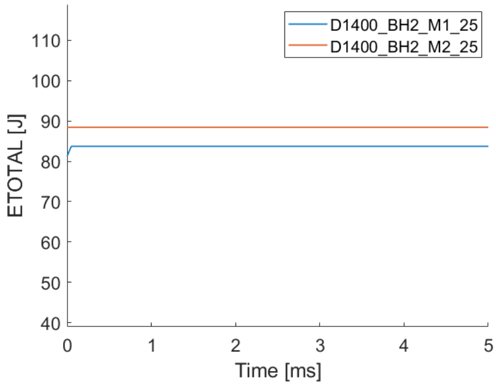

(a) Conservation of energy.

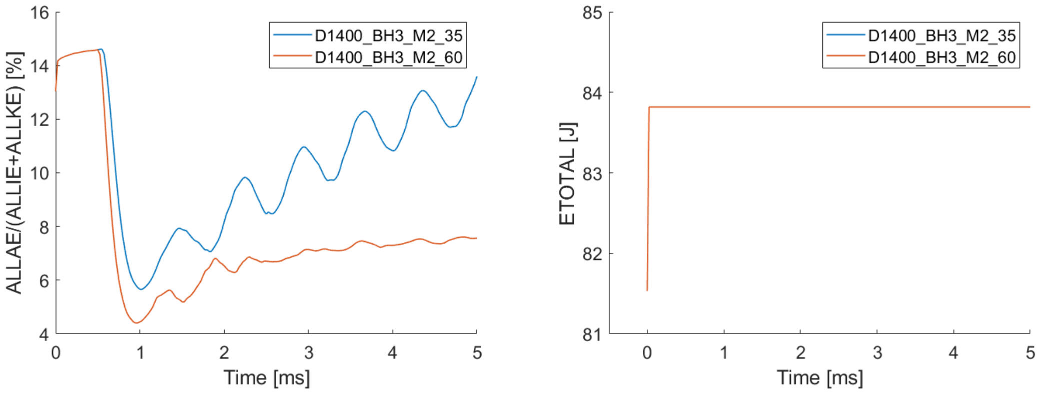

(b) Artificial strain energy energy.

(c) Conservation of energy.

Figure A.10: Energy plots for Docol 1400M blast loading simulations from Section 7.3.1..

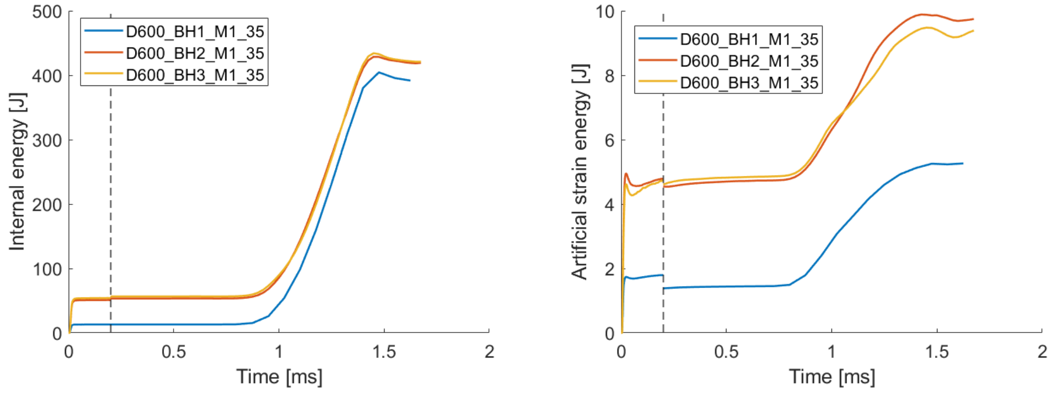

(a) Internal energy. **(b)** Artificial strain energy.

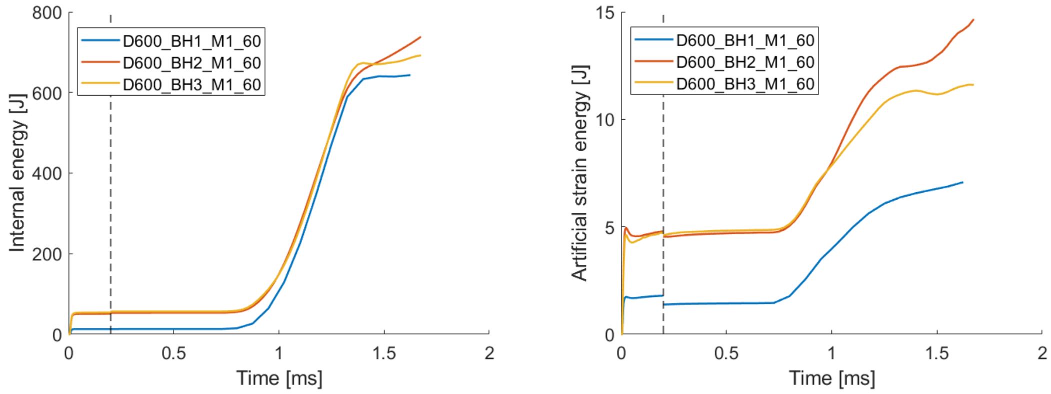

(c) Internal energy. **(d)** Artificial strain energy.

Figure A.11: Energy plots from the transition between steps in restart analysis from Section 7.3.1., for Docol 600DL with mesh configuration M1.

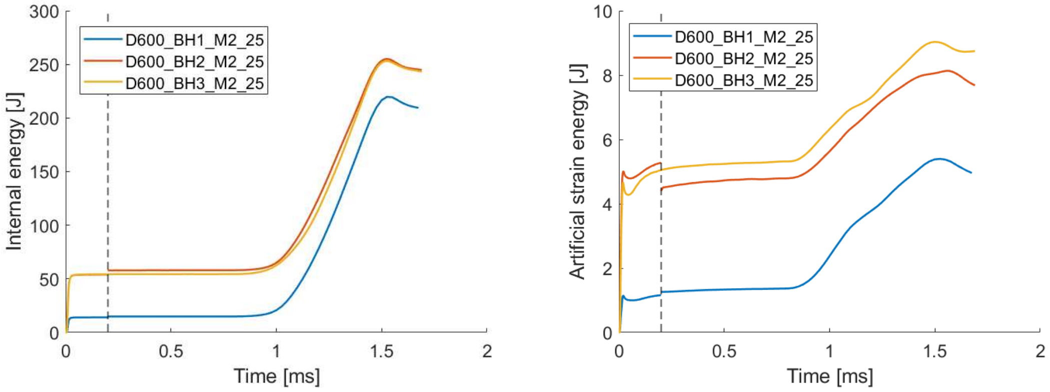

(a) Internal energy. **(b)** Artificial strain energy.

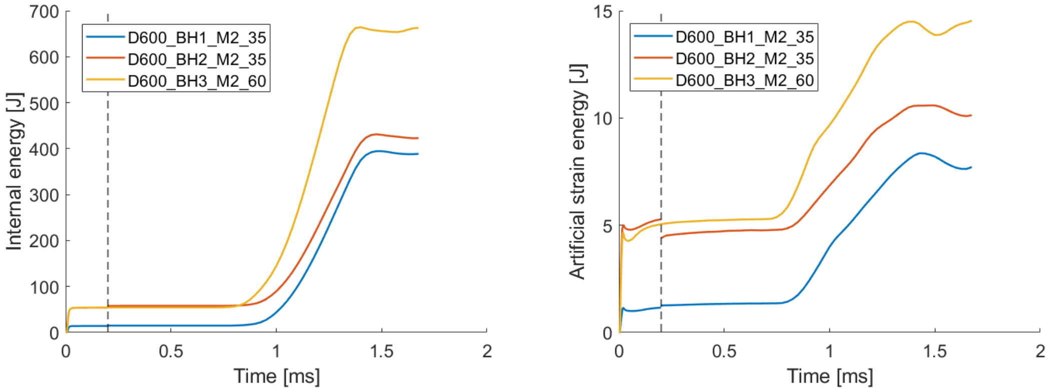

(c) Internal energy. **(d)** Artificial strain energy.

Figure A.12: Energy plots from the transition between steps in restart analysis from Section 7.3.1., for Docol 600DL with mesh configuration M2.

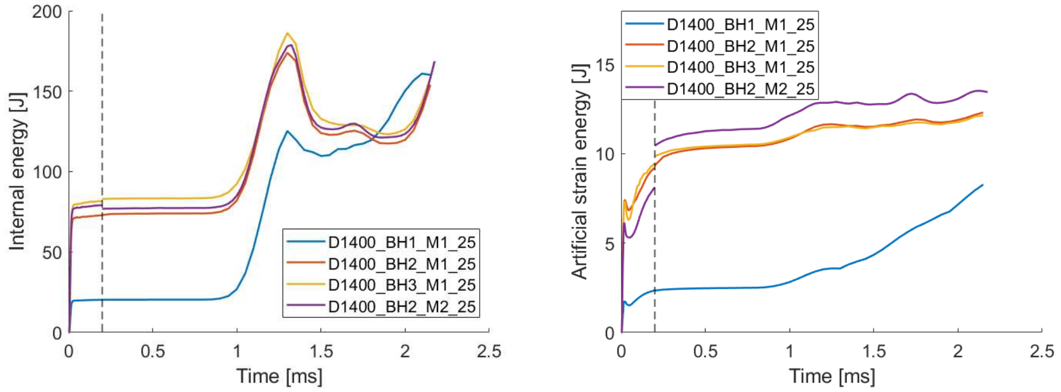

(a) Internal energy. **(b)** Artificial strain energy.

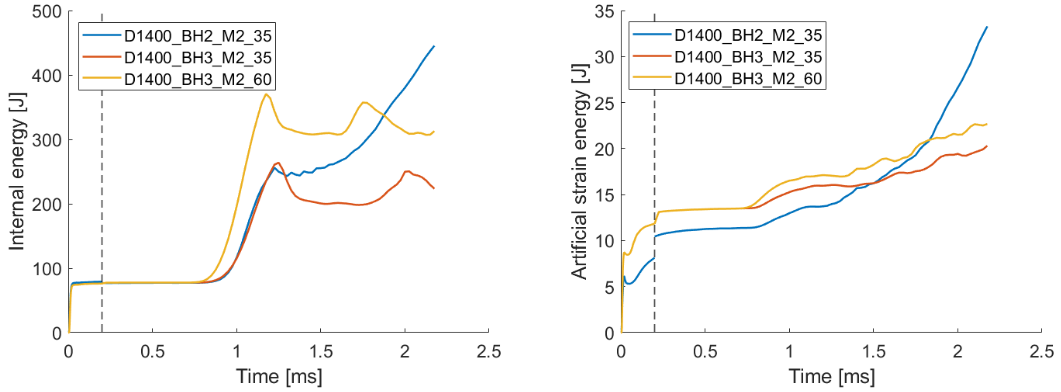

(c) Internal energy. **(d)** Artificial strain energy.

Figure A.13: Energy plots from the transition between steps in restart analysis from Section 7.3.1., for Docol 1400M with mesh configuration M1 and M2.

A.3.2 Section 7.3.2.

Ballistics Simulations

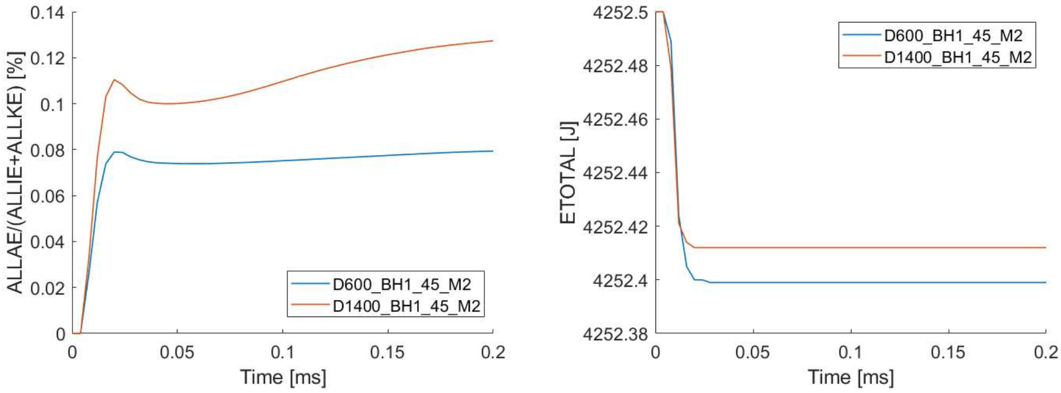

(a) Artificial strain energy. **(b)** Conservation of energy.

Figure A.14: Artificial strain energy and conservation of energy plots from Section 7.3.2.

Blast Loading Simulations

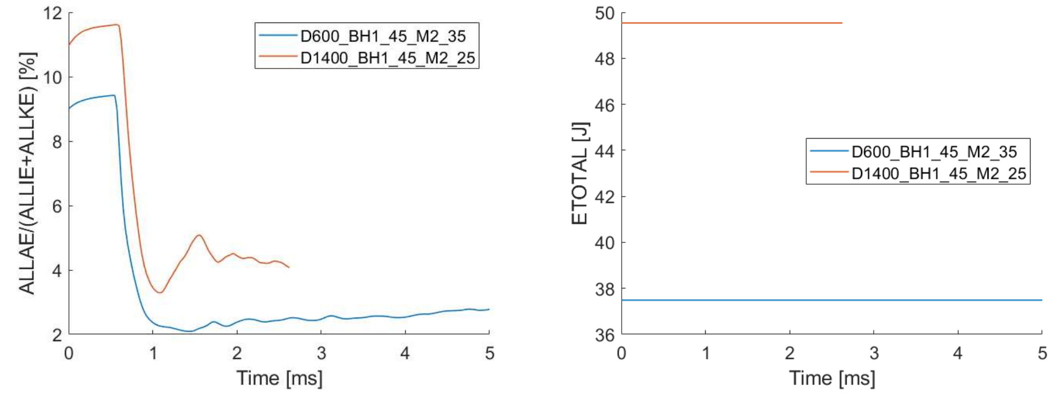

(a) Artificial strain energy. **(b)** Conservation of energy.

Figure A.15: Artificial strain energy and conservation of energy plots from Section 7.3.2.

A.3.3 Section 7.3.3.

CL Fracture Parameter Study

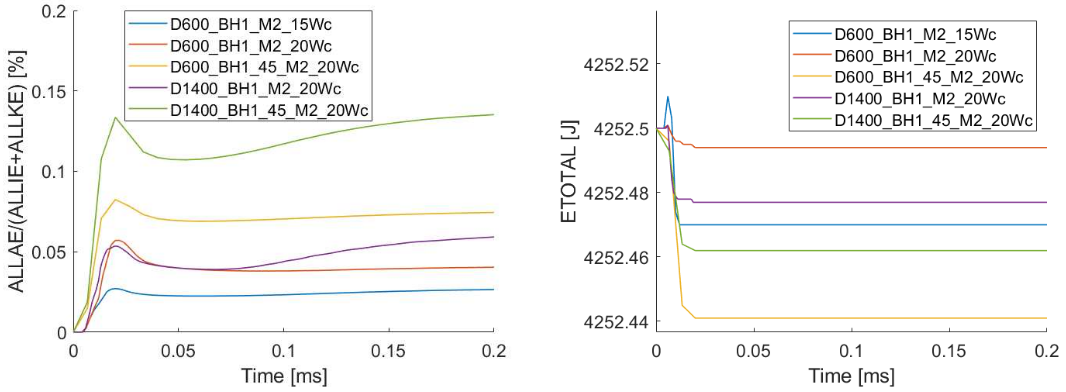

(a) Artificial strain energy. **(b)** Conservation of energy.

Figure A.16: Energy plots from the CL fracture parameter study. (A.16a) and (A.16b) shows energy plots from the ballistics simulations.

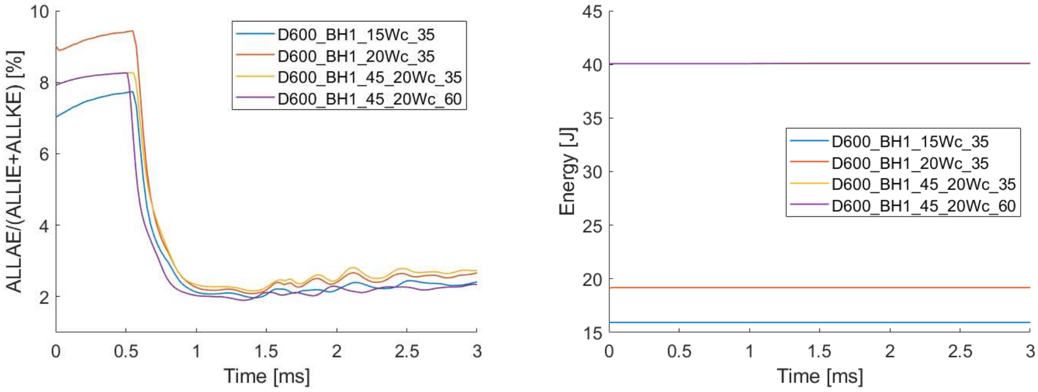

(a) Artificial strain energy.

(b) Conservation of energy.

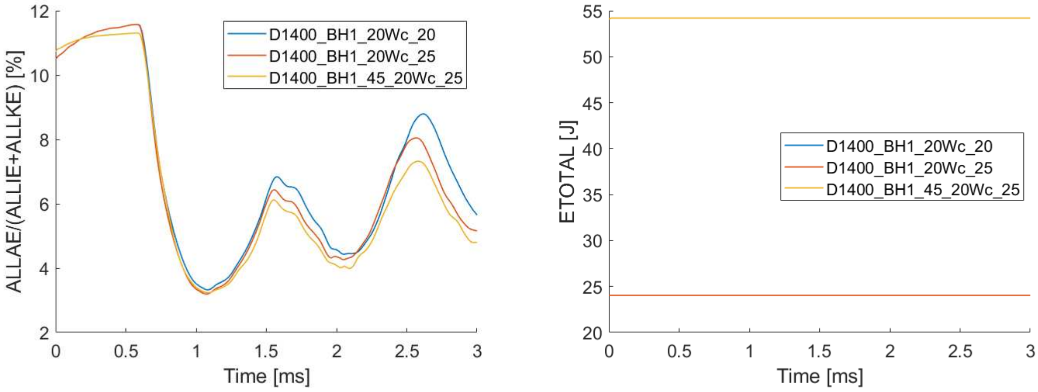

(c) Artificial strain energy.

(d) Conservation of energy.

Figure A.17: Energy plots from the CL fracture parameter study. (A.17a) and (A.17b) shows energy plots from the blast loading simulations for Docol 600DL, and (A.17c) and (A.17d) shows the energy plots from the blast loading simulations for Docol1400M.

Strain Rate Sensitivity Parameter Study

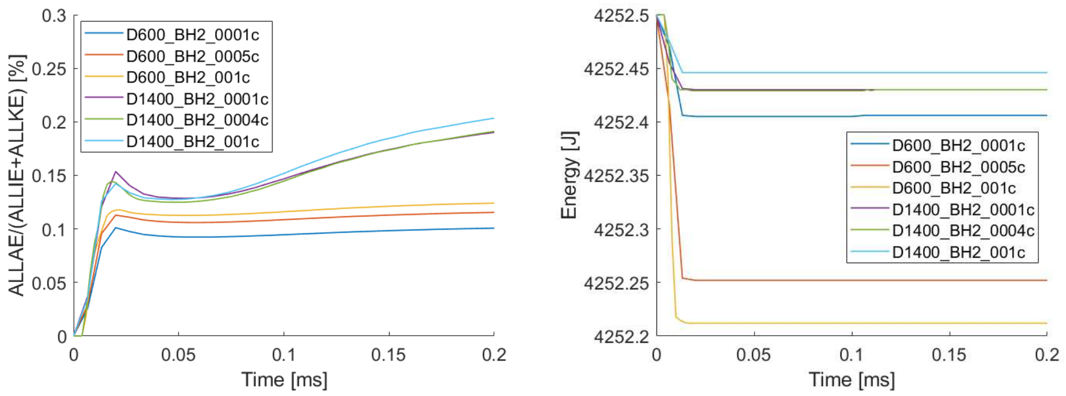

(a) Artificial strain energy.

(b) Conservation of energy.

Figure A.18: Energy plots from the strain rate sensitivity parameter study. (A.18a) and (A.18b) shows energy plots from the ballistics simulations.

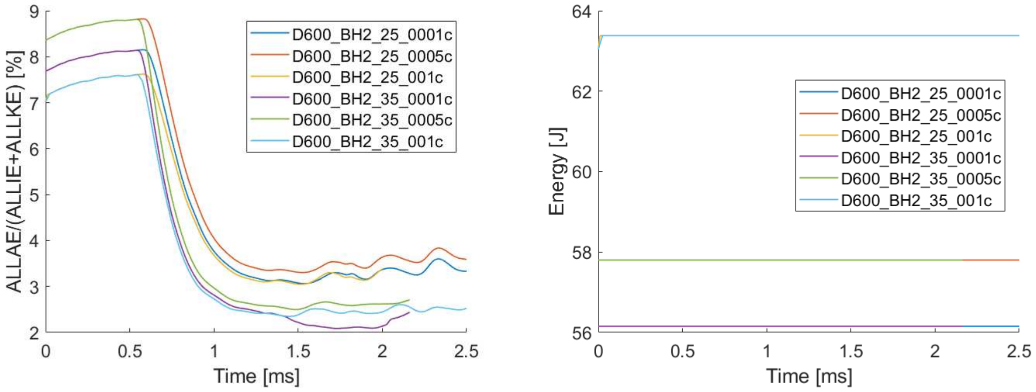

(a) Artificial strain energy. **(b)** Conservation of energy.

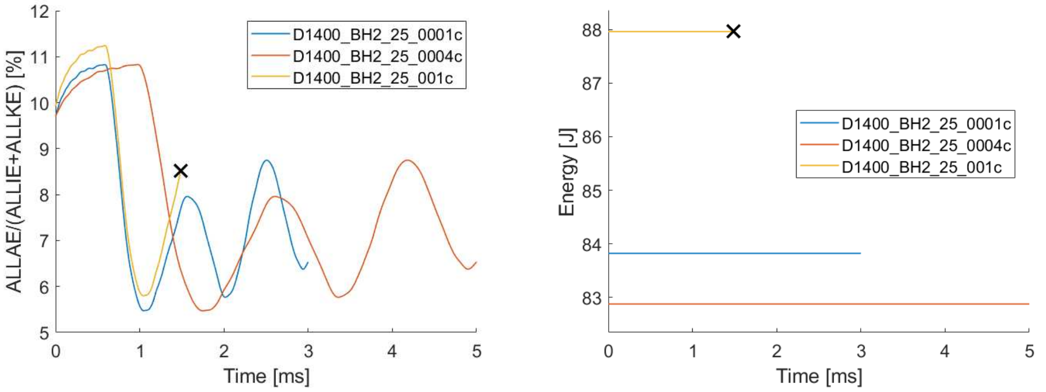

(c) Artificial strain energy. **(d)** Conservation of energy.

Figure A.19: Energy plots from the strain rate sensitivity parameter study. (A.19a) and (A.19b) shows energy plots from the blast loading simulations for Docol 600DL, and (A.19c) and (A.19d) shows the energy plots from the blast loading simulations for Docol 1400M. The "X" indicates abortion of the simulation due to a power outage.

A.4 Contour Plots from Chapter 7

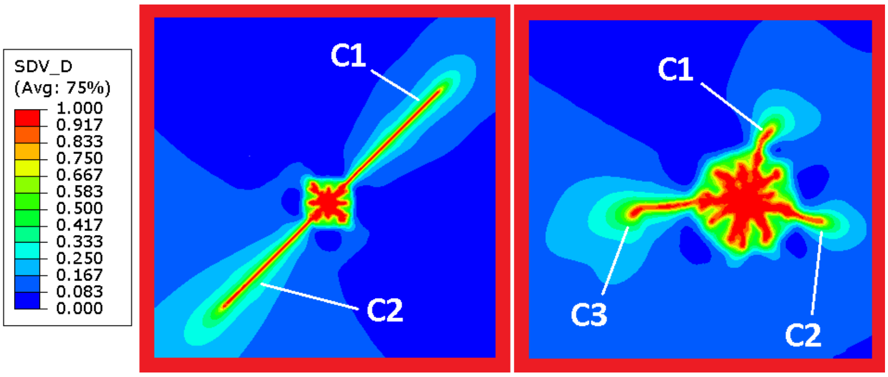

Figure A.20: Damage accumulation plot on undeformed configuration for Docol 600DL using the BH3 configuration at 60 bar. Using the M1 mesh configuration (left) and the M2 configuration (right).

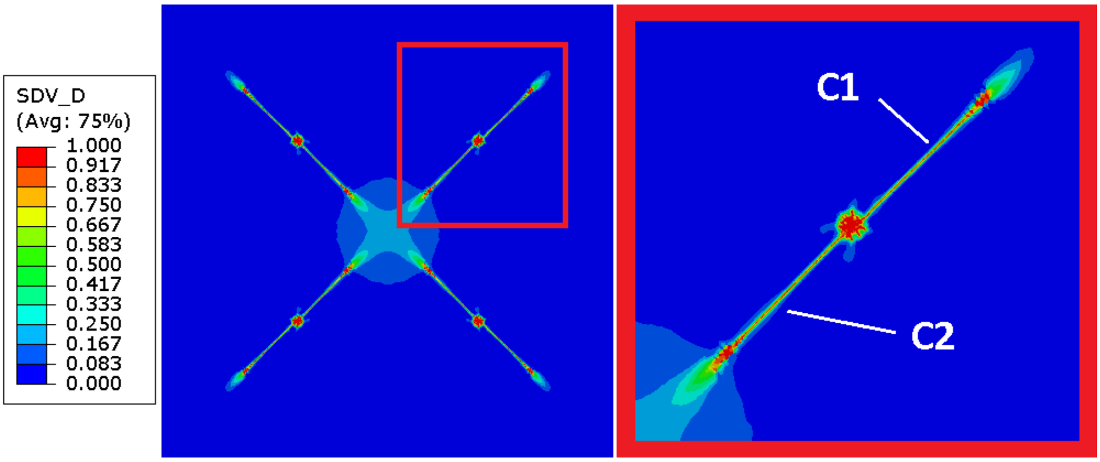

Figure A.21: Damage accumulation plot on undeformed configuration for Docol 1400M using the BH3 configuration at 60 bar.

Table A.1: Measured crack lengths. The naming of the cracks follow from Figure A.20 and A.21.

Simulation	**C1** [mm]	**C2** [mm]	**C3** [mm]
D600_BH3_M1_60	20.56	19.24	-
D600_BH3_M2_60	2.16	2.10	5.02
D1400_BH3_M2_60	45.26	48.98	-

A.5 Displacement Histories from Chapter 7

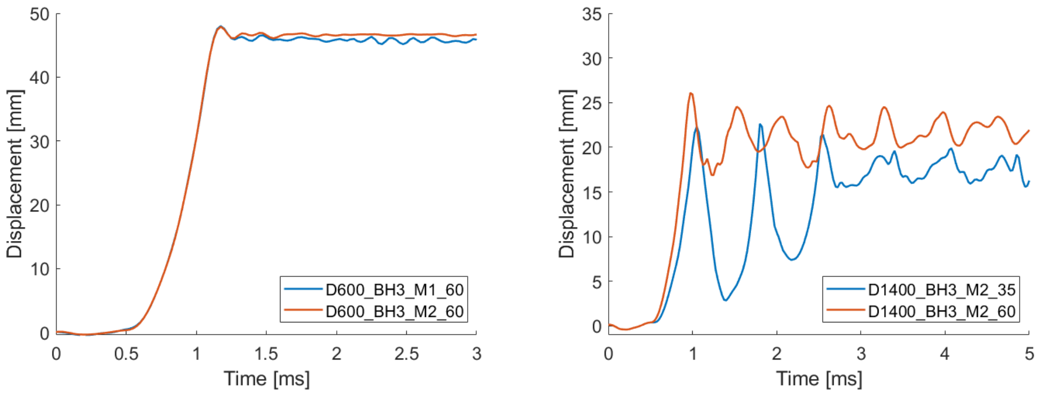

(a) Displacement histories for Docol 600DL.

(b) Displacement histories for Docol 1400M.

Figure A.22: Displacement histories for blast loading simulations outside of the experimental program from Section 7.3.1.

Table A.2: Maximum deflection for the simulations outside of the experimental program.

Simulation	**Maximum Deflection** [mm]
D600_BH3_M1_60	47.99
D600_BH3_M2_60	47.88
D1400_BH3_M2_35	22.63
D1400_BH3_M2_60	26.09

NTNU
Kunnskap for en bedre verden